Growth and multi-scale properties of hybrid magnetic tunnel junctions : towards the control of Spinterfaces

Maryam Sadeghiyan Dehaghani

COLLEGE SCIENCES DE LA MATIERE
DOCTORAL DES MOLECULES
BRETAGNE ET MATERIAUX

Université de Rennes

THÈSE DE DOCTORAT DE

L'UNIVERSITÉ DE RENNES

ÉCOLE DOCTORALE N° 638
Sciences de la Matière, des Molécules et Matériaux
Spécialité : *Materials and Nanoscience*

Par

Maryam SADEGHIYAN DEHAGHANI

Growth and multi-scale properties of hybrid magnetic tunnel junctions : towards the control of Spinterfaces

Thèse présentée et soutenue à Rennes, le 31-08-2023
Unité de recherche : Institut de Physique de Rennes (IPR) - UMR 6251

Rapporteurs avant soutenance :

Richard MATTANA — Chargé de recherche CNRS, Unité Mixte de Physique Thalès-CNRS
Amandine BELLEC — Chargée de recherche, Laboratoire Matériaux et Phénomènes Quantiques

Composition du Jury :

President :	Corinne LAGROST	Directrice de recherche CNRS, Institut des sciences chimiques de Rennes
Examinateurs :	Richard MATTANA	Chargé de recherche CNRS, Unité Mixte de Physique Thalès-CNRS
	Amandine BELLEC	Chargée de recherche, Laboratoire Matériaux et Phénomènes Quantiques
Dir. de thèse :	Pascal TURBAN	Professeur des Universités, Institut de Physique de Rennes

Invité(s) :

Sophie GUEZO — Maitre de Conférences, Institut de Physique de Rennes
Samy BOUKARI — Maitre de Conférences, Institut de Physique et Chimie des Matériaux de Strasbourg

Acknowledgement

I would like to express my heartfelt gratitude to all the individuals who have contributed to the completion of this thesis. First and foremost, I would like to express my deepest appreciation to my supervisors Prof. Pascal Turban, Prof. Francine Solal, and Dr. Sophie Guezo for their unwavering guidance, encouragement, and support throughout this research. Their deep knowledge, expertise, and enthusiasm for science have been an immense source of inspiration to me. Their mentorship and encouragement have helped me to push the boundaries of my research, and I am extremely grateful for the opportunity to have worked with them. I would like to extend my deepest gratitude to Francine who has been an incredible mentor, friend and family all at once. It was an astonishing pleasure and opportunity to be her last student before retirement.

I would also like to acknowledge the invaluable contribution of my colleagues in my team. In particular, I would like to acknowledge Dr. Soraya Ababou-Girard for her invaluable contributions to my research and for being an amazing colleague and friend. I am also indebted to Dr. Sylvain Tricot, Dr. Bruno Lépine, and Mr. Arnaud Le Pottier for their collaborative spirit, exceptional work ethics, and their invaluable contributions to my experiments and thesis. They have provided a supportive and collaborative environment for me to conduct my research and have helped me to develop both personally and professionally. Their contributions, ideas, and feedback have been invaluable, and I am deeply grateful.

Furthermore, I would like to extend my gratitude to my family for their

unconditional love, support and encouragement throughout my journey. I am particularly grateful to my parents Tayebeh and Hamid for their sacrifices, and for supporting me both emotionally and financially.

بالاترین تشکر را از پدر و مادر عزیزم دارم که بزرگترین فداکاری ها را بدون چشم داشت و سرشار از محبت انجام میدهند، برای تمام خوشحالی هایی که بخاطرشان تجربه کردم و برای باوری که در من داشتند. پدر و مادری که نه تنها تجربه منحصر به فرد آرامش را برایم فراهم کردند، بلکه از تمام تصمیماتم پشتیبانی کردند. ممنونم!

My little brother, Majid, has been a constant source of support, encouragement and humor, and I am deeply grateful for his unwavering presence in my life.

I am also indebted to my close friends, who have been a great source of emotional and intellectual support throughout this journey. In particular, I would like to thank Azadeh Yazdani, who has been my sister and my safe place with unconditional support. I am also grateful to Mahsa Nazemi Ashani, Pardis Mortezaei and Saba Moradi, who have become a part of my second family, for having always believed in me. Additionally, I would like to thank Dr. Ellie Alipour, Mitra Vafaie, Dr, Shiva Moradmand, Dr. Alireza Mottaghizadeh , Dr. Philipp del Hougne and Lyle De La Cloche, who have been very close friends to me throughout my life, for their support and encouragement.

I would like to also express my appreciation and acknowledgment to the invaluable individuals who have undoubtedly enriched my life, and made me feel at home in France, Prof. Massimilano Marangolo, Prof. Didier Sebilleau, Dr. Corentin Tregouet, Olivier Girard, Theo Lenavetier, Ambroise Mathey and Lucas Jannin.

Finally, I would like to thank all of my colleagues at IPR including all the PhDs, post-docs, and permanents who have provided critical support and for the great time passed at IPR during these years!

I recognize that my success would not have been possible without the support and encouragement of each and every individual mentioned above. I am grateful to have had such a supportive network of people in my life, and I will be forever grateful for their contributions to my academic and personal growth.

Contents

1 Introduction

General overview

Spintronics is an emerging field of fundamental research and technology proposed as a promising alternative to classical electronics. In field of electronics, scientists and engineers have worked continuously to make silicon chips smaller and smaller to the extent of tens of millimeter, containing billions of silicon transistors. The transistor size is reducing to an extent of 3 to 7 nanometers technology. At these ultimate scales, technological limitations are arising such as overheating, data rot (due to leakage current), slower speed, etc. These limitations are mostly related to the fact that classical electronics is based on charge transport. To overcome this challenge, rather than using the charge of an electron as our binary state, spin of an electron can be used for the same purpose. As every electron either possesses spin up or spin down, these can be assigned as a binary logic 1/0. The information now in encoded on a magnetic moment resulting in a non-volatile character, thus leading to reduced energy consumption in devices. The branch which especially works/studies on this intrinsic property of electron on electronics is known as spin electronics or commonly called as spintronics. Spin-electronics is now considered as a credible technology for the future development of green electronics. Even though spintronics is a relatively recent domain, this field has already been largely exploited on the market. For instance, the hard disk read heads, the non-volatile magnetic random access memories (MRAMs), Racetrack memories, magnetic-field sensors, or even applications in quantum-computing [1, 2, 3] have been developed, based on spin transport in magnetic

heterojunctions. This first generation of devices was recently extended to hybrid organic/inorganic heterojunctions, giving birth to a new research field called molecular spintronics[4]. This discovery quickly boosted the interest of this field. In the following, I will review spintronics, focusing on the tunnel magnetoresistace effect, to have a better understanding of the basics of this study. I will further continue with molecular spintronics and show the importance of ferromagnet/molecule interface. This chapter later will be carry on by the challenges in this field, concerning both the physics behind molecular spintronics devices and the demanded fabrication technology. Finally, I will discuss the objectives of my Ph.D. work to overcome the named challenges.

1.1 Spintronics

Spintronics was born in 1988 with the discovery of Giant Magneto-Resistance (GMR) by A. Fert [5] and P. Grünberg [6], and rewarded in 2007 with the Nobel Prize in Physics. This GMR effect consists of a different measured resistance through a stack of two magnetic layers separated by a non-magnetic metal layer (spin-valve), depending on the orientation of the magnetization in the ferromagnetic layers. By replacing the separator by a very thin ($\approx$ nm) insulator layer, the GMR effect turns into Tunnel Magneto-Resistance (TMR). TMR phenomenon was discovered by Jullière (1975) at low temperature [7], and the realization of appreciable TMR in $Fe/Al_2O_3/Fe$ and $CoFe/Al_2O_3/Co$ magnetic tunnel junctions (MTJs) at RT by Miyazaki et al. [8] and Moodera et al.[9], respectively.

1.1.1 Tunnel Magneto-Resistance

1.1.1.1 Jullière's model

Jullière provided the first measurements on TMR in 1975 on a $Fe/Ge(10-15nm)/Co$ device [7]. With two FM electrodes he could exploit into a device the physical concept of spin polarized tunnel effect and he developed a model that is now widely known as Jullière's model. A schematic example to understand TMR phenomenon is shown in Figure 1.1, for a $Co/Insulator/Fe$ tunnel junction. The principle behind TMR phenomenon is spin-dependent tunneling, i.e., up-spin electrons can only tunnel into up-spin states, and down-spin electrons can tunnel to down-spin states alone.

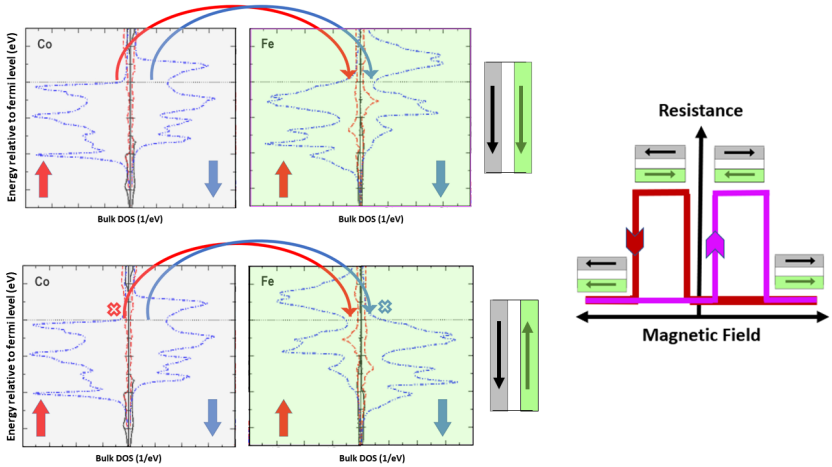

Figure 1.1: Principle of operation of a magnetic tunnel junction. The density of states for bulk Co and Fe is presented Vs the energy relative to the Fermi level [10], parallel magnetization configuration is observed in absence of magnetic field. The applied magnetic filed changes the magnetic direction of the free layer, leading to an anti-parallel magnetization configuration. A low(high) resistance is measured for parallel (anti-parallel) state.

The asymmetry of density of states (DOS) for the up and down spin electron around Fermi level leads as a consequence to different resistance states associated to the parallel or anti-parallel magnetic configuration of the MTJ. Jullière developed a simple analytical model to quantify the TMR amplitude [7] as follow:

$$TMR = \frac{R_{ap} - R_p}{R_p} = \frac{2P_1P_2}{1 - P_1P_2} \tag{1.1}$$

where R_p and R_{ap} are the junction resistance with parallel and anti-parallel magnetic configuration, and P_i is the spin polarization of FM at the Fermi level defined as:

$$P_i = \frac{N_\uparrow^i - N_\downarrow^i}{N_\uparrow^i + N_\downarrow^i} \tag{1.2}$$

where $N_\uparrow^i$ and $N_\downarrow^i$ are the DOS of spin $\uparrow$ and $\downarrow$ of the material i at the Fermi level.

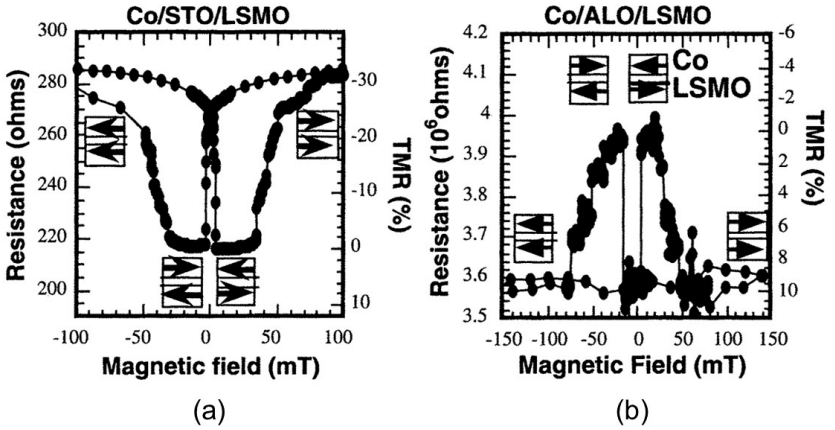

Figure 1.2: TMR curves obtained at bias voltage of -10mV, and at 40K (a) $Co/SrTiO_3(STO)/LSMO$, (b) $Co/Al_2O_3(ALO)/LSMO$ junction. Opposite signs TMR are observed with identical LSMO and Co ferromagnetic electrodes, Figures are reprinted from [11]

.

The sign of TMR effect depends thus on the sign of the product between the spin polarizations of the two electrodes. Association of two ferromagnetic electrodes with opposite spin polarizations at the Fermi level will cause a negative TMR amplitude, i.e. a junction resistance higher in the parallel magnetic configuration than in the anti-parallel state.

1.1.1.2 Limitations of Jullière's model

Jullière's model succeeded to predict quantitatively the TMR amplitude in inorganic MTJs based on classical ferromagnets bulk spin-polarization values. However, new insights on the physics of spin-dependent tunneling were pointed at after the breakthrough experiments of De Teresa et al. [11], in 1999. They studied the effect of barrier choice on determination of the magnetoresistance signals in $Co/Insulator/LSMO((La,Sr)MnO_3)$ systems. They illustrate that magnetoresistance signals can be modified by the choice of the insulating layer. The TMR curves of $Co/SrTiO_3(STO)/LSMO$ and $Co/Al_2O_3(ALO)/LSMO$ tunnel junctions are displayed in Figure 1.2a and b, respectively. An inverse TMR ($R_{ap} < R_p$) was obtained for STO barrier, whereas a normal TMR ($R_{ap} > R_p$) was found for ALO barrier. According to Jullière's model, the TMR signal only depends on the polarizations of the

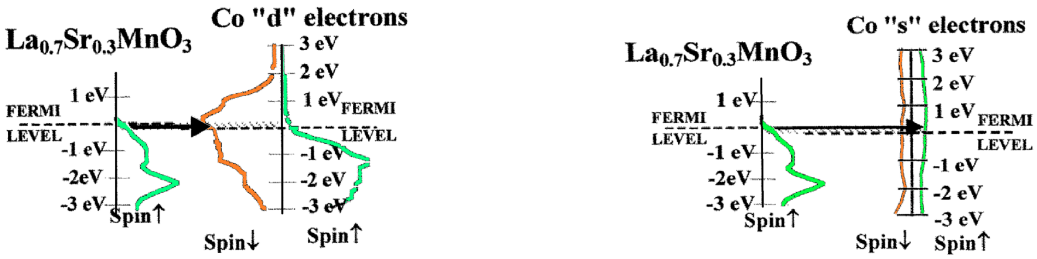

(a) (b)

Figure 1.3: DOS of LSMO and Co, for d- and s-character electrons, the arrow represent the most probable tunneling transition (a) STO/Co interface selects d-bands of Co resulting in a negative TMR. (b) Al_2O_3/Cointerface would select s-bands of Co resulting in a positive TMR. Figure reprinted from [11].

.

ferromagnetic electrodes. Therefore, since the FM electrodes are identical in both systems, same TMR signals are expected. The observed difference can thus only be explained by the fact that the insulating material influences the spin polarization of the tunneling current and therefore defines the sign of the TMR.

Figure 1.3 displays the LSMO and Co density of states of the d- and s-character electrons. LSMO is a half-metal presenting a full spin-polarization at the Fermi level (P=+100%). Therefore, the TMR sign was used to probe the spin polarization of Co at the Fermi level when coupled to different insulating barriers. The negative polarization of Co when the barrier is STO can be viewed as a preferential transmission of electrons of d character at the Co-STO interfaces, shown in Figure 1.3a. The positive polarization when the barrier is ALO has been ascribed to the selection of s character electrons by bonding effects at the Co-ALO interface, Figure 1.3b.

1.1.2 Molecular Spintronics

Organic spintronics emerged in 2002 with the pioneer work presented by the group of C. Taliani and A.V. Dediu [12] on a lateral LSMO/sexithienyl/LSMO junction. Organic materials have brought major advantages to spintronics. They can be resumed in the potentiality to implement flexible, low production cost and easy-processing electronics. However, the main advantage that

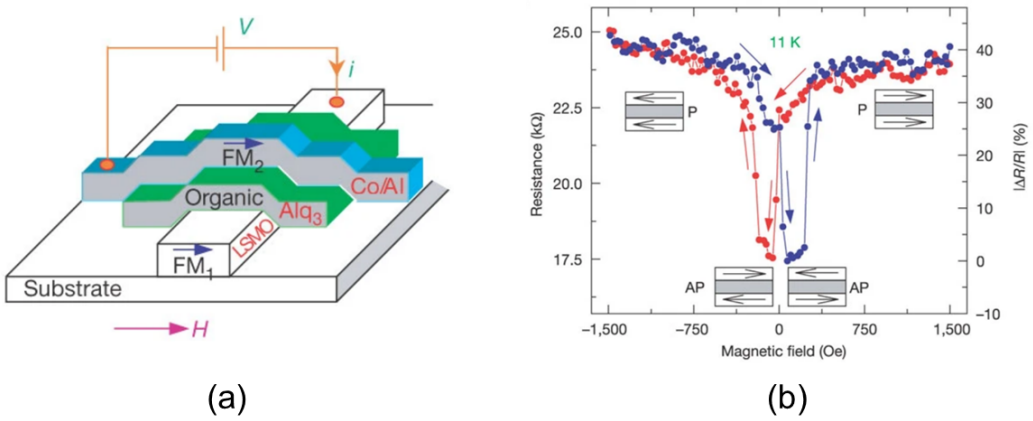

Figure 1.4: (a) Schematic structure of an organic vertical spin valve $LSMO/Alq_3/Co$, (b) MR curve measured of a $LSMO/Alq_3(130nm)/Co$ junction at 11 K, Figure reprinted from [16].

initially attracted much of the attention to organic materials is their expected longer spin lifetime [13, 14]. This effect is expected due to the weak spin-orbit and hyperfine interactions [15]. The spin-orbit coupling grows with the atomic number Z like Z^4. Organic materials are composed of low-weight atoms leading to low spin-orbit coupling. Importantly the spin-orbit effect is responsible for spin-precession and the loss of spin-coherence. Another important interaction, which generally leads to spin-decoherence, is the hyperfine interaction between electron and nuclear spins. The molecules used for spin-transport are π-conjugate molecules where the transport is mostly through molecular states localized over the carbon atoms. Carbon, in its most abundant isotopic form, ^{12}C, has zero nuclear spin, and therefore is not hyperfine active. Moreover the π-states are usually delocalized and hyperfine interaction can be anyway rather small. As a consequence of low spin-orbit coupling and hyperfine interaction in organic systems, the spin information can be potentially maintained for a long time.

In 2004, the first MR signal was observed in a vertical organic spin valve formed of $LSMO/Alq_3(130nm)/Co$ by the group of Z.V. Vardeny [16]. As shown in Figure 1.4, a negative magnetoresistance of -40% was observed at 11 K. The high resistance state can be identified as the parallel magnetic

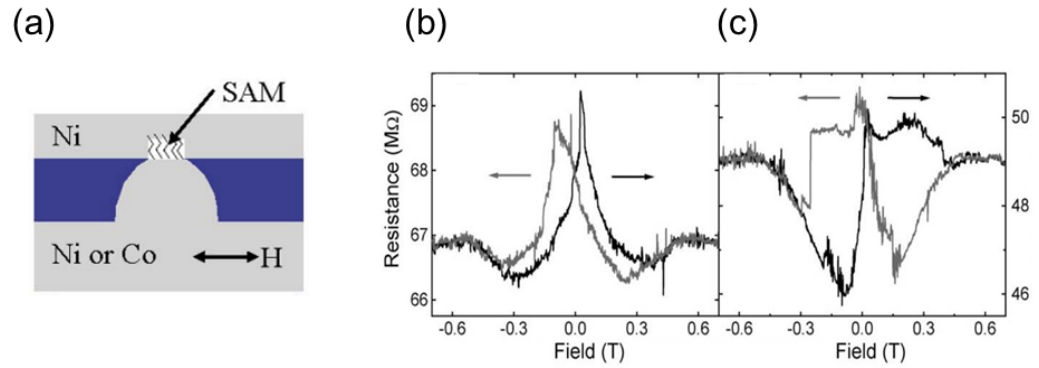

Figure 1.5: (a) Schematic structure of molecular MTJ using SAMs, (b) and (c) different resistance behaviour measured of two $Ni/octanethiol/Ni$ junctions as a function of in-plane magnetic field at 4.2 K with a bias of 10 mV, Figures are reprinted from [17].

configuration between the two FM electrodes, while the low resistance state corresponds to the anti-parallel one.

In parallel, first effects to characterize spin transport through mono molecular layers were reported.

The first result in this direction using organic self-assembled monolayer (SAMs) was presented by Petta et al. in 2004 [17]. A $Ni/octanethiol/Ni$ magnetic tunnel nanojuction was studied where the diameter of nanopores was 5-10 nm. The magnetoresistance curves were measured at 4.2 K, displayed in Figure 1.5. Positive and negative junction magnetoresistance, $JMR_+ = (R_{max} - R_p)/R_p = +3.5\%$ and $JMR_- = (R_{min} - R_p)/R_p = -6.1\%$, were calculated from measured resistance as a function of magnetic field, presented in Figure 1.5. Authors suggested that the presence of defects inside the organic monolayer as a possible reason of variable magneto-transport properties from one junction to the other.

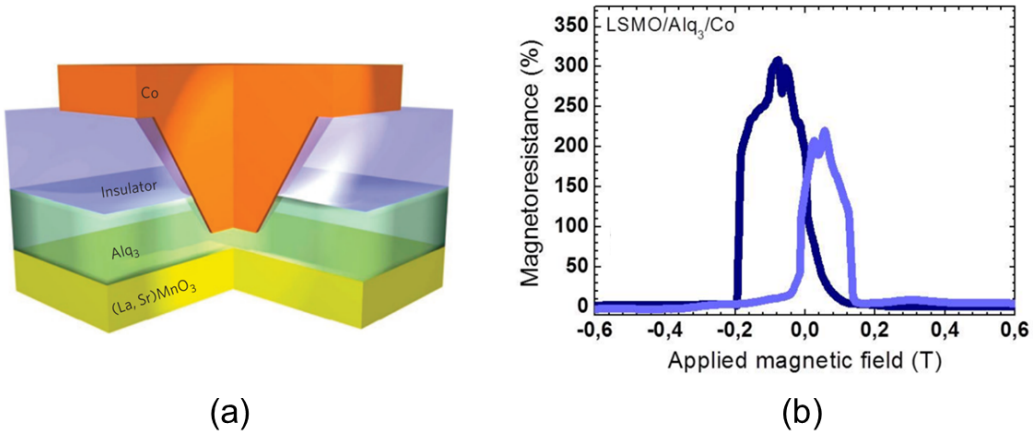

Figure 1.6: (a) Schematic structure of a nanometric-size MTJ of $LSMO/Alq_3/Co$, (b) MR curve measured of a $LSMO/Alq_3(2nm)/Co$ junction at 2 K and -5 mV, Figure reprinted from [18].

1.2 The Spinterface concept

In 2010, the spin-dependant hybridization at the ferromagnet/molecule interface was brought into light by C. Barraud and his colleagues [18]. In this study, a nanometre-scale $LMSO/Alq_3(2nm)/Co$ magnetic tunnel junctions exhibits a positive magnetoresistive response of up to 300% at 2K, displayed in Figure 1.6. Although, a negative TMR had been measured for a same structure spin-valve with different thickness barrier, $LSMO/Alq_3(130nm)/Co$, shown in Figure 1.4. As a consequence, the magneto-resistance property of molecular spintronic devices was found to be highly sensitive to the FM/Mol interface. To explain this apparent discrepancy, C. Barraud et al. proposed a model to take into account the role of interfacial spin-dependent metal/molecule hybridization on the effective spin polarization. This study indicates that depending on the electronic coupling strength between molecules and FM electrodes, the spin polarization at the interface between the ferromagnet and the molecules can be enhanced [19] or inverted [20]. These interface hybridization effects thus govern the magneto-transport properties and were quickly demonstrated as "spinterface" effect [21].

1.2.1 Ferromagnetic metal/molecule interaction: spinterface formation

To investigate the spinterfaces of MTJs, the FM/Mol interface electronic interactions have to be considered. To graft a molecule on a ferromagnet, we first consider uncoupled FM band structure and molecular level separated by vacuum, displayed in Figure 1.7-1. Molecules being isolated, the lifetime of this electronic molecular state is infinite, and its energy ϵ_0 is precisely known. Qualitatively, by bringing the molecule in proximity with a metallic electrode, the isolated molecular level couples with the continuum of electronic states of the metal, Figure 1.7-2. In this case, the charge has now a certain probability to escape from the molecular level to the metal. Hence, the lifetime (τ) of the molecular level becomes finite, resulting in energy broadening of the molecular orbital (Γ). Depending on the strength of the interaction this broadening can range from below the meV up to the eV range [22]. Another major effect is an energy shift, ΔE,of the molecular level from the initial position of the isolated molecule, also results from the interaction with the metal [23]. We highlight that this metal layer is also ferromagnet. On this account, the spin unbalance in the DOS of the metal is also reflected on the molecule, resulting in a spin-dependent energy shifting, $\Delta E^{\uparrow\downarrow}$ and energy broadening $\Gamma^{\uparrow\downarrow}$. This spin-dependent energy shift depends for instance on the adsorption geometry.

Spin polarization inversion is expected to happen for intermediate to strong coupling, Figure 1.7-2a [20], when $\Gamma^{\uparrow\downarrow} \gg \Delta E^{\uparrow\downarrow}$. In this case, the frontier orbitals of the grafted molecule are close to E_F and acquire a spin-polarization opposite to the FM spin-polarization, resulting in a TMR sign inversion. On the other hand, in the case of a weak interface electronic coupling between molecule and FM, $\Gamma^{\uparrow\downarrow} \ll \Delta E^{\uparrow\downarrow}$, the LUMO states acquire same spin polarization but remains above system Fermi level. In that case (Figure 1.7-2b), electron tunneling through the molecular layer will see a spin-dependent tunnel barrier height resulting in efficient spin-filtering. The observed TMR is in that case amplified [19].

Summarizing, it is demonstrated that the spin response can be strongly modulated by the hybridization at the interface. In the next section, some experimental evidences of the significance of spinterface are presented.

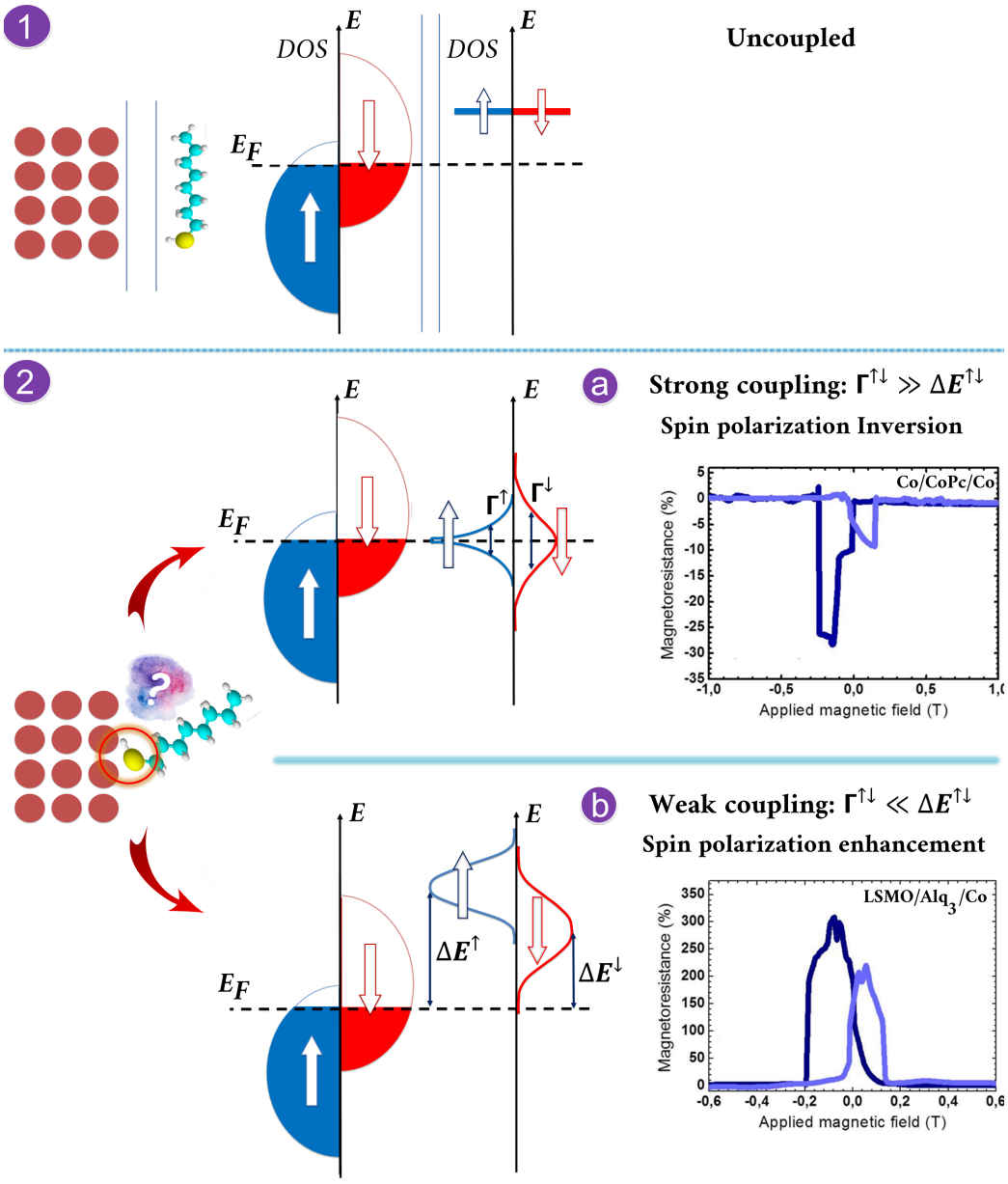

Figure 1.7: Schematic spinterface effect of a hybrid junction, 1- a magnetic material and a molecule far apart, the DOS is the superposition of the isolated systems, 2- molecule interaction with FM, leading to broadening and spin-dependent energy shifting of molecular orbitals, a) and b) Tunneling magnetoresistance (TMR) experiments highlighting (a) the possible inversion and (b) the enhancement of the spin polarization of the molecular levels depending on the strength of the interface hybridization. Figures are adapted from [20] and [19], respectively.

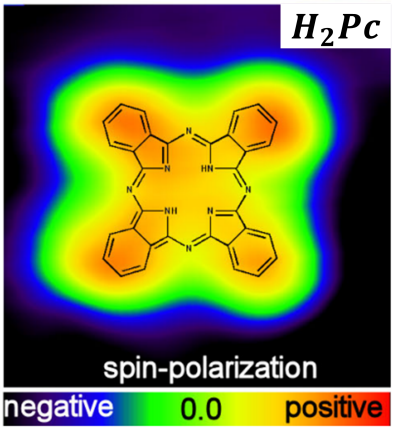

Figure 1.8: Spin polarized scanning tunneling microscopy experiment employed to image the spin polarization of a H_2Pc molecule deposited on an iron surface at 6K. The opposite surface spin polarization of iron (negative) and spin polarization above the molecule (positive) highlights the spin polarization inversion on the H_2Pc orbitals, figure is reprinted from[20].

1.2.2 Experimental proofs of spinterface effects

Several experimental investigations on the spin dependent hybridization have been pursued on FM/molecules interfaces, employing different spectroscopic techniques. N. Atodiresei et al. have studied organic molecules with significantly different reactivities absorbed on a Fe(001) surface by spin-polarized STM (SP-STM) technique [20]. The spin polarization of a H_2Pc molecule adsorbed on out-of-plane magnetized Fe is imaged at 6K, shown in Figure 1.8. In this study, a strong interaction occurs between the carbon's p_z atomic orbitals of phthalocyanine molecule and the d states of the iron atoms resulting in an amplification of the inversion of the spin polarization above Fermi level (Figure 1.8), compared to the free Fe surface.

The spin dependent energy shifting of the molecular orbitals at the ferromagnetic interface has also been directly measured on C_{60} molecules deposited on chromium surface by SP-STM at 5K [19]. A strong interaction between single C_{60} molecule and Cr(001) surface has been observed, resulting in spin-splitting of a LUMO derived state close to the Fermi level. This spin-splitting was probed by spin-polarized scanning tunneling spectroscopy (SP-STS), displayed in Figure 1.9. The extracted TMR values calculated from this measured spectra confirms spin-polarization enhancement in this

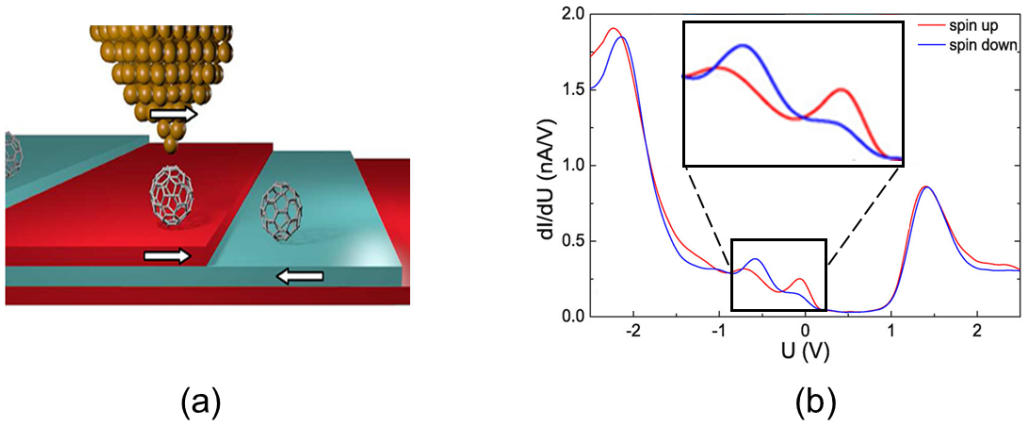

Figure 1.9: Spin-polarized scanning tunneling spectroscopy measurements on a C_{60} molecule deposited on a chromium surface. (a) Schematic view of the STM junction. (b) The difference in the conductance curves for the spin up (red) and down (blue) shows a spin dependent energy shifting of the molecular levels up to 0.5 eV, figure is reprinted from [19].

system, reaching to values of 100%.

F. Djeghloul et al. have explicitly measured the interface contribution to the spin polarized DOS for phthalocyanine monolayers on Co(001) [24] by Spin-resolved photoemission spectroscopy. A strong spin polarization of $\approx$ +80% at room temperature is revealed at E_F, shown in Figure 1.10, whereas spin-polarization of bare Co at Fermi level is opposite in sign.

To conclude, we have seen through a selection of experimental studies on model molecule/ferromagnet systems that the interface spin-polarization is intimately dependant on hybridization effects. Those spinterface effects are a major challenge to understand spin-dependant transport in hybrid MTJs but can also be considered as an opportunity to engineer magnetoresistance systems with high MR values. However, exploiting spinterface effects in fundamental devices requires first the preparation of model MTJs integrating a self assembled monolayer between two ferromagnets which is still a highly challenging experimental issue.

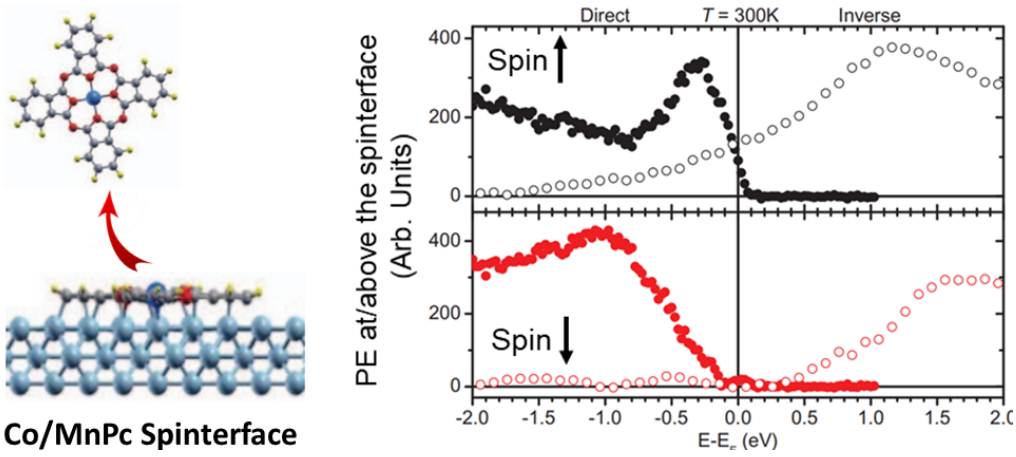

Figure 1.10: Spin-resolved spectra of direct (closed symbols) and inverse (open symbols) photoemission spectroscopy at room temperature of Co/MnPc. A high interface spin polarization of phthalocyanine (MnPc) molecules on Co(001) is widened at Fermi level, figure is reprinted from [24].

1.3 Experimental challenges and objectives of this work

From experimental perspective, fabrication of a vertical functioning molecular MTJ is limited for several reasons. To designate one of the limitations of these systems, we highlight the frangibility of a grafted molecular layers resulting in extremely damageable junctions. The oldest and most crucial challenging aspect of MTJs fabrication is top-electrode penetration through the molecular layer, subsequent to short-circuits in MTJs. In schematic Figure 1.11, we show the formation of FM top-electrode gradually onto SAMs. The deposited metal atoms contain a certain kinetic energy which leads to locally destroying the SAMs order. This disturbed SAMs opens room for metal diffusion, inevitably leading to short circuits. Fabrication of pinhole-free molecular MTJs have remained a tremendous struggle in this field.

To avoid the metal penetration, numerous approaches have been introduced to contact SAMs in Au/SAMs/Au devices, reviewed in [25], such as transfer printing [27, 28, 29], cross wires junctions [30, 31], direct conducting AFM [32, 33, 34], spin-coating of conductive polymer [35, 36], direct evaporation [37, 38, 39, 40], indirect evaporation [41, 42], nanopores [43, 44]. Some of

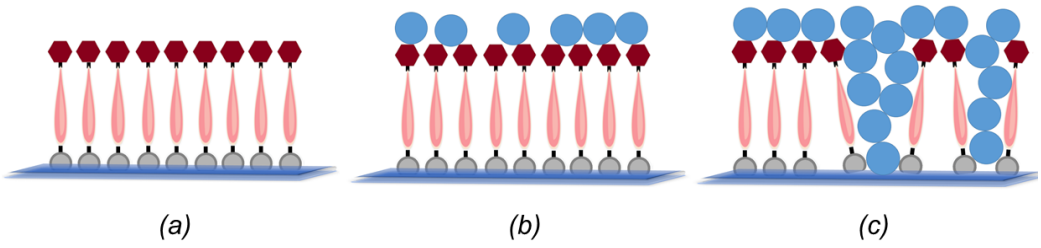

Figure 1.11: Schematic top-electrode deposition onto a grafted substrate, a) grafted substrate by SAM, b) formation of metal top-electrode, c) metal diffusion due to high kinetic energy of metal atoms through SAM.

these methods are briefly presented in Figure 1.12. While various contacting approaches and architectures have been proposed to contact the molecules, there are very few that are are realistic for large scale integration. Furthermore, even less are compatible with ferromagnetic materials. Commonly used transition metal ferromagnets (Fe, Co, Ni and their alloys) are indeed highly reactive with oxygen and will form a surface oxide layer in air that is redhibitory for the preparation of model MTJs. SAM grafting on such reactive metallic surfaces is thus much more challenging than on non-reactive Au surface. Even the presence of nanometric oxide patches at the metallic FM surface will result in local poor grafting of the thiol linker group leading to SAM discontinuities. To overcome this issue, two approaches were proposed and consist in grafting the FM reactive surface in controlled environment, i.e. either under inert atmosphere in a glove box or under ultra high vacuum. Once the issue of interface oxidization is solved, the preparation of MTJs will also require patterning of small area tunnel contacts by lithography to increase the probability of achieving pinhole-free junctions.

Nanoindentation lithography technique method has been successfully developed to fabricate MTJs by UMPhy laboratory [45]. This method consists in the notching of a nanohole into an electrical insulator layer by using a conductive tip AFM (CP-AFM) to define the nanometric size of the device. A solution of glycolic acid diluted in anhydrous ethanol is used to eliminate the oxidization of bottom-electrode (NiFe) in a glove box with inert atmosphere. Glycolic acid is also employed to avoid any possible reoxidation of the NiFe during molecular grafting of the SAMs in solution. The grafted NiFe is transferred for top-electrode deposition under an inert atmo-

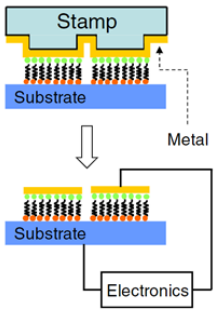

Transfer printing: a metal-coated stamp is brought into mechanical contact with a monolayer-coated substrate, with a reactive termination group. This high reactivity in regard to the metal adhesion to the stamp leads to a transferred pattern once removing the stamp.

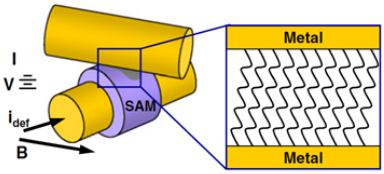

Crossed wires: the SAM is sandwiched between two crossed wires to form the junction.

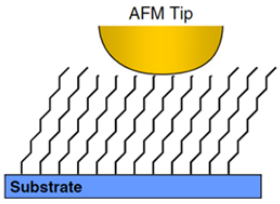

Direct conducting AFM: formation of monolayer junction using a metal-coated (conducting) AFM tip.

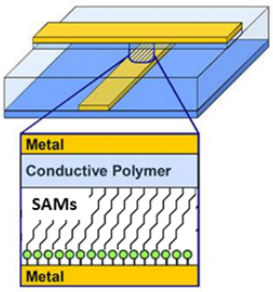

Spin-coating of conductive polymer: a conductive polymer as PEDOT-PSS is spin-coated over the SAM and acts as top electrode in the junction.

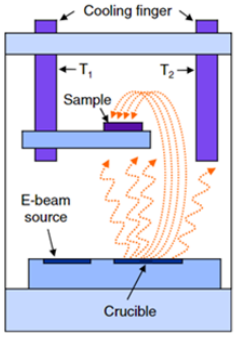

Indirect evaporation: for the top-electrode deposition, samples are placed facing away from the crucible. Indirect deposition of low energy adatoms prevents pinhole formation.

Figure 1.12: Some commonly used methods to contact SAMs [25].

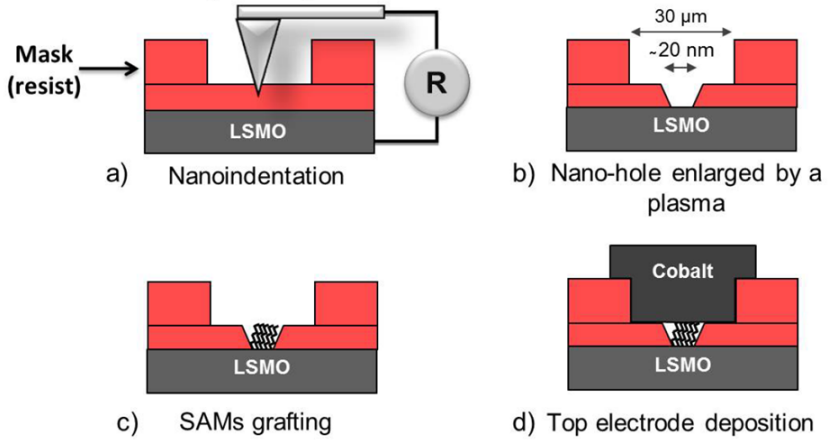

Figure 1.13: Schematic of a $LSMO/SAM/Co$ device fabrication. (a) Nanoindentation lithography technique: LSMO spin-coated with a resist which is indented by an AFM tip to form a nanohole, (b) O_2 plasma is used to enlarge the nanohole to a final diameter of 10-50 nm, (c) SAM grafting process: immersing the sample in a SAM solution, (d) Co top-electrode deposition by sputtering. figure is reprinted from [26]

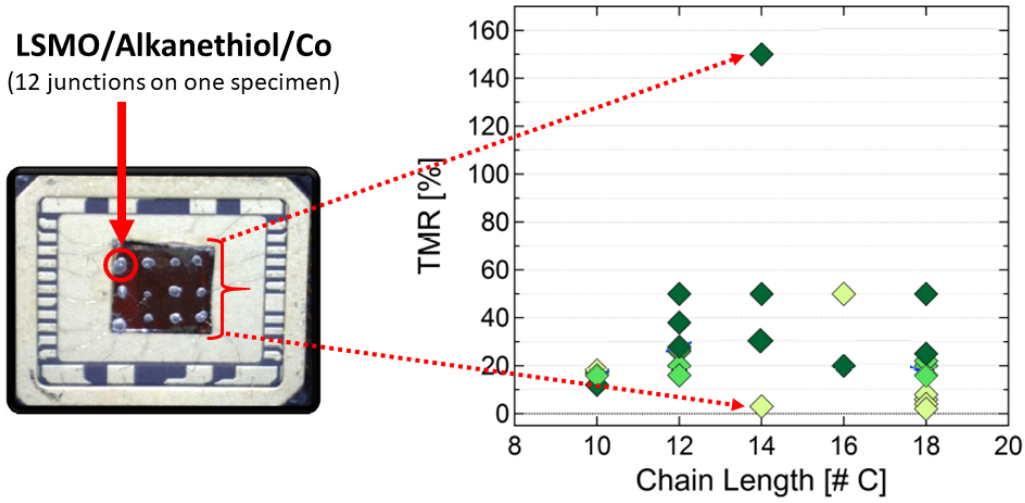

Figure 1.14: TMR measurements on $LSMO/Alkanethiol/Co$ systems from C10, C12, C14, C16 and C18 (in the right), different TMR amplitudes have been detected from one specimen containing 12 junctions (in the left), figure is adapted from [26].

sphere using a vacuum transfer chamber. This technique, which is briefly explained in Figure 1.13, junctions of diameter $10 - 15nm$ [46] has led to 30% functional molecular MTJs. Recently, a similar approach was used in the same group to define large area MTJs by replacing the nano-indentation process by laser lithography. The coresponding junction diameter can be controlled in the 400-800 nm range while maintaining a typical 30% ratio of the prepared junctions presention non-linear I(V) curves. However, in both methods (Nanoindentation/laser lithography), a broad distribution of TMR amplitudes can be observed on the sames stack or even on various junctions on the same sample, pointing at a possible imperfect control of spinterfaces (Figure 1.14) even at this submicronic scale. Local disorder in molecular orientation in the SAM or partial atomic diffusion in the molecular layer could result indeed in such spinterface inhomogeneities.

Another elegant MTJs patterning method was developed in IPCMS (Strasbourg) based on nanosphere lithography [47], Figure 1.15. $Co/Pc/Co$ MTJs integrating a thick (20nm) Co-phthalocyanine (CoPc) organic layer was deposited using sputtering of the cobalt electrodes and organic molecular beam epitaxy (OMBE) of the organic spacer. The junctions were then ex-situ patterned using SiO_2 nanobeads (diameter 500nm) as a solid mask to etch nanopillars using dry argon etching. This method also allows to prepare submicronic MTJs with interfaces prepared under controlled environment, but, to the best of our knowledge, for relatively thick organic layers only.

To conclude, despite major progresses in the development of hybrid MTJs integrating an insulating organic monolayer as a tunnel barrier, the molecular spintronics community is still facing several issues to prepare model systems. Small area junctions are still necessary due to the common formation of electrical shorts during deposition of the top ferromagnetic contact on the SAM. Even in the submicronic range, majority of the prepared junctions can be ohmic, and MTJs presenting a tunneling behaviour can present a broad range of magneto-transport properties.

In this framework, the objectives of this Ph.D. thesis is to contribute to the development of model hybrid MTJs. For this purpose, we propose:

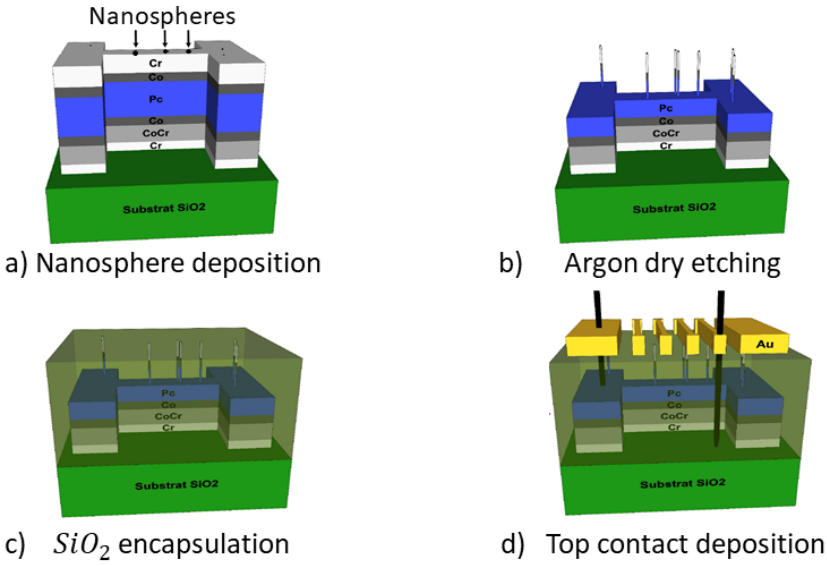

Figure 1.15: Schematic of a $SiO_2//Cr/CoCr/Co/Pc/Co/Cr$ device fabrication by Nanosphere lithography technique. (a) nanosphere deposition on the surface, (b) Ar etching: tailoring the nanopillars protected by the shadow-masking nanospheres, (c) Passivation layer deposition: it serves to electrically decouple the parallel pillars with the same common bottom electrode (this layer is removed from the nanoshperes using N_2 gun), (d) Top-electrode deposition, figures are adapted from [47].

i to use single-crystalline bottom ferromagnetic electrode grown by molecular beam epitaxy. This epitaxial FM with well-defined electronic properties (spin-polarization) and oxide-free surface is an ideal starting point for model MTJs.

ii to graft the bottom electrode under ultra-high vacuum environment using vapor phase method in a chamber connected to the MBE to prepare dense, oxide-free SAM with a high degree of organisation.

iii to develop a soft-landing deposition method of the top FM electrode allowing the formation of pinhole-free junctions over extended areas.

iv to develop complete in-situ patterning of the MTJs in the cross-bar geometry by using shadow-mask deposition. This method will allow preparing MTJs with optimal interface, without any technological process after junction deposition.

The manuscript is organized as follow:

Chapter 1.3 is dedicated to the presentation of the experimental tools used in this study. We use extensively electron spectroscopy XPS/UPS to characterize the grafting, the cleanness of the interfaces and the electronic properties of the interface. An original scanning probe technique BEEM was also used to characterize the homogeneity of the contact, and will be also presented.

Chapter 2.2.4 is focused on preparation of the bottom electrode. Grafting quality on several FMs as a potential bottom-electrode is thus studied by XPS. Moreover, the investigation of electronic band structure for FM and FM/SAM systems is presented.

Chapter 3.3 is devoted to controlled top-electrode deposition on SAM. BLAG technique is introduced to provide top-electrode atoms soft-landing on SAM, preventing the formation of short circuits. The BLAG method is validated macroscopically and microscopically employing XPS and BEEM/STM

respectively. Moreover, the electronic band alignment of these heterojunctions are investigated using UPS and BEEM.

Chapter 4.4.2 illustrates transport properties of large area cross-bar geometry MTJs. We focus on study of shadow-mask deposition using optical microscope and AFM. The chapter is carried on by investigation of magnetic properties of top- and bottom-electrode. However, the magneto-transport investigation for this specific geometry MTJs is challenging and still under progress.

2

XPS and BEEM techniques

Introduction

The control of each steps of the sample production relies on the surface and interface analysis techniques available in the laboratory. This chapter will be dedicated to the two main employed techniques. The photoemission technique allows to obtain information on the chemical species present on the surface. Therefore, it permits checking the quality of the grafted molecular layers on a substrate. To complete the study of these heterostructures, an interface analysis technique is required. Ballistic Electron Emission Microscopy (BEEM) is a scanning probe technique which allows to probe at the nanoscale electron transport through heterostructures. In the case of metal top contact deposited on SAM, BEEM allows to detect the diffusion of the top electrode through the molecular layer (pinholes). Thanks to BEEM technique, the information about the band alignments of the system is also provided. Both techniques will be discussed in more details in the following chapter.

2.1 Photoemission techniques

X-Ray Photoelectron Spectroscopy (XPS) and UV Photoelectron Spectroscopy (UPS) are quantitative techniques for measuring the elemental composition of the surface. They give access to the valence and the core electronic levels of the material surface. Therefore, they provide information about the

quality of the grafting of molecular layer on a substrate. In particular, the experimental coverage rate of the organic molecules on the surface can be obtained quantitatively. In the following chapter, I will briefly introduce these techniques as well as the common used models, and finally the experimental setup.

The theoretical aspects of photoemission presented here are targeted according to the studies carried out in the rest of the chapter.

2.1.1 Photoemission process

Photoemission spectroscopy consists of irradiating a sample with a photon, in order to extract an electron by the absorption of a quantum of light. This phenomenon corresponds to a photoelectric process which was discovered in 1887 by Frank and Hertz, and explained in 1905 by Einstein [48, 49, 50]. The choice of X-ray sources as excitation beams comes from their ability to probe the core-level electrons. Complementary, employing UV sources gives access to valence electrons of our system. The photoemission spectroscopy measurements are based on the analysis of the kinetic energy of the extracted photoelectron. In fact, the measurement of the kinetic energy of the photoemitted electron allows to determine the binding energy of the electronic state where it comes from, by using the following energy conservation law.

$$h\upsilon = E_B + E_K \tag{2.1}$$

where E_B corresponds to the binding energy of the photoelectron, E_K its kinetic energy , h the Planck constant and υ the frequency of the excitation photon beam.

This process is easily described in the three-step model [51], which breaks up the photoemission process into three steps:

2.1.1.1 Photoexcitation

The surface irradiation of a sample with photons excites the electrons in the zone of penetration of the photon beam, due to photon absorption. After absorption of a photon, an electron of the sample can be extracted with a given kinetic energy. This extraction creates a hole in the atomic core-level. The photon excitation must have an energy higher than the electron binding energies, for the atomic ionization to occur.

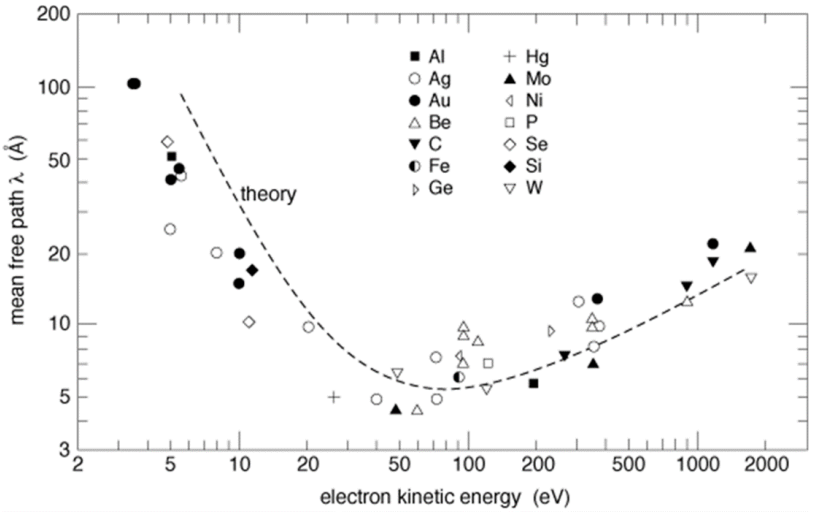

Figure 2.1: Evolution of the electron mean free path with respect to their kinetic energies.

2.1.1.2 Propagation

The photoexcited electrons propagate within the solid to reach the surface, which involves elastic and inelastic mechanisms. The average length between two consecutive inelastic scattering events is called the mean free path and is noted by λ. It is of the order of a few tens of angströms, and depends in particular on the kinetic energy of the electrons and on the nature of the medium traversed that leads to the universal curve shown in 2.1. [52]. This figure demonstrates the surface sensitivity of photoemission spectroscopy. This technique allows us to probe the grafted molecular layer on the surface as the thickness of these layers are estimated in the same order as the electron mean free path.

2.1.1.3 Escape of the photo-excited electrons from solid to vacuum

Finally, the photo-excited electrons with enough energy cross the potential barrier that represents the surface of the solid. This crossing costs electrons a certain amount of energy which is the sample work function Φ_s. Consequently, the kinetic energy of the electrons which escape from the solid is

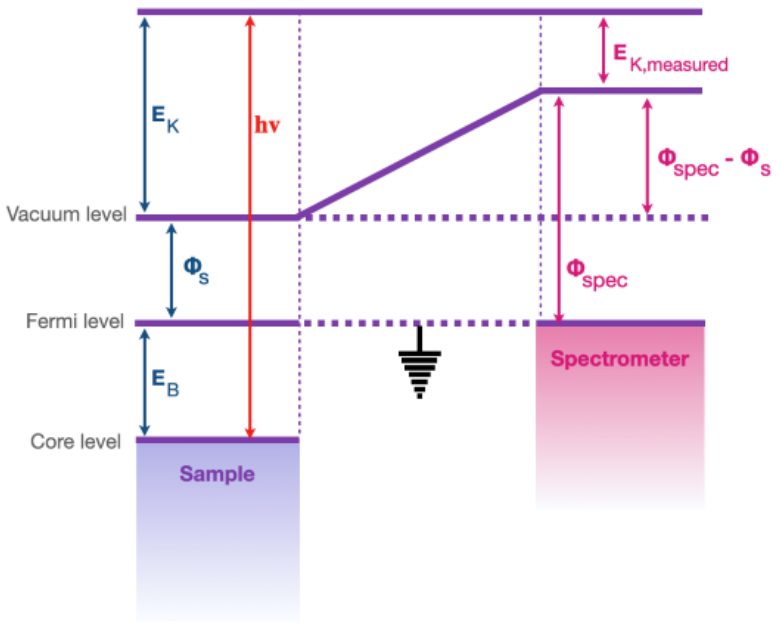

Figure 2.2: Scheme of the energy configuration taking place in a photoemission experiment where the spectrometer is electrically connected to the solid sample.

given by:

$$h\upsilon = E_B + E_K + \Phi_s \tag{2.2}$$

where Φ_s, sample work function, is the energy needed to promote an electron from the sample Fermi level to the vacuum level.

The sample and analyzer being electrically grounded has the consequence to align the Fermi level of the spectrometer and the sample of interest, Fig. 2.2. Hence, the kinetic energy of an electron can be expressed as:

$$E_K = E_{K,measured} + \Phi_{spec} - \Phi_s \tag{2.3}$$

where Φ_{spec} is the work function of the spectrometer. The spectrometer used in photoemission spectroscopy is a hemispherical photoelectrons detector which counts the number of photoelectrons emitted by the sample with a given kinetic energy.

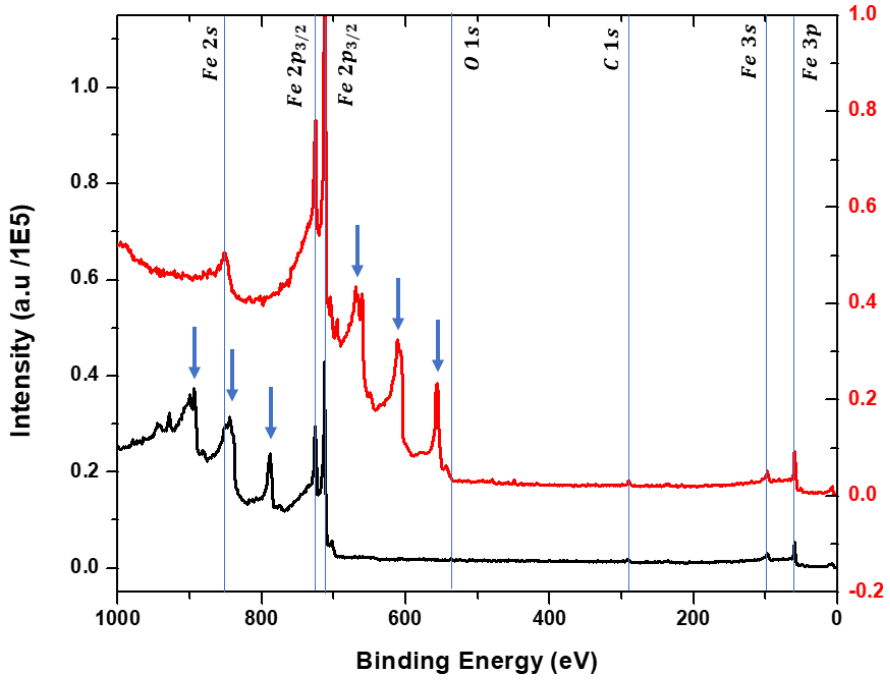

Figure 2.3: XPS spectra of Fe/MgO(001), with Al-Kα (black line) and Mg-Kα (red line) sources, Fe Auger peaks are marked with blue arrow observed with two sources, Fe, O and C core levels have been indicated by blue lines.

This equation allows the 2.2 to be expressed as a function of spectrometer work function (Φ_{spec}) in the following way:

$$h\upsilon = E_B + E_{K,measured} + \Phi_{spec} \tag{2.4}$$

The last equation (2.4) allows the determination of the binding energy of the photon-emitted electron for a given spectrometer with a well-defined Φ_{spec} work function. Thus, depending on the utilized photon energy, a window of levels is probed.

2.1.2 XPS spectra

A typical photoemission spectrum consists of plotting the number of photoelectrons which reach the detector in function of their kinetic energy. To identify the obtained peaks from the spectra regardless of the used photon source, they are represented as a function of the binding energy $E_B = h\upsilon -$

$E_{K,measured}$. Figure 2.3 presents the spectra obtained with the two sources Al-Kα (black line) and Mg-Kα (red line) on a surface of MgO(001)/Fe(001) before grafting the molecular species. These spectra identify the different core levels of Iron. The other peaks present (shown with blue arrows) correspond respectively to the Fe Auger peaks, which are located in different binding energies due to the employed source. The continuous background increases at higher binding energies, and corresponds to secondary photoelectrons having undergone inelastic scattering which are therefore detected at lower kinetic energies. In some cases, a close inspection of the energy positions of the core-level peaks can reveal binding energy shifts originating from a modification of the chemical environment of the emitting atomic species. In addition to that the photoemission peak intensity is proportional to the number of atoms involved in the photoemission process [51]. Consequently, the analysis of the photoemission peak intensities can give information about the amount of a grafted molecular species per unit surface.

2.1.3 Quantitative analysis of XPS spectra

Obtaining quantitative information is possible by analyzing the intensity of the detected signal. Therefore, spectra processing (PRESENTS software) is used to determine the intensity of the components by integrating the area under the peak after background subtraction. The shape of a photoemission peak can be described by a convolution of Lorentzian and Gaussian functions.

Case of an infinite layer

The photoemission signal elementary intensity of a layer with thickness of dz located at the depth of z from the surface, detected at angle (θ) from the sample surface normal, (notations defined in Figure 2.4) is given by:

$$dI_\theta(z) = \phi N \frac{A_0}{cos\theta} \frac{d\sigma}{d\Omega} \Omega_0 L T(E_K, E_{pass}) D(E_K, E_{pass})\ e^{-\frac{z}{\lambda cos\theta}}\ dz \qquad (2.5)$$

where ϕ corresponds to photons flux, N to the number of atoms per unit of volume, $\frac{A_0}{cos\theta}$ to the analyzed surface, $\frac{d\sigma}{d\Omega}$ to the photoionization cross section, Ω_0 to the angular acceptance of analyzer, L to the emission anisotropy (constant depending on source and analyzer orientation), $T(E_K, E_{pass})$ and

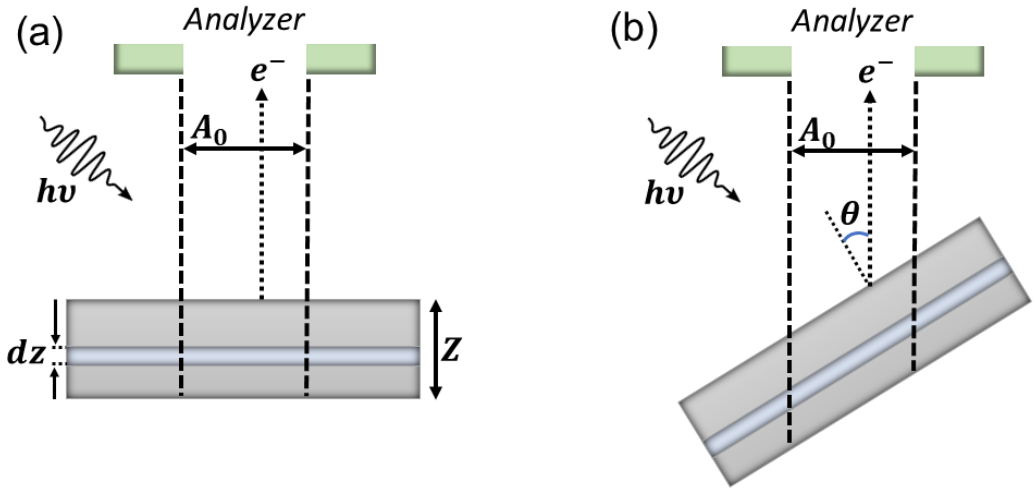

Figure 2.4: Schematic diagram of the system geometry during photoemission measurement (a) for normal detection and (b) for a detection angle (θ) to the surface normal.

$D(E_K, E_{pass})$ ascribe to the terms of transmission and detection of the analyzer (dependent on the kinetic energy E_K of the electrons and the used pass energy E_{pass}), and the exponential term corresponds to the attenuation undergone by the electrons in matter over a distance z.
In the case of an infinite thickness Z with respect to the analyzed depth (i.e. a thickness much greater than 3λ), the expression of the intensity becomes:

$$I_\theta^\infty = \phi N A_0 \frac{d\sigma}{d\Omega} \Omega_0 L \lambda T(E_K, E_{pass}) D(E_K, E_{pass}) \tag{2.6}$$

Case of a finite layer

For a sample of finite thickness Z, the intensity of the measured signal is obtained by integrating the equation 2.5, between the surface $z = 0$ and the thickness $z = Z$:

$$I_\theta(z = Z) = \phi N A_0 \frac{d\sigma}{d\Omega} \Omega_0 L \lambda T(E_K, E_{pass}) D(E_K, E_{pass}) \left(1 - e^{-\frac{Z}{\lambda cos\theta}}\right) \tag{2.7}$$

Thus, from equations 2.7 and 2.6, the intensity of the measured signal can be written as:

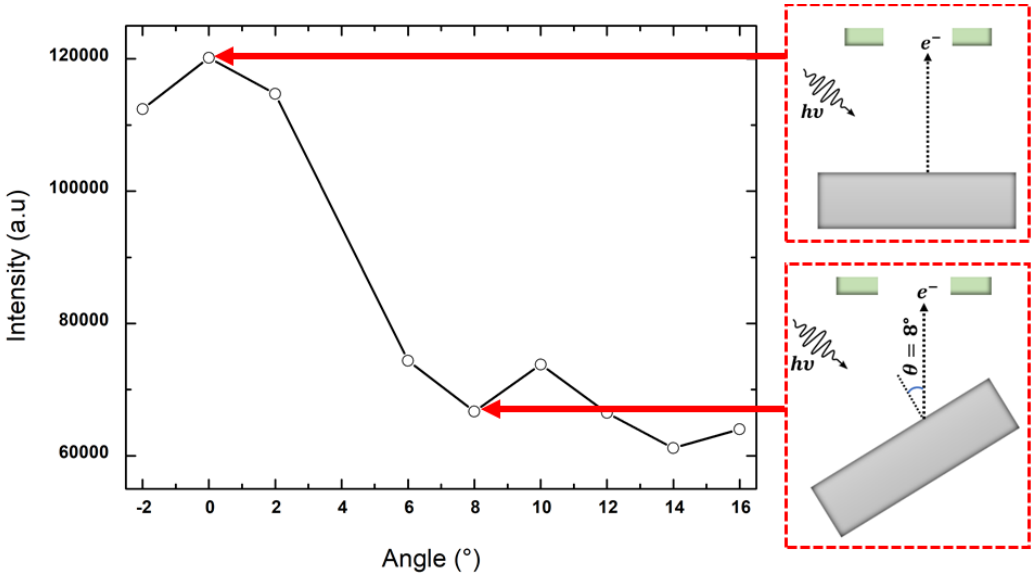

Figure 2.5: Angular measurements of Fe-2p core level, carried out by XPS on a Fe(001)/MgO(001) substrate before grafting the molecules.

$$I_\theta(z = Z) = I_\theta^\infty \left(1 - e^{-\frac{Z}{\lambda cos\theta}}\right) \tag{2.8}$$

In single crystalline systems, the measured signal is modulated by the diffraction of photo-electrons and is overestimated for analysis angles parallel to crystal high symmetry directions, known as X-ray Photo-electron Diffraction (XPD) effect. This overestimation is highlighted at normal measurements as shown by the angular analysis of the $2p_{1/2}$ level of a thick monocrystalline Iron layer in Figure 2.5, Fe(001)/MgO(001). The XPD effect is corrected by considering a corrected intensity calculated as the average between the measured signal at normal and the first minimum signal, at $\theta = 8°$ for Fe(001)/ MgO(001):

$$I_{0°} = \frac{I_{0°}^{overestimated} + I_{8°}^{minimum}}{2} \tag{2.9}$$

It is noted that no XPD effect was detected for poly-crystalline ferromagnets (poly-crystalline Fe and Co).

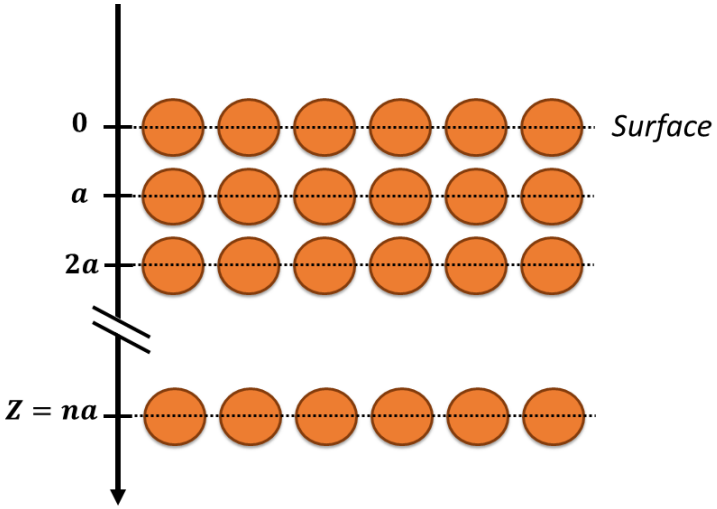

Figure 2.6: Schematic representation of atomic layers of a semi-finite material, used in discrete approach.

Discrete approach

The intensity of the core level photoemission peaks can alternatively be calculated using a discrete approach. In this approach, the specimen is composed of n atomic planes spaced by a distance a, displayed in Figure 2.6. For an homogeneous sample, each atomic mono layer is emitting the same elementary photoelectron intensity I_i^{ML}. The total intensity corresponds to the sum of the signal emitted by each of these planes, with quantified attenuation after propagation through a thickness ka (k integration between 0 and n-1):

$$I = I_i^{ML} \sum_{k=0}^{n-1} e^{-\frac{ka}{\lambda cos\theta}} \tag{2.10}$$

$$I = I_i^{ML} \left(1 + e^{-\frac{a}{\lambda cos\theta}} + e^{-\frac{2a}{\lambda cos\theta}} + ... + e^{-\frac{(n-1)a}{\lambda cos\theta}} \right) \tag{2.11}$$

That can be written as:

$$I = I_i^{ML} \frac{1 - e^{-\frac{na}{\lambda cos\theta}}}{1 - e^{-\frac{a}{\lambda cos\theta}}} \tag{2.12}$$

For a thick sample compared to the analyzed depth, $na \gg \lambda$, the measured intensity at normal becomes:

$$I = I_i^{ML} \frac{1}{1 - e^{-\frac{a}{\lambda}}} \tag{2.13}$$

From the measurement of the integrated photoemission peak, we can thus deduce the elementary value of I_i^{ML} which after normalization by the value of the photoionization cross section gives access to the surface concentration of element i.
This method will be used in Chapter 2.2.4 to determine the grafting ratio of the SAM on various ferromagnetic bottom electrodes.

2.1.4 XPS and UPS setup

The Photoemission measurements is performed in a multi-chamber ultrahigh vacuum (UHV) system, with base pressures at four 10^{-10} mbar (represented in Figure 2.7). This modified multi-chamber setup allows analyzing a fully *in situ*-prepared sample. Moreover, the XPS-UPS study is feasible at all stages of the process. The analysis chamber is equipped with non-monochromatized Al and Mg sources, in the form of a dual anode that produce both 1486.6 eV (Al-Kα anode) and 1253.6 eV (Mg-Kα) X-rays, which can be individually selected. The main advantage of two anodes for the X-ray source is to detect and possibly avoid electrons emitted by the Auger-Meitner process. Moreover, the chamber also has a helium discharge lamp, allowing to obtain photon energies of 21.2 eV (He I) and 40.8 eV (He II). Thanks to this complementary XPS-UPS setup, by providing the choice of the photon energy, it is possible to preferentially probe the core levels (X-rays) or the densities of states of the valence band (UV rays).

A molecular beam epitaxy (MBE) chamber is interconnected with the XPS analysis chamber via a transfer chamber. This MBE chamber is equipped

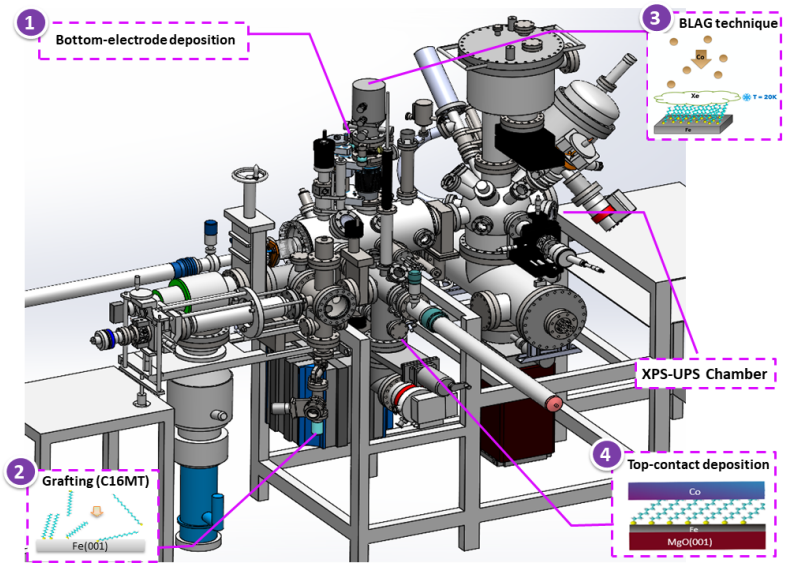

Figure 2.7: Photoemission Spectroscopy and sample preparation setup. (1) Bottom-electrode deposition: Metal deposition by MBE at room temperature, (2) Molecules grafting chamber (C16MT): Self Assembled Monolayers(SAMs) evaporation of molecules at room temperature into the chamber by means of a leak valve, (3) BLAG (Buffer Layer Assistance Growth) technique: Soft landing of the top contact, (4) Top-contact deposition: Evaporation growth through a shadow mask at RT or using BLAG.

for metal deposition at room temperature (Figure 2.7.1) and also at low temperature (20K)(Figure 2.7.3). Thicknesses of metallic films are determined using a quartz crystal microbalance. Thanks to a helium compressor connected to the preparation chamber, the substrate reaches 20K in 1 hour. This chamber is provided with a micro-leakage valve to introduce Xe gas (its crucial role in sample preparation will be explained). Additionally, a second transfer chamber eases the access to the grafting chamber under UHV, shown in Figure 2.7.2 . The grafting chamber is connected by a micro-leakage valve to a flask filled with a pure solution of alkanethiols (purity 95%, purchased from Sigma Aldrich). The leakage valve allows to control the vapor pressure of molecules on sample surface and grafting time.

2.2 Ballistic Electron Emission Microscopy

Ballistic Electron Emission Microscopy (BEEM) is an effective tool to investigate the nanoscale lateral homogeneity of electron transport through various heterostructures. BEEM also gives access to local measurements of potential barrier heights and is thus perfectly adapted to study fragile or heterogeneous systems such as SAM barriers integrated in a realistic device. BEEM was already successfully used to investigate $Au/alkanethiols/GaAs$ heterostructures during Alexandra Junay thesis in our group [53]. Specifically, BEEM imaging allowed to clearly identify the presence of pinholes in the SAM barrier, while BEEM spectroscopy could give access to the energy position of the lowest unoccupied molecular orbitals of the SAM (LUMO states). In the present work, BEEM was intensively used to assess the ferromagnetic Co top electrode deposition on the hexadecanethiol SAM with the ultimate ambition to achieve pinhole-free magnetic tunnel junctions with extended lateral dimensions. In the following, I will describe the principles of BEEM for the study of molecular barriers. I will then present the BEEM microscopy and spectroscopy operation modes and the classical theoretical models used to analyse the BEEM data. I will then illustrate the interest of BEEM to study SAM tunnel barriers in the case of previously studied $Au/alkanethiols/GaAs$ tunnel contacts [54, 55]. Finally, I will present the STM/BEEM experimental setup used in this work.

2.2.1 Principle of BEEM technique

BEEM is derived from scanning tunnelling microscopy (STM) and was originally developed in 1988 by Kaiser and Bell [56] to investigate the interface electronic properties of metal/semiconductors Schottky contacts. After an intensive use of BEEM to study various Schottky contacts [57], the technique was extended to the characterization of metal/insulator/semiconductor (MIS) tunnel contacts also for microelectronics applications [58, 59]. Finally, BEEM was also used to investigate monomolecular contacts and successfully applied to determine the energy position of the LUMO states of fullerenes deposited on Bi(111)/Si(001) [60]. This led to generalizing the application of BEEM to hybrid metal/SAM/semiconductor systems.

The principle of BEEM is presented in figure 2.8 for the specific case of a metal/SAM/semiconductor heterojunction with a n-doped semiconductor substrate. Electrons are injected from the STM tip (emitter) through the vacuum to the metal surface, with an energy simply defined by the tunnelling bias U_{gap} applied between tip and surface, defining the tunnel current I_T (typically few nA). Amongst the injected hot electrons traveling through the metal top layer (base), only a few percent of the injected current can reach the metal/SAM interface without energy loss. Those so-called "ballistic electrons" might cross the molecular barrier and enter the conduction band of the semiconductor substrate, either by tunnelling through the SAM (at low energy), or by propagating through the LUMO states of the molecules (at higher energy). In that case, a low magnitude BEEM current I_C (typically few pA) can be collected by an ohmic contact at the backside of the semiconductor substrate (collector).

Two modes of operation are used in a BEEM experiment. BEEM images $I_C(x, y)$ at a specific electron energy (defined by the chosen U_{gap} value) are obtained by measuring the collector current value at each pixel of the surface image while scanning the surface in the constant tunnel current mode. These BEEM images correspond to an electron transmission map at a given energy, and can be directly correlated with simultaneously recorded STM image. In the spectroscopy mode, the STM tip is stopped at a specific point of interest, and the $I_C(eU_{gap})$ spectra is collected while maintaining the tunnelling current constant. The BEEM spectra can give access to the local energy position of the LUMO state in the SAM and of the semiconductor conduction band minimum at the molecule/semiconductor interface.

Quantitative analysis of the BEEM spectroscopy curves can be performed

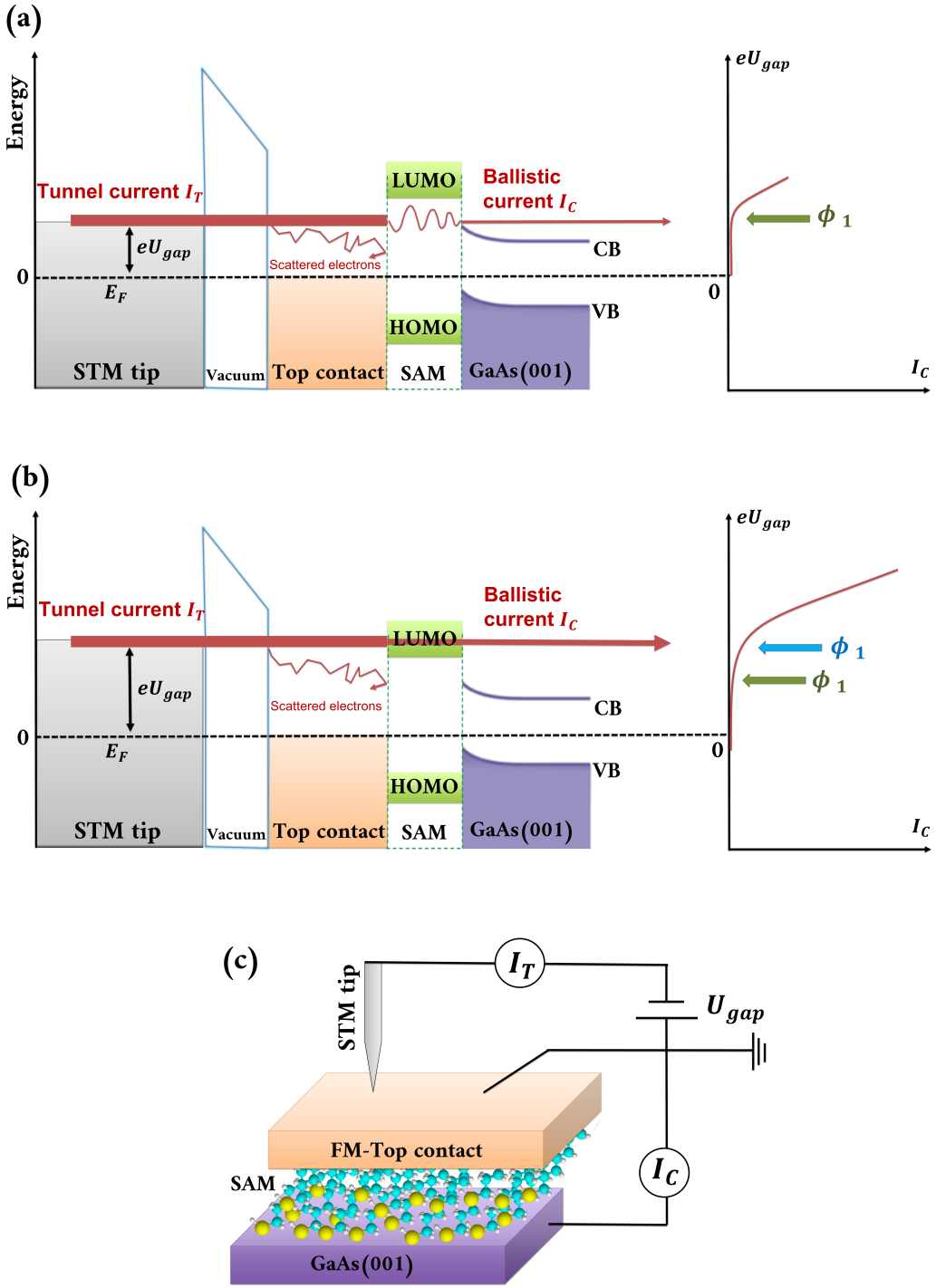

Figure 2.8: Schematic band diagram of a BEEM experiment on a Metal/Molecule/Semiconductor system, (a) so-called ballistic electrons tunnelling through the SAM (at low energy) with a low magnitude BEEM current, I_C, (b) by propagating through the LUMO states of the molecules (at higher energy) with a larger I_C magnitude, in generic BEEM spectrum. (c) A schematic of BEEM experimental setup.

within classical free-electron models and are commonly used by the BEEM community. Kaiser and Bell [56, 61]. first derived an analytical expression for the $I_C(eU_{gap})$ spectra for simple metal/semiconductors contact and for electron energy close to the Schottky barrier Φ_{SB} considering a sequential three steps model:

i the electron emission from tip to metal surface by tunnelling,

ii hot-electron transport through the metal layer: inelastic scatterings result in an exponential decay of the BEEM current,

iii electron transmission at the metal/semiconductor interface considered as abrupt: Both electron energy and electron wave vector component parallel to the interface (transverse momentum) are conserved, and a quantum transmission coefficient at the interface is considered.

In this simple model, both STM tip and metal base layer are considered as free-electron metals, and the bottom of the semiconductor conduction band is also modelled using a parabolic dispersion with the considered semiconductor effective mass, allowing a simple analytical calculation of the BEEM spectra. Kaiser and Bell (KB) first considered a constant transmission coefficient at the metal/semiconductor interface, resulting in a simple quadratic power law of the BEEM current close to the threshold:

$$\frac{I_C(U_{gap})}{I_T(U_{gap})} \propto {\Phi_{SB}}^2 \tag{2.14}$$

Ludeke and Prietsch (LP) refined this first KB model by introducing the energy and wave-vector dependence of the interface transmission coefficient, leading to a modified power-law [62, 63]:

$$\frac{I_C(U_{gap})}{I_T(U_{gap})} \propto (eU_{gap} - \Phi_{SB})^{5/2} \tag{2.15}$$

For a detailed development of the KB and LP model calculations, the reader can refer to the excellent review by M. Prietsch [57] or to the PhD manuscripts of Sophie Guézo or Alexandra Junay [65, 53]. The LP model, despite its simplicity, is adapted to fit the experimental BEEM spectra close

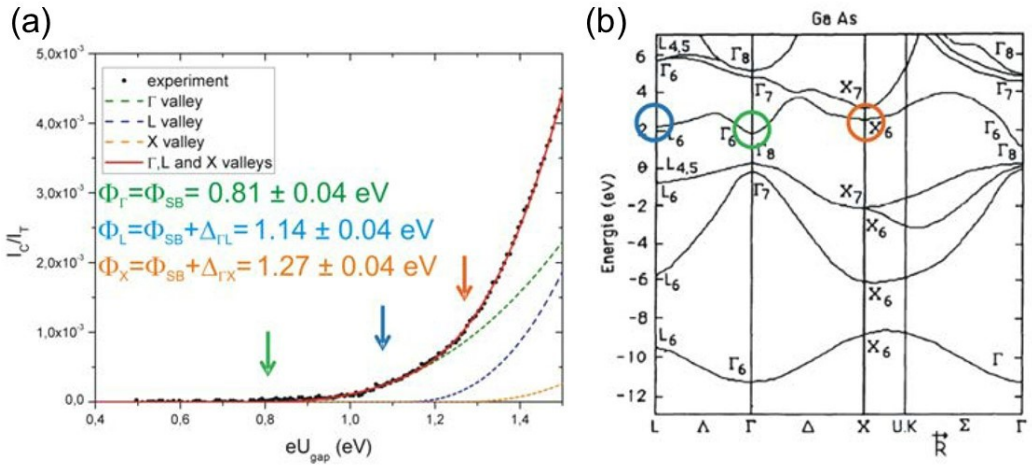

Figure 2.9: (a) Adjustment by the LP model, spectrum obtained on a junction $Au(5nm)/GaAs(001)$ (average of 6400 curves for a surface of $100 \times 100nm^2$ and (b) band structure of GaAs, figures taken from [53, 64].

to the threshold and allows a quantitative determination of the local Schottky barrier. An example of a quantitative data fit of a BEEM spectra on a simple Au/GaAs(001) Schottky contact is presented in figure 2.9.a. An excellent agreement between LP model and experimental data is obtained at low energy (typically between Φ_{SB} and $\Phi_{SB} + 0.3eV$. The Schottky barrier height deduced from the fit is $0.81eV$, in excellent agreement with literature, and corresponds to hot-electron injection in the lowest energy point of GaAs conduction band, i.e. the Γ-valley (see GaAs band structure figure 2.9.b. At higher energy, an inflection point on the experimental spectra is observed, the measured BEEM current exceeding the low-energy LP fit. This is due to the fact that with increasing energy, hot electrons can also be injected in the L-valley of GaAs conduction band, opening a new transport channel and leading to the observed BEEM current increase [66]. This can be taken into account in the LP fit by considering a second component to the BEEM current, with a second threshold corresponding to the energy position of the minimum of the L-valley of GaAs conduction band. A third component should finally also be considered associated to the opening of a new density of empty states in GaAs corresponding to the last and highest energy valley of GaAs conduction band, i.e. the X-valley. Finally, a complete fit of the BEEM spectra can be obtained over an extended energy range considering

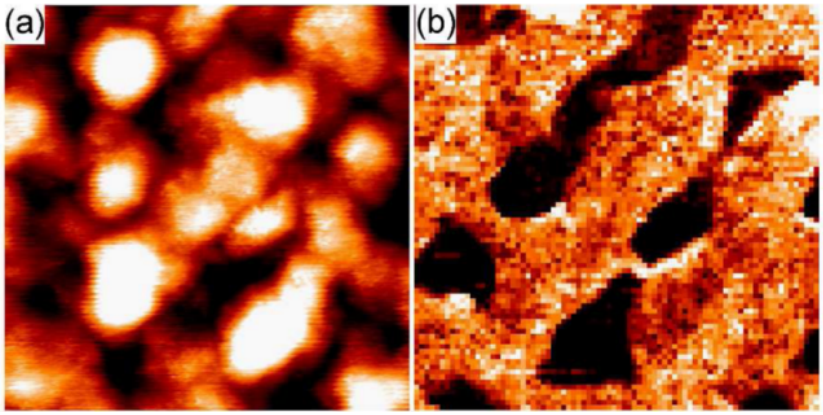

Figure 2.10: $50 \times 50\ nm^2$ STM images of gold overlayer surfaces on SAM, Au/C16MT/GaAs(001)((a) 5 nm thick gold deposited at room temperature, with peak-to-peak roughness of 1.1nm. (b) Simultaneously recorded BEEM images at $U_{gap} = 1.80V$ and $I_T = 5nA$ (color scale: 0 to 0.16 nA), figures are taken from [53].

all the transport channels in the 3 valleys of GaAs conduction band:

$$\frac{I_C}{I_T} = a_1(eU_{gap} - \phi_1)^{5/2} + a_2(eU_{gap} - \phi_2)^{5/2} + a_3(eU_{gap} - \phi_3)^{5/2} \qquad (2.16)$$

Remarkably, the energy values of the three thresholds deduced from the experimental data LP fit match perfectly the theoretical energy positions of the L and X valleys of GaAs, validating the LP data fit methodology. This multi-component LP fit can be generalized to other systems, each of the introduced components corresponding to a transport channel of the system opening at a specific energy Φ_i and with a spectral weight a_i corresponding to the magnitude of the BEEM current for each channel.

2.2.2 Example of a BEEM study on a hybrid metal/SAM system

Our group has previously investigated by STM/BEEM the formation and properties of $Au(5nm)/SAM/GaAs(001)$ metal top contacts, here with an hexadecanethiol (C16MT) SAM. As an illustration, Figure 2.10.a, presents a $50 \times 50nm^2$ STM image of the surface morphology of a 5nm thick Au metal

top contact deposited at room temperature on a dense hexadecanethiol self-assembled monolayer grafted on a GaAs(001) surface. A continuous polycrystalline metal film is obtained, with a typical granular morphology. The Au 3D islands have typical lateral extensions around 10nm and lead to a peak-to-peak roughness of 1.1nm. The simultaneously recorded BEEM current image at tunnelling bias of 1.8V and for a tunnelling current of 5nA is presented in figure 2.10.b. Strong contrasts are observed on this BEEM image with well-defined regions of high current transmission (bright regions) surrounding extended regions with a low current transmission (dark regions).

The morphology of the dark and bright regions on the BEEM image are not correlated to the surface topography. These strong BEEM contrasts are thus not related to local thickness variations of the gold layer. Figure 2.11 presents the local spectroscopy curves recorded respectively in the bright and dark regions of the previous BEEM image. Several individual spectra were averaged to reduce the signal to noise ratio. These BEEM spectra were compared to reference data measured on a simple $Au(5nm)/GaAs(001)$ sample. The BEEM spectra measured in the bright regions of the $Au(5nm)/C16MT/GaAs(001)$ is perfectly matching the reference $Au(5nm)/GaAs(001)$ spectra. The high transmission regions are thus attributed to local regions of the $Au(5nm)/C16MT/GaAs(001)$ sample where the metal has completely diffused through the SAM, creating a direct $Au/GaAs$ Schottky contacts, also called a pinhole. On the other hand, the BEEM spectra measured in the dark regions present a threshold value close to the one of the bright regions, but with an additional strong attenuation of the signal attributed to transport trough a molecular patch at the interface. More information is obtained by using a LP fit in both bright and dark regions as shown in figure 2.12.

The fit of the BEEM spectra in the bright regions are identical to the one obtained in the reference $Au/GaAs$ sample, with a first threshold at 0.83eV corresponding the energy position of GaAs conduction band Γ-valley for a direct $Au/GaAs$ Schottky contact, and a second threshold 0.34eV higher in energy is associated to the position of the L-valley for this system. This further confirms the presence of extended regions with strong metal penetration through the SAM in this system. In the dark regions, a similar first threshold value is observed, with an associated spectral weight a_1^{dark} about ten time smaller than the spectral weight a_1^{bright} in the bright region. This strong additional attenuation is attributed to a first transport channel by tunnelling trough the SAM barrier into the Γ-valley states of GaAs at low energy (Figure 2.8.a). This idea is supported by the calculated expected

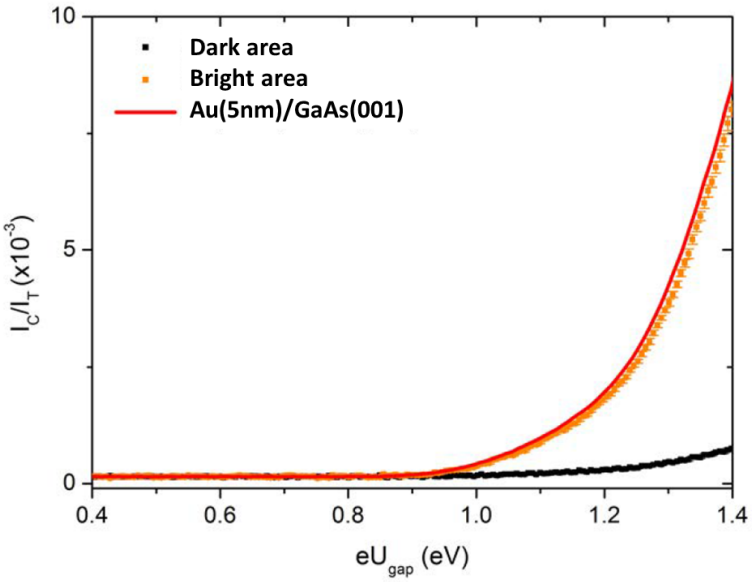

Figure 2.11: BEEM spectra of Au(5nm)/C16MT/GaAs(001) system, average of 14 (21) curves recorded in bright areas (dark). Solid line: average of 400 curves obtained on an Au(5nm)/GaAs(001) junction, figure taken from [67].

tunnel attenuation through the SAM, using typical organic thickness and effective mass values for the SAM [55]. At higher energy, a second threshold is observed to open 0.40eV higher in energy than the Γ-valley of GaAs. This second threshold, higher in energy than the *L*-valley of GaAs, is this time attributed to a transport channel through the LUMO states of the molecules (Figure 2.8.b). The corresponding heterostructure band diagram is presented in figure 2.12. It should be noted that no electron tunnelling through the SAM barrier into the *L*-valley of GaAs is possible. Indeed, electron tunnelling through a planar tunnel barrier selects electrons with wave vector close to the interface normal, while the *L*-valley states of GaAs correspond in GaAs band structure to electronic states with a large transverse momentum. From these initial observations on metal/SAM contacts, we can underline the interest of BEEM to study the interface homogeneity of these hybrid systems. BEEM allows first to image pinholes formed during metal deposition on the SAM. The local band diagram can also be determined in the areas where the molecular barrier was preserved and specifically the energy position of the LUMO states of the SAM as well as energy position of the semiconduc-

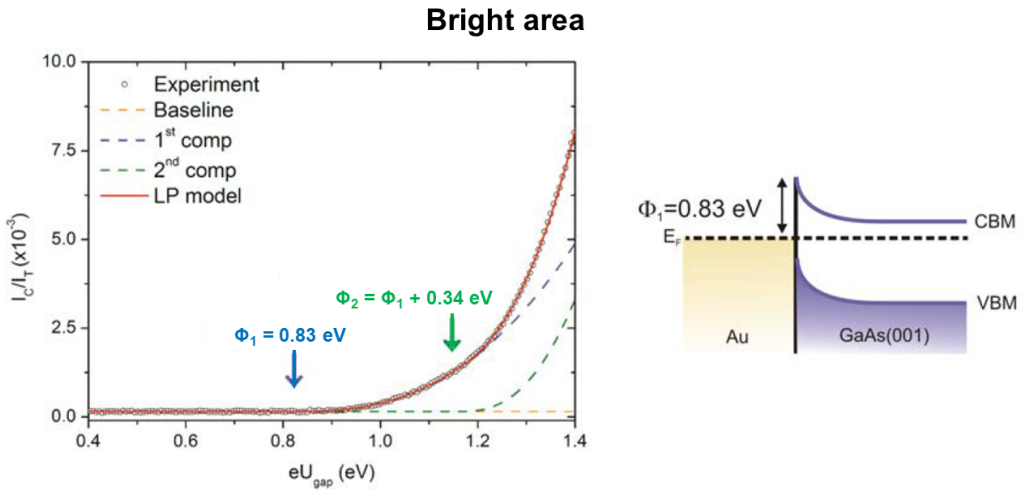

(a)

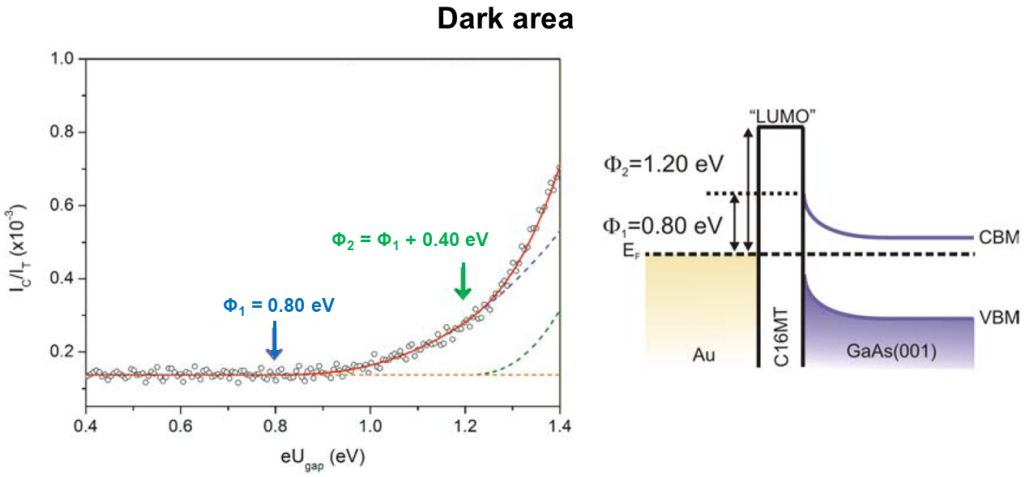

(b)

Figure 2.12: Adjustments by the LP model of the obtained curves from the (a) bright and (b) dark zones of an Au(5nm)/C16MT/GaAs(001) sample and diagrams of the associated band alignments, figure taken from [67].

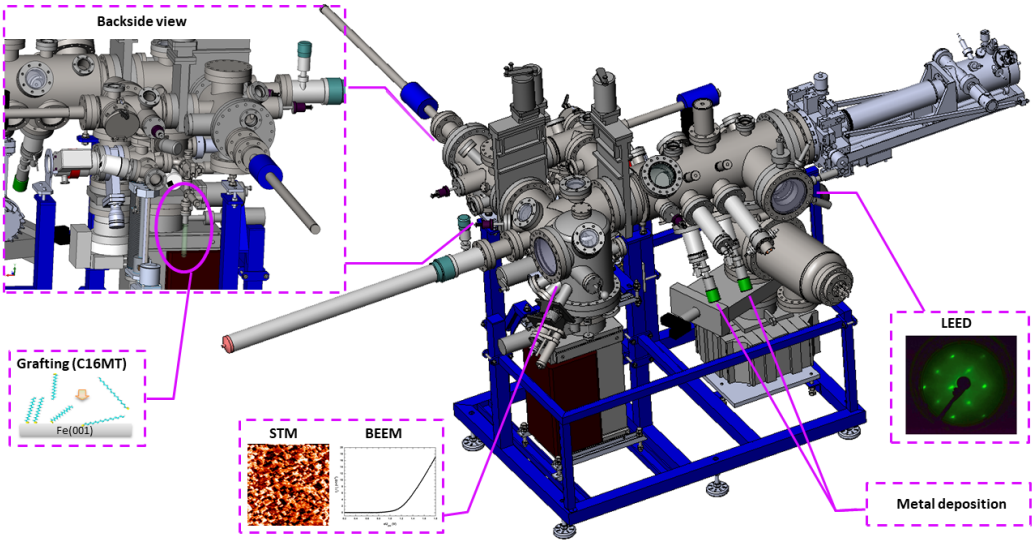

Figure 2.13: BEEM/STM setup employed to prepare and characterize *in situ* specimen.

tor conduction band minimum at the SAM/GaAs interface. This study was further generalized to investigate the influence of metal thickness, the use of dithiolated molecules in the SAM, and metal deposition by a soft landing method (or buffer layer assisted growth, see chapter 3.3) on the formation of pinholes [55, 54].

2.2.3 STM/BEEM experimental setup

This setup benefits from an UHV multi-chamber, including a preparation and a grafting chamber that allow the entire production process of samples to be performed *in situ*, displayed in Figure 2.13. The preparation chamber allows MBE metal deposition of Co, Fe and Au, currently. Moreover, a Low Energy Electron Diffractometer (LEED) assists to characterize the surface crystalline structure of a sample. The grafting chamber is connected to a flask as a molecules container with a micro leak-valve, allowing to control the grafting conditions. The STM/BEEM setup is based on an Omicron STM setup that has been adjusted to perform BEEM measurements. In STM mode, the sample holder is electrically grounded and the STM tip is

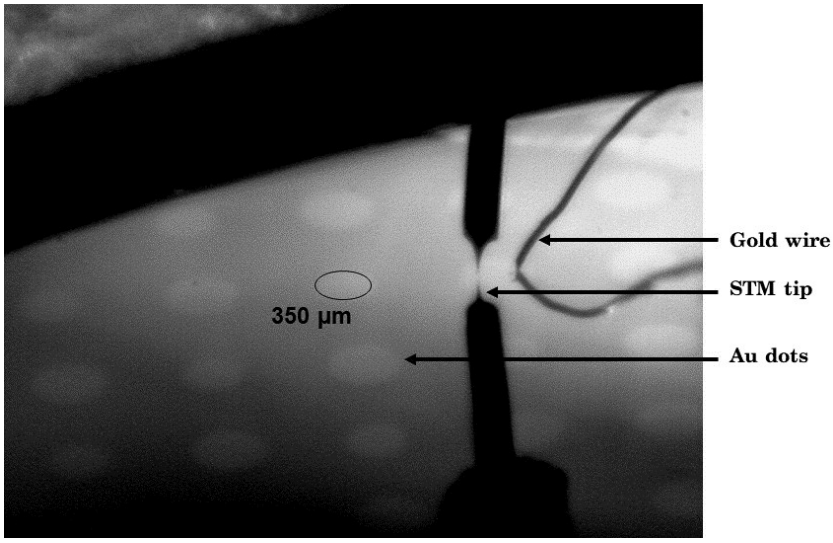

Figure 2.14: View from the camera: the gold wire is placed on a gold dot, to ground the sample of the selected junction and the STM tip is in tunnel contact with the surface of this dot, Figure taken from [67].

biased. Whereas to access the BEEM mode, the sample holder is electrically floating by disconnecting grounding of the sample holder. Instead, the surface of an in situ patterned junction is grounded by an external gold wire inside the STM head, shown in Figure 2.14. The sample holder is connected to the BEEM current measurement circuit while the tunneling current is drained by the gold wire and measured in an independent electronic circuit. STM/BEEM measurements are performed at room temperature and under ultra-high vacuum conditions, with the base pressure of several 10^{-11} mbar. The experimental challenges of heterostructures BEEM study will be carried out in the following section.

2.2.4 Sample preparation

Local BEEM measurement, carried out at room temperature, is delicate. Three sources of noise will impact the BEEM signal:

- The measurements being carried out at ambient temperature, a current of thermo-excited electrons continuously crosses the junction, contributing to a leak current.

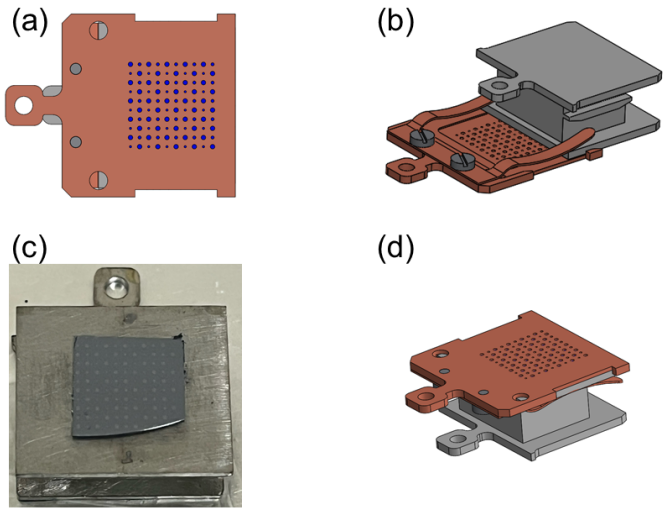

Figure 2.15: 3D design of (a) prepared shadow mask for BEEM measurements $1 \times 1cm^2$ with 3 sizes of holes $250\mu m$, $350\mu m$ and $500\mu m$, (b) and (d) present placing the mask on the sample holder, and (c) a prepared sample with metallic Au dots.

- There is also a source of noise related to the low voltage (few hundred μV)) present on the BEEM current measurement pre-amplifier which creates a slight polarization of the junction. Therefore a weak diffusive current enters the semiconductor substrate, even at low injection energy, contributing to the current background.

- Finally, a last source of noise is the presence of a photo-excited current.

To overcome these sources of noise, the measurements are carried out in the dark, thus eliminating the photo-excited current. To limit the amplitude of the current leakage, the resistance of the junction must be increased [68], which can be achieved by decreasing the area of the junction. For this purpose, the metal top contact of the junction is patterned *in situ* by using a transferable CuBe shadow mask during MBE metal deposition (Figure 2.15). This mask contains 3 hole diameters of $250\mu m$, $350\mu m$ and $500\mu m$ for different junctions. For plots of $500\mu m$ in diameter, we obtain a typical junction resistance of the order of $10^8\Omega$, which gives a leakage current of the order of a few pico-Amperes, corresponding to the continuous background present on

the BEEM spectra for energies lower than the barrier height of the studied system.

Conclusion

XPS-UPS and STM-BEEM setups available in our laboratory have been introduced as well as the essential used models for this work. These two techniques provide us with a complementary set of tools to effectively control each step of a magnetic molecular tunnel junction fabrication in micro- and macro-scale. This well-controlled sample production allows reproducible specimen preparation process, which is crucial for studying a model system.

3

Bottom Electrode Growth and Grafting

Introduction

The main objective of this chapter is to confirm a high quality grafted FM electrode. To pursue this objective, we focus on the fabrication process of several grafted ferromagnetic bottom electrodes studied by XPS study, and for the most promising system, complemented by LEED, RHEED, STM and UPS. This bottom-electrode investigation is finalized by a conclusive study of grafting quality on their surfaces. The band structure of SAM/FM system is also illustrated to have a better understanding of our system.

I will present the study of several FM bottom electrodes such as Cobalt, Permalloy and Iron, using surface spectroscopies. I will then describe the used SAMs, its grafting process and eventually XPS study of grafted SAMs on all noted FM electrodes. In the following, I will illustrate an analytical model to examine the grafting quality (SAMs coverage rate), leading to a well-controlled grafted electrode. Finally, I will display a deeper investigation on the most dense grafted system.

3.1 Bottom Electrode

Several potential bottom electrodes have been studied such as Co, Permalloy ($Ni_{80}Fe_{20}$) and Fe. Ferromagnetic deposition is performed in the preparation chamber employing MBE, presented in section 2.1.4. In order to thoroughly control the specimen fabrication steps (i.e. FM surface quality and grafting density), *in situ* XPS is exploited. We specifically use XPS measurements to determine the ratio between the molecule density of the SAM and the surface atomic density of the substrate, defining the bottom FM electrode grafting ratio. We thus investigate the crystal structure at the each FM surface which determines the surface atomic density of the termination layer.

3.1.1 Poly-crystalline Cobalt

A 10 nm thick poly-crystalline Co thin film is deposited on commercially available Si wafers (with native SiO_2 oxide) by using a pocket e-beam evaporator. A pure cobalt rod is evaporated by using electron bombardment. This deposition occurs at the pressure of 5×10^{-9}mbar at room temperature. Co deposition rate is controlled by a quartz crystal microbalance at the rate of 1.77 Å/min. A reproducible quality electrode is confirmed by XPS study as well as growth rate by a quartz crystal microbalance.

The Co film after the preparation has been analysed by XPS using Mg anode X-ray source, Co-2p core level is presented in Figure 3.1. For metallic Co layer, the Co-2p3/2 peak is reported at binding energy of 778.1eV [69]. The measured XPS spectra of Co-2p shown in 3.1, confirms the 2p3/2 peak to be at 777.8eV. Moreover, the 2p1/2 core level is observed at 15.0eV from 2p3/2, which is in excellent agreement with reported Co metallic layer. A negligible O-1s signal also confirms an oxide-free Co surface.

As it was explained, the surface atomic density of Co is required for illustration of a reference model for SAM coverage rate. Due to the ambiguous surface structure of poly-crystalline Co, we decided to consider the surface to be the most packed plane. The stable structure of cobalt is hexagonal closed-packed (hcp) [70], and the close-packed planes are the (0001) basal plane. In this plane for Co film, the Nearest and Next Nearest Neighbours are located at $NN = 2.52\mathring{A}$ and $NNN = 4.36\mathring{A}$, shown in Figure 3.2. The distance between two planes is $c/2 = 4.11\mathring{A}$. This surface structure has a

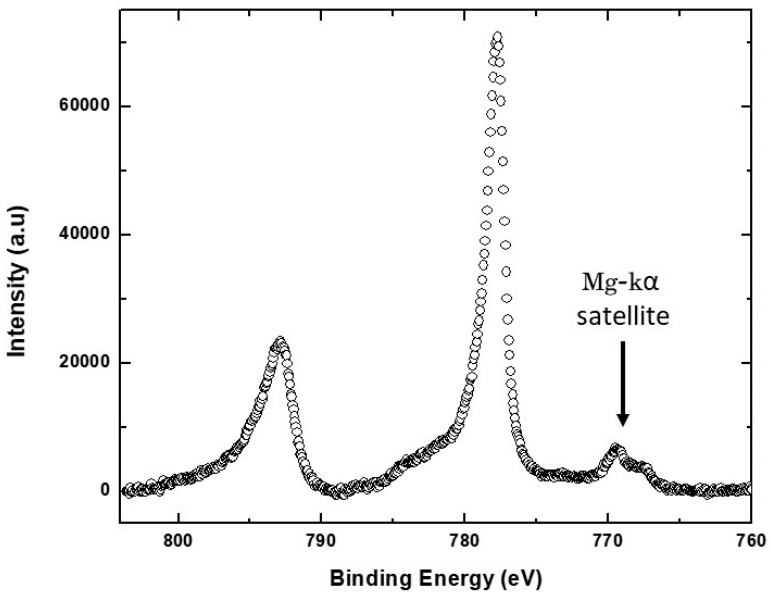

Figure 3.1: XPS measurement, Co-2p core level measured by Mg-kα X-ray source,Co-2p3/2 is located at 778.8eV.

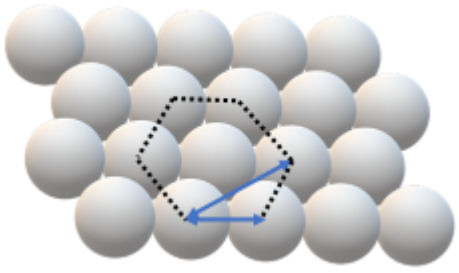

Figure 3.2: hcp-Co structure (0001), the Nearest and Next Nearest Neighbours are shown and located at $NN = 2.52\mathring{A}$ and $NNN = 4.36\mathring{A}$.

surface density of 0.18 $atom/\mathring{A}^2$ at Co surface.

3.1.2 Permalloy

Permalloy electrode, an alloy of 81% Ni and 19% Fe, can be simply deposited by congruent evaporation of bulk permalloy [71]. Pure (99.99%) Permalloy (Py :$Ni_{81}Fe_{19}$) has been commercially purchased to be used in an effusion cell. This 40nm thickness Py source was evaporated on MgO(001) substrate at pressure of 1×10^{-9}mbar, with the growth rate of 1.35 Å/min, and annealed at $300°C$ for 1 hour. XPS examines several aspects of this electrode such as surface contamination and the surface composition of the deposited NiFe alloy. To address those aspects, the XPS measurements takes place at normal and 45 degree detection direction defined by the analyser axis. At normal incidence, the Ni-2p and Fe-2p has been measured are shown in 3.3. The Fe-2p3/2 peak is located at 706.8eV refers to a metallic film Fe [69], confirming a deposited Fe metallic layer. It should be noted that the presence of oxidized iron at the surface would be conveniently detected by XPS due to the large chemical shift (few eV in binding energy) observed in iron oxide [72]. Additionally, no signal from O-1s core level can be detected confirming a clean Py surface. The integrated area of Fe-2p1/2 and Ni-2p1/2 intensities are representative of the Ni and Fe presence at the first few planes of the film. The electron mean free path of photoelectrons in Ni and Fe at the binding energy of 2p core levels defines the experiment surface sensitivity to 4 or 5 planes. The ratio between these two signals has been calculated, considering their cross sections $\left(\frac{I_{Ni}/\sigma_{Ni}}{I_{Fe}/\sigma_{Fe}}\right)^{2p_{1/2}} = 6.58$. This signal ratio of Ni-2p to Fe-2p demonstrates a formation of $Ni_{87}Fe_{13}$ layer. This measurement verifies a coherent alloy composition with the source of evaporation, $Ni_{81}Fe_{19}$. The small difference in compositions for Py is explained by XPS measurements at 45 degree. As the detection angle increases, the number of probed sample planes reduces. In another word, XPS measurements performed at 45 degree are more surface sensitive than at 0 degree. A larger Ni-2p signal compared to Fe-2p signal at 45 degree indicates the presence of a Ni access at the surface. To conclude an average $Ni_{87}Fe13$ surface stoichiometry has been determined with a tendency towards moderate Ni segregation at surface.

From a structural point of view, permalloy has been shown to grow as (001)-oriented single crystal films on MgO(001) at room temperature [73, 74].

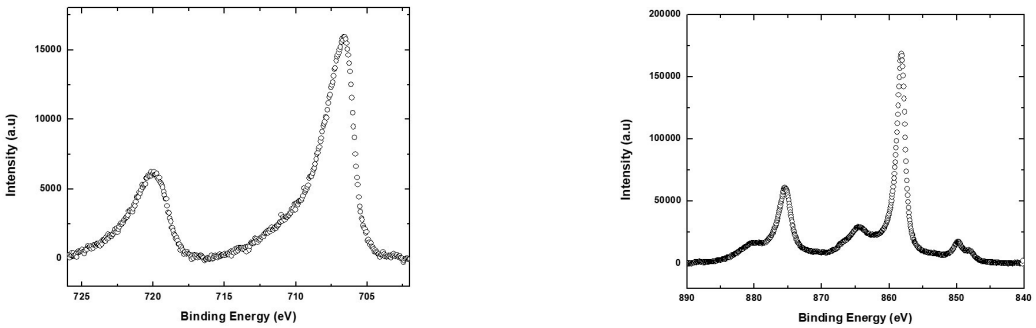

(a) Fe2p (b) Ni-2p

Figure 3.3: XPS spectra of Permalloy electrode measured with Mg-kα source(MgO(001)/NiFe), (a) Fe-2p1/2 and Fe-2p3/2 located at 719.9eV and 706.8eV, respectively. This location for Fe-2p core levels are reported for a metallic Iron layer, (b) Ni-2p.

Py has been observed to form an fcc structure, and films thicker than about 20–30 nm show a full structural relaxation[73]. The lattice parameter and the distance between two planes, in this case, is reported $a^(Ni_{80}Fe_{20}) = 3.55\mathring{A}$ and $a/2 = 1.78\mathring{A}$. The second nearest neighbor at the surface is at the distance $NNN = 5.0214\mathring{A}$, as it is shown in Figure 3.4. The surface density for Py is calculated to be 0.16 $atom/\mathring{A}^2$.

3.1.3 Iron

3.1.3.1 Mono-crystalline Fe

The iron film growth has been observed to be epitaxial bcc-Fe(001) on MgO(001) [75, 76]. In our study, mechanically polished MgO(001) substrates, commercially available, were used. The MgO(001) substrate is mounted on a Molybdenum holder with water-based silver paste (PELCO high performance Silver paste), tolerating high and low temperature [77, 78]. This silver paste containing silver flakes (20µm) in an inorganic silicate aqueous solution has good thermal and electrical conductivity. It contains no hydrocarbons, making it suitable for demanding specimen preparation in ultra high vacuum applications. The ultraviolet (UV)/ozone surface cleaning method was proven effective in removing the C contamination of the surface. The substrate also is annealed at 180°C for 2 hours before introducing to UHV to

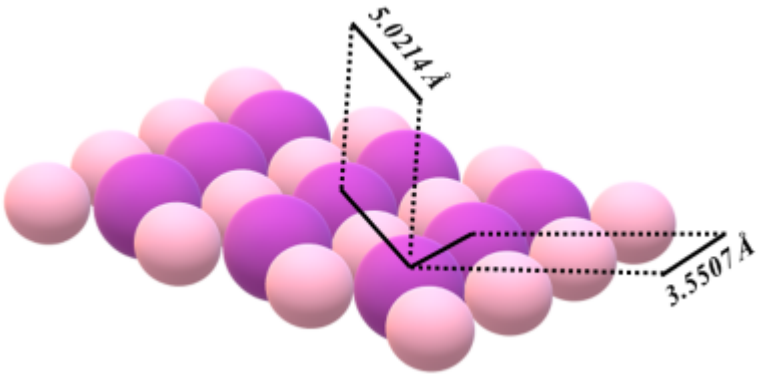

Figure 3.4: Permalloy structure (001), lattice parameter, and nearest next neighbor distance.

dry and degas the silver paste. The last step of MgO surface cleaning takes place under UHV, by annealing up to around 560°C for 1 hour. XPS study has shown 5 times reduction of Carbon contamination after UHV annealing. A 30nm thick Iron film is grown on the cleaned MgO(001) substrate at room temperature, with the growth rate of 5.85 Å/min at pressure of 10^{-8} mbar. The roughness of the Fe surface has been reported to affect the quality of SAMs formation. Hence, the sample has been annealed for 1 hour at 560°C to smooth the surface. The XPS measurement on Fe(001)/MgO(001) has confirmed a non-oxidised metallic Fe layer. Reflection high-energy electron diffraction (RHEED) has been employed to control the Fe film formation after growth and annealing. The RHEED patterns verify an epitaxial Fe film grown on MgO(001). Figure 3.5b shows the RHEED patterns of the substrate and the subsequently grown layer. Considering distinct spots and streaks for Fe layer, also at the exact location as the substrate patterns confirm the single-crystal Iron growth in the MgO(001) orientation. Moreover, square reciprocal lattice unit cell has been observed with Low Energy Electron Diffraction (LEED), presented in Figure 3.5c, which confirms a cubic lattice structure. The epitaxial orientation determined with RHEED/LEED is Fe(001)//MgO(001) and Fe[100]//MgO[110] [75].

As explained in section 3.1.2, the energy position of Fe-2p3/2 peak in binding energy allows to discriminate a metallic Fe layer from an oxide layer. The XPS study of the Fe/MgO(001) layer concludes to the deposition of an oxygen-free surface with some C traces (not shown).

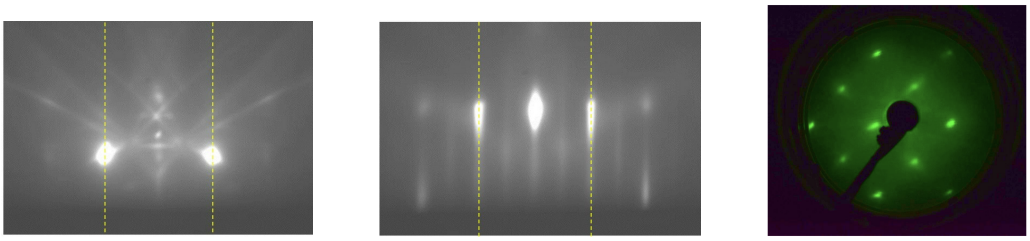

(a) MgO(001), RHEED (b) Fe(001), RHEED (c) Fe(001), LEED

Figure 3.5: Fe(001) electrode, (a) MgO(001) substrate RHEED pattern, after annealing at 560°C for 1 hour (detection beam parallel to $[110]_{MgO}$), (b) Fe(001)/MgO(001) RHEED pattern, 30nm Fe annealed at 560°C for 1 hour (detection beam parallel to $[100]_{Fe}$). (c) Fe(001)/MgO(001) LEED pattern.

As a substrate for growing mono-crystalline Fe electrode, GaAs(001) has also been used in this work. Epitaxial bcc-Fe(001) MBE-prepared on GaAs(2×4) is achieved[79, 80]. GaAs(001) layer with controlled doping layer is prepared in our group by MBE. A 3 μm cap layer of amorphous As protects the GaAs surface during the transfer at atmospheric pressure from the MBE enclosure to the Fe deposition/XPS enclosures. The As-cap decapsulation of the substrate is done thermally up to a temperature of 465°C in order to obtain an arsenic-rich GaAs(001) surface with a As(2×4) type surface reconstruction [68, 79]. A 30nm Iron film has been grown at room temperature on the GaAs(001) As-rich surface, with the same conditions as on MgO(001). XPS studies on Fe(001)/GaAs(001), has shown a negligible C contamination on the Fe surface. Therefore, this surface is more satisfactory for SAMs formation. Although, Fe/GaAs annealing was observed to make a mixture of two layers due to the interfacial reaction, also reported by our team previously [81]. Therefore, since the deposited Fe layer on GaAs cannot be annealed, the surface roughness is expected to be larger than in case of Fe(001)/MgO(001).

Fe(001) film grows in bcc structure on both MgO(001) and GaAs(001) substrate. Considering $a_{Fe} = 2.867$ Å[76], the Next Nearest Neighbours at the surface are $NNN = 4.054\mathring{A}$ and $NNNN = 5.734\mathring{A}$. The distance between two planes in this structure is $a\frac{\sqrt{2}}{2} = 2.03\mathring{A}$. The surface density for mono-crystalline Fe(001) layer is $0.122\ atom/\mathring{A}^2$.

3.1.3.2 Poly-crystalline Fe

A poly-crystalline Fe film was considered to be studied, due to the long time consumption of MgO substrate preparation process (two days). Fe deposition on Si substrate with native SiO_2 oxide layer forms a poly-crystalline film [82], Si preparation is not required. The first-deposited Fe atoms react with the surface (Si), displacing Si atoms from their positions. The result is an amorphous layer with compositions close to those of FeSi. On top of this reacted layer, crystallites of Fe with inter-diffused Si grow. Upon further Fe deposition, the crystallite composition evolves to pure Fe. This film of 10nm is deposited with the growth rate of 3.17 Å/min, at the pressure of 1×10^{-8}mbar.
As it was explained for poly-crystalline Co, the surface structure is imprecise. Therefore, we consider the same surface structure as mono-crystalline Fe to have a perspective for grafting rate.

Ferromagnetic electrodes deposition have been well controlled by XPS and thus the heterostructure fabrication can be carried on, starting with the SAM grafting process.

3.2 Grafting

Self-assembled monolayers are grafted on the studied FM electrodes. A dense grafted monolayer is desired to lower the probability of the top electrode penetration, at the ungrafted zones due to low SAM density. To define the grafting quality, XPS study of grafted surfaces is proposed to calculate the SAM coverage rate for each FM bottom electrode. The following is devoted to a full investigation on SAM grafting on FM electrodes.

3.2.1 Self-assembled monolayers

Self-assembled monolayers (SAMs) are molecular layers that assemble on a surface by adsorption. The intrinsic inter-molecular forces tend to drive the molecules into an ordered packing. SAMs are composed by a head, a body and an anchoring group that can be independently tuned thus allowing an easy engineering of the barrier[83], shown in Figure 3.6a. Their formation is mediated by a specific functional group (anchor group) that has a strong

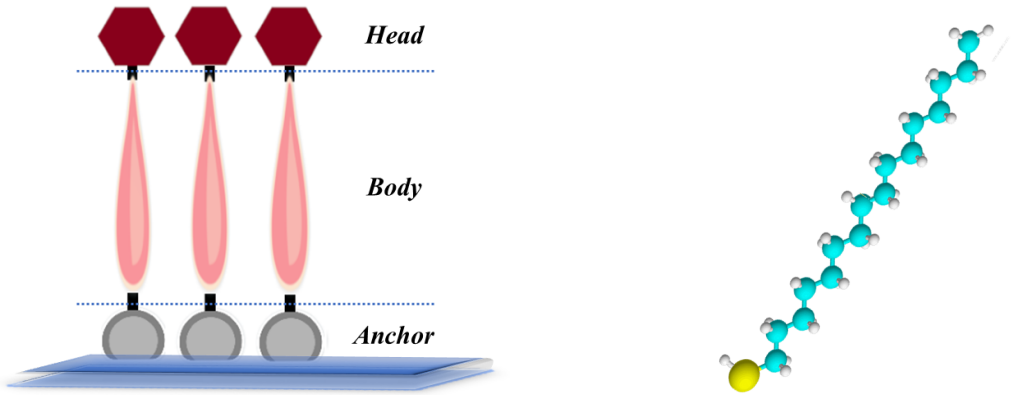

(a) (b)

Figure 3.6: SAMs, (a) Schematic of a Self-Assembled Monolayer structure. Molecules are formed by a head, a body and an anchoring group that can be independently changed, (b) Saturated Alkane chain with thiol anchoring group, Hexadecanethiol (HDT), $CH_3(CH_2)_{15}SH$, PubChem website.

affinity for a particular surface. Several different SAMs have been developed for a range of different substrate materials including FM metals such as Fe, Co, Ni etc [84, 85, 86, 87, 88, 89]. The structure of the molecular body plays the key role on transport properties. Its choice allows to modify the barrier potential, from fine tuning of its properties (height, width, etc) to the addition of new functionalities. For instance, a saturated alkane chain is insulating and electrically equivalent to a rectangular potential barrier. On the contrary, the insertion of an aromatic ring in the chain introduces discrete levels in the barrier that modify its height and can also lead to a resonant configuration [90].

Hexadecanethiol

In this study, we have chosen Hexadecanethiol SAMs as our separator layer. Hexadecanethiol, noted as C16MT, is a saturated chain of 16 carbons and the anchoring group of Sulfur, with the chemical formula of $CH_3(CH_2)_{15}SH$, shown in Figure 3.6b. This molecule has been reported with the length and the lateral size of 22.8$\mathring{A}$ and 4.25$\mathring{A}$, respectively [91]. The lateral size of this molecule defines the smallest separation distance between two grafted molecules. C16MT is in liquid phase at room temperature due to the low

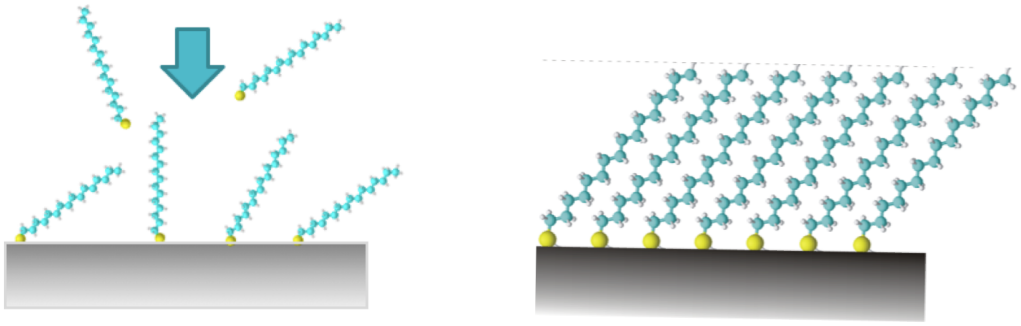

(a) (b)

Figure 3.7: Schematic of vapor phase Self-Assembled Monolayer grafting structure. Hexadecanethiol grafting on a substrate, (a) Vapour phase grafting process, (b) Self-Assembled Monolayer.

melting point of around 20°C. Highly pure C16MT, $> 95\%$, is commercially available, noted as C16MT, at Sigma-Aldrich company.

3.2.2 Vapor phase grafting

By choosing the vapor phase method for grafting, we have taken advantage of our UHV multi-chamber setup to have a fully *in situ*-prepared sample. This multi-chamber allows the SAM formation on fresh FM-deposited surfaces without any surface contaminations. In this method, the substrate is exposed to the molecular vapor pressure of 5×10^{-6}mbar for 1 hour, and a packed self-assembled monolayer forms on the substrate, shown in Figure 3.7b. The organic molecules are contained in a flask connected to the grafting chamber under UHV via a micro-leakage valve allowing the control of time and molecular pressure during grafting. This flask is heated up to $40°C$ during the grafting, using heating tape. Before the molecular grafting step on FM substrate, the purification of liquids containing the molecules is carried out in order to eliminate the most volatile constituents. For this, cooling-pumping and heating-pumping cycles are performed.

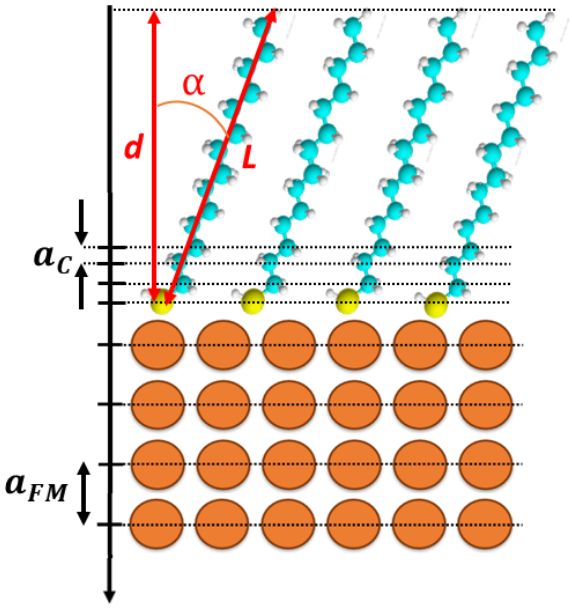

Figure 3.8: Schematic sketch of SAM grafted on a ferromagnet layer, a_{FM} and a_C are associated to the atomic distance between two layers of FM and C, respectively, d and L to the thickness and length of the molecules with a tilting angle of α.

3.2.3 XPS study of the SAM grafting

3.2.3.1 Methodology

XPS was used to investigate the SAM properties after grafting the different ferromagnetic surfaces presented previously. The surface grafting rate (GR) for each system is defined by calculating the ratio between the molecule surface density and the atomic surface density at the FM surface. Figure 3.8 presents all the experimental parameters defining the experiment geometry. We consider a layer model for the stack, with successively the ferromagnet atomic layers (interlayer spacing a_{FM}) and the hexadecanethiol SAM, supposed to be homogeneous. All molecules with chain length L are parallel with a tilt angle α with respect to sample normal. The C planes parallel to surface in the SAM are separated by a_C, the SAM thickness is thus $d = 16 \times a_C = L\ cos(\alpha)$.

In order to experimentally determine the grafting ratio, we will determine:

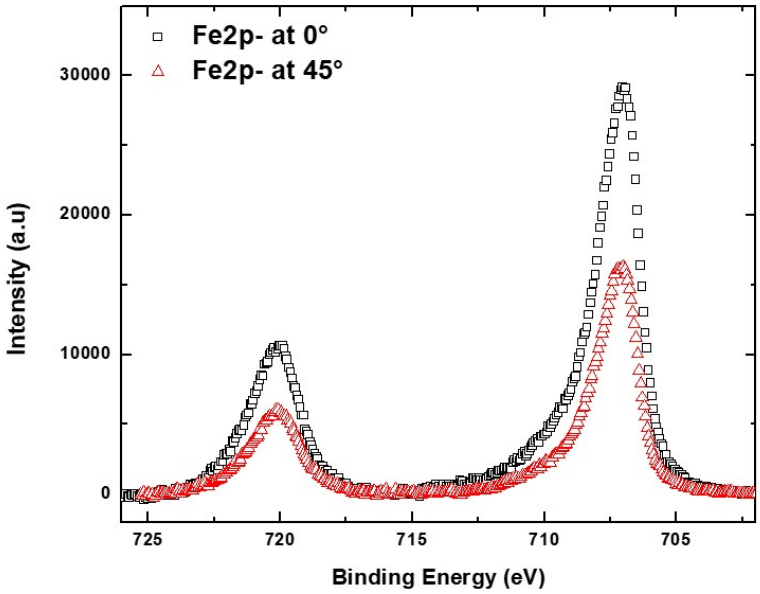

Figure 3.9: XPS spectrum, C16MT/Fe(001)/MgO/(001), Fe-2p peak is shown after grafting at $\theta = 0°$ and $\theta = 45°$, $Al - k\alpha$ source.

- the elementary photoemission intensity emitted by one monoatomic layer of the ferromagnet for the 2p1/2 core level, written I_{FM}^{ML},
- the elementary photoemission intensity emitted by one monoatomic C layer of the SAM for the C1s core level, written I_{C1s}^{ML}.

Since I_{FM}^{ML} (respectively I_{C1s}^{ML}) is proportional to the FM 2p1/2 (respectively C1s) photoionization cross section and to the FM atomic surface density (respectively molecule surface density), the grafting rate can be first obtained as follow:

$$GR_1 = \frac{I_{C1s}^{ML}/\sigma_{C1s}}{I_{FM}^{ML}/\sigma_{FM}} \tag{3.1}$$

Experimentally, we first measured the photoemission FM 2p1/2 core level intensity after grafting and for an analysis direction of $\theta = 0°$ and $\theta = 45°$ (see figure 3.9). In these two geometries, the FM photoemission signal is attenuated by the effective SAM thickness $d/cos(\theta)$ of the organic layer. We can thus calculate the ratio of the FM 2p1/2 core level photoemission intensities for both geometries as follow:

$$\frac{I_{FM}^{45^\circ}}{I_{FM}^{0^\circ}} = \frac{e^{-\frac{d}{\lambda_{SAM}^{2p1/2}\,cos(45)}}}{e^{-\frac{d}{\lambda_{SAM}^{2p1/2}}}} = e^{-\frac{d(\sqrt{2}-1)}{\lambda_{SAM}^{2p1/2}}} \tag{3.2}$$

where $\lambda_{SAM}^{2p1/2}$ is the electron mean free path in the organic layer at the kinetic energy of the FM-2p1/2 core level [92].

This allows us to determine an experimental value for the SAM thickness d as:

$$d = -\frac{\lambda_{SAM}^{2p1/2}}{\sqrt{2}-1}\; ln\left(\frac{I_{FM}^{45^\circ}}{I_{FM}^{0^\circ}}\right) \tag{3.3}$$

The corresponding experimental value for $a_C = d/16$ can trivially be deduced. Adapting equation (2.12) for a semi-infinite FM layer buried underneath the SAM, we also have:

$$I_{FM}^{0^\circ} = I_{FM}^{ML}\; \frac{e^{-\frac{d}{\lambda_{SAM}^{2p1/2}}}}{1-e^{-\frac{a_{FM}}{\lambda_{FM}^{2p1/2}}}} \tag{3.4}$$

where $\lambda_{FM}^{2p1/2}$ is the electron mean free path in the FM layer at the kinetic energy of the FM-2p1/2 core level [92].

leading to the experimental I_{FM}^{ML} value:

$$I_{FM}^{ML} = \frac{1-e^{-\frac{a_{FM}}{\lambda_{FM}^{2p1/2}}}}{e^{-\frac{d}{\lambda_{SAM}^{2p1/2}}}}\; I_{FM}^{0^\circ} \tag{3.5}$$

Let us now focus on the measured XPS carbon signal associated to the SAM (figure 3.10). The total C1s photoemission intensity can be calculated as the sum of the photoemission signals emitted by each of the individual carbon layers in the SAM, damped after propagation through the above lying carbon layers. For example, the XPS signal from the first C layer attached to the sulphur anchor on the FM surface is attenuated by the above 15 other

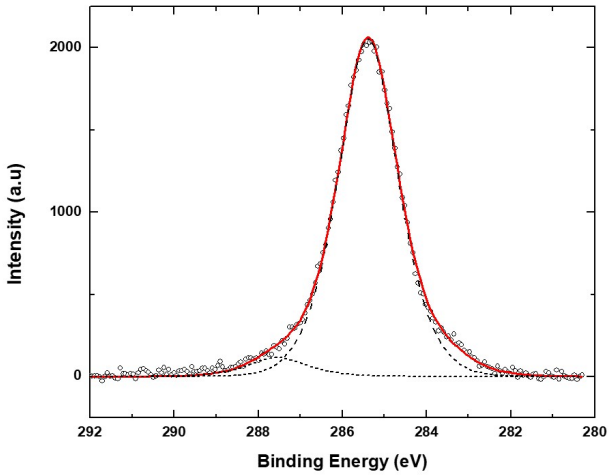

Figure 3.10: XPS spectrum, C16MT/Fe(001)/MgO/(001), C-1s peak is shown after grafting, measured with $Al-k\alpha$ source. The major peak located at $E_B = 285.3eV$ is assigned to C-C and C-H bonds, whereas a negligible signal is observed for C=O, 3eV shifted in binding energy.

C layers. This self-attenuation process leads to a total C1s photoemission intensity for a measurement normal to sample surface calculated as:

$$I_{C1s}^{0^\circ} = I_{C1s}^{ML}\left(1 + e^{-\frac{a_{FM}}{\lambda_{SAM}^{C1s}}} + e^{-\frac{2a_{FM}}{\lambda_{SAM}^{C1s}}} + ... + e^{-\frac{15a_{FM}}{\lambda_{SAM}^{C1s}}}\right)$$

$$= I_{C1s}^{ML}\ \frac{1 - e^{-\frac{16a_C}{\lambda_{SAM}^{C1s}}}}{1 - e^{-\frac{a_C}{\lambda_{SAM}^{C1s}}}} \tag{3.6}$$

where λ_{SAM}^{C1s} is the electron mean free path in the SAM at the kinetic energy of the C-1s core level [92]. The resulting numerical value for I_{C1s}^{ML} is easily calculated from equation 3.6 and allows to determine the grafting rate for all the investigated systems. The corresponding values are presented in the first line of table 3.1.

A similar XPS data analysis can be obtained while working with the intensity of the sulphur 2p core level. The S-2p photoemission signal is due

to the S atoms located at the SAM/FM interface, and thus corresponds to the elementary XPS signal of one atomic layer of S, I_S^{ML}, damped by the SAM thickness:

$$I_S^{0^\circ} = I_S^{ML} \; e^{-\frac{d}{\lambda_{SAM}^{S2p}}} \tag{3.7}$$

where λ_{SAM}^{S2p} is the electron mean free path in the SAM at the kinetic energy of the S-2p core level [92].

A second experimental evaluation of the grafting rate, GR_2, can be deduced by calculating the ratio between I_{S2p}^{ML} and I_{FM}^{ML} after normalization with the respective photoionization cross sections:

$$GR_2 = \frac{I_{S2p}^{ML}/\sigma_{S2p}}{I_{FM}^{ML}/\sigma_{FM}} \tag{3.8}$$

Furthermore, we now have also access to an experimental value of the ratio $R_{C/S}$ between the surface densities of C chains and the surface density of thiol anchors at the FM surface as follow:

$$R_{C/S} = \frac{I_{C1s}^{ML}/\sigma_{C1s}}{I_{S2p}^{ML}/\sigma_{S2p}} \tag{3.9}$$

The calculated GR_2 and $R_{C/S}$ values for all investigated FM electrodes is presented in the second and third lines of table 3.1 respectively.

3.2.3.2 Discussion

The experimental grafting ratios have to be compared to theoretical values that can be expected for an hexadecanethiol dense monolayer on each of the ferromagnetic electrodes. We first considered an ideal SAM geometry with the maximal surface density allowed by steric hindrance considerations, i.e. an hexagonal closed-packed structure with a lattice parameter of $4.25\mathring{A}$. The corresponding molecular surface density of $0.064 molecule/\mathring{A}^2$, independent of the FM electrode surface structure, was used to calculate an upper limit GR_3 of the surface grafting ratio presented in table 3.1.

In a more realistic second approach, we considered that the molecular assembly is determined not only by steric hindrance effects, but also by the lattice geometry of the FM surface, each molecule being attached to a surface atom. For instance, after grafting a first molecule on a surface site,

Grafting Rate					
		Co Electrode	Permalloy Electrode	Mono-Fe Electrode	Poly-Fe Electrode
		Co-2p	Py-2p	Fe-2p	Fe-2p
Measured	GR_1	0.11	0.40	0.32	0.13
	GR_2	0.33	0.19	0.29	0.59
	$R_{C/S}$	0.32	2.16	1.10	0.22
Theory	GR_3	0.36	0.4	0.53	0.53
	GR_4	0.33	0.25	0.25	0.25

Table 3.1: Grafting Table, the Coverage rate for C16MT on Co, permalloy, and Fe electrodes(Mono-Crystalline and Poly-Crystalline Iron electrodes are noted as Mono-Fe and Poly-Fe electrodes, respectively).

the next one can be anchored on the second nearest neighbour surface atom only if the second nearest neighbour distance is larger than the molecular diameter. The resulting SAM has the same symmetry than the FM surface and a lattice parameter equal to the second nearest neighbour distance. This is for example the case for the hexagonal Co surface, where 1 surface site out of 3 can be grafted, resulting in molecular surface density of $0.06 molecule/\mathring{A}^2$. For the permalloy and iron surfaces on the other hand, the second nearest neighbour distance is smaller than the molecular diameter, leading to SAMs with a lattice parameter equal to the third nearest neighbour distance, and thus to SAMs with lower density, 1 surface site out of 4 being grafted only. The grafting ratios GR_4 calculated with this assumption are also presented in table 3.1.

Before discussing the experimental values of grafting ratios determined by XPS on each system, let us focus on the $R_{C/S}$ ratio between the alkane chain and sulphur atoms densities on sample surface. This ratio should be equal to 1 for a model SAM, i.e. for an experimental grafting geometry similar to the one presented in figure 3.8. In that case, each molecule brings one S atom at the surface, which is located at the SAM/FM interface. The $R_{C/S}$

ratio can eventually be smaller than 1, if some molecules during the grafting process has been temporarily attached to the FM surface before being desorbed after breaking the C-S bond, leaving a lone S atom on the surface site. In this case, the calculated grafting ratio GR_2 deduced from the S-2p core level analysis will be overestimated, while the GR_1 experimental value should still be reliable. This is typically what is observed in the case of the polycrystalline Fe and Co electrodes, where GR_2 are significantly exceeding the GR_1 values, this tendency being amplified with increasing surface concentration of lone S atoms. On the other hand, a $R_{C/S}$ value larger than 1, as observed on the permalloy electrode, can be due to a sample geometry different from the chosen model one, as for example in the eventual case of the presence of excess surface molecules physisorbed on top of the chemisorbed SAM. Such configuration will this time affect the reliability of both experimental GR_1 and GR_2 values deduced from XPS data analysis, making a quantitative discussion of the grafting ratios quite elusive for the permalloy electrode. Nevertheless, from table 3.1 data analysis, one can identify the $Fe(001)/MgO(001)$ electrode as the most promising one. Indeed, for this electrode, the $R_{C/S}$ ratio is first close to unity, corresponding to a grafted layer of unaltered molecules. Second, the two experimental grafting rates GR_1 and GR_2 deduced respectively from the C1s and S2p core level analysis are remarkably consistent, with absolute values in-between GR_3 and GR_3 thus corresponding to a high density SAM with a geometry close to the ideal case depicted in figure 3.8.

After this point, we decided to pursue this work focusing mainly on the preparation of hybrid magnetic tunnel junctions integrating a bottom $Fe(001)/MgO(001)$ ferromagnetic electrode and an hexadecanethiol SAM as tunnel barrier, this system being identified as the most promising one. It should however be noted that other preliminary grafting studies have also been performed using other molecules including Tetradecanoic acid (Myristic acid, with a carboxylate anchor group), and 4,4' Biphenyldithiol on Fe(001). These results are not be presented in the manuscript for sake of conciseness.

3.3 Investigation of $C16MT/Fe(001)/MgO(001)$

Mono-crystalline Fe electrode has been studied as the bottom electrode in section 3.1.3.1. Other aspects of Hexadecanethiol SAM properties on Fe were examined using STM, XPS, LIXPS and UPS.

STM characterizations on an *in situ* grown 30nm thick Fe(001) electrode before and after grafting have been performed (see part 2.2.3 for experimental details). Figure **??** presents typical $400 \times 400nm^2$ STM images obtained before grafting on the Fe(001) surface. For the first sample (figure 3.11a), no *ex situ* cleaning of the MgO substrate was done, while for the second one (figure 3.11b), the initial MgO surface was cleaned from hydrocarbon adsorbates by using an ozone generator. This *ex situ* surface cleaning process has a major influence on the initial Fe(001) surface. Without ozone treatment, the Fe(001) surface presents atomic steps, mostly parallel to the Fe[110] crystal direction. Most of these steps are anchored on screw dislocations emerging at the surface. On the atomic terraces, a high density of nanometric inclusions is observed, appearing as depletions on the STM image. These defects are attributed to the presence of carbon inclusions at the Fe(001) surface, resulting from C segregation from the initial MgO surface during the post-growth film annealing process. We can also note that these C inclusions are regularly observed at the dislocation emerging point. After ozone cleaning, the C inclusions are completely removed from surface. The surface step density has also significantly decreased after annealing, which is probably due to the fact that C inclusion were acting as pinning centers for the motion of emerging dislocations. The resulting surface morphology is extremely flat, with a peak to peak roughness below 0.4nm over a $400 \times 400nm^2$ area. After the hexadecanethiol SAM grafting, no evolution of the surface morphology is observed at large scale by STM. At low scale figure 3.11c, the SAM presence is confirmed by STM with the observation of a new granular texture at the surface. It was not possible to observe any specific local molecular order in the SAM, which is consistent with the fact that no diffraction pattern could be observed by LEED on the grafted surface.

XPS measurements were used to check the thermal stability of the Hexadecanethiol SAM on Fe. After grafting, the SAM has been annealed sequentially for 20 minutes at a certain temperature, each annealing temperature has been reached at the same rate. After each annealing step, sample was cooled down and analyzed by XPS. The Fe-2p and C-1s signals have been recorded after every annealing step. The intensity of the 1s core level of C is normalized by the Fe-2p1/2 signal and plotted as a function of annealing temperature in Figure 3.12. A drastic drop of the normalized C-1s signal is observed at 90°C. This study illustrates the thermal stability of this

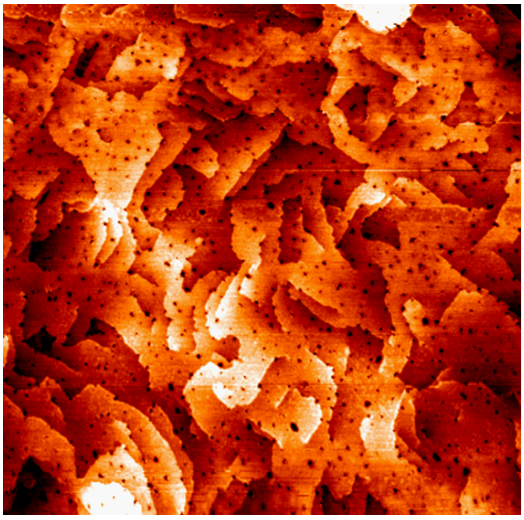

(a)

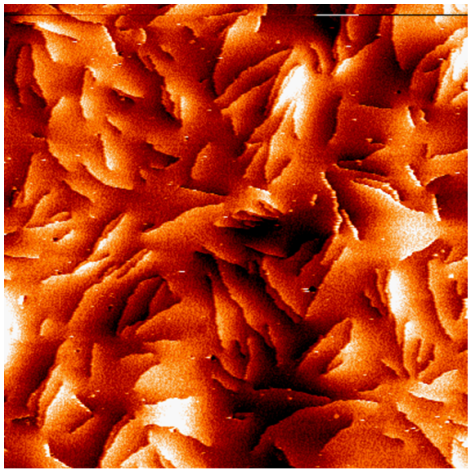

(b)

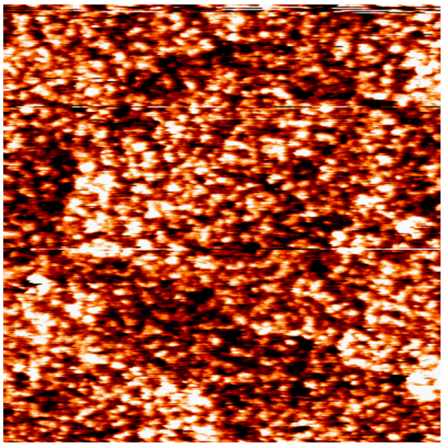

(c)

Figure 3.11: STM images, (a) $Fe(001)/MgO(001)$ no *ex situ* cleaning, , STM $400 \times 1 = 400nm^2$ image of Iron surface ($I_T = 0.36nA$, $U_{gap} = -0.218V$), color scale: $\Delta z = 0.5nm$, (b) $Fe(001)/MgO(001)$ after UV/ozone surface cleaning of MgO substrate, STM $400 \times 400nm^2$ image of Iron surface($I_T = 0.012nA$, $U_{gap} = 0.822V$), color scale: $\Delta z = 0.4nm$, edges of the image are aligned with Fe[100], (c) $C16MT/Fe(001)/MgO(001)$, $75 \times 75nm^2$ ($I_T = 15pA$, $U_{gap} = -1.9V$) surface image of C16MT grafted on Fe(001).

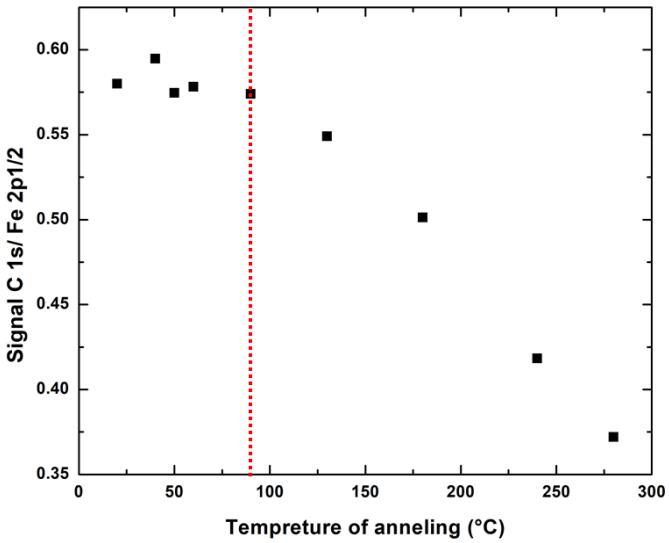

Figure 3.12: Evaluation of XPS signal of C core level, normalized to the substrate signal(Fe-2p1/2), by annealing grafted C16MT molecules on Fe(001)/MgO(001) substrate.

molecular layer on Iron electrode up to 90°C.

Moreover, the long term room temperature stability of the molecules has also been confirmed by XPS measurements after 3 and 7 days, without any detected variation of the C signal.

UPS measurements of grafted Hexadecanethiol SAM on Fe(001) was performed. The UPS spectra gives access to the system band diagram. A schematic UPS spectra of metal and metal/organic system have been displayed in Figure 3.13. In this figure, Φ_m and Φ_{SAM} are the work functions of metal and SAM, respectively. The width of the emitted electrons (W) from the onset of the secondary electrons up to the Fermi edge directly gives the work function:

$$\Phi = h\nu - W \tag{3.10}$$

where $h\nu$ is the energy of the incident UV light.

UPS spectra of deposited Fe layer after annealing up to 460°C is presented in Figure 3.14a. This spectra has been measured using $He\ I$ line ($h\nu = 21.21\ eV$ [93]). This UPS spectra with a cutoff at 17.19 eV corresponds to a

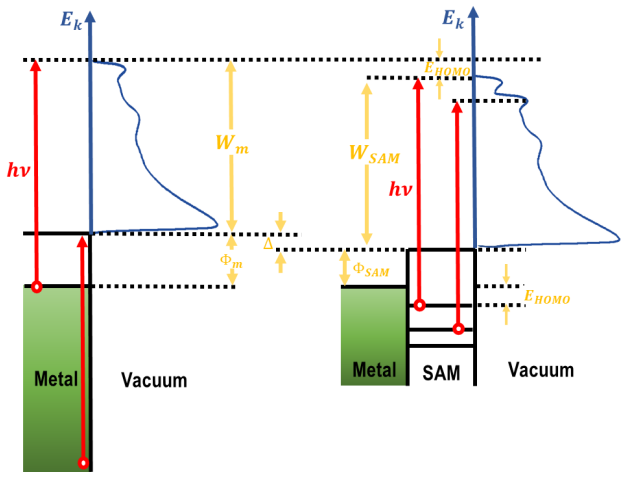

Figure 3.13: Energy relationships in UPS, left for metal system, and right for an organic layer deposited on the metal substrate. Δ:vacuum shift (presence of a dipole moment at the interface), E_{HOMO}: energy of the highest occupied molecular orbital

work function of the Fe substrate of 4.02 eV.

The UPS study has been completed by a set of measurements on a grafted Iron layer, presented in Figure 3.14b. This spectra presents visible changes in shape due to the molecular energy levels, in comparison to Fe spectra. The Iron Fermi level is still detectable in this spectra (at $E_K = 0$). To have access a broader energy range, a $He\ II$ line has been employed ($h\nu = 40.8\ eV$ [94]). The recorded spectra of Fe and C16MT/Fe using $He\ II$ line is presented in Figure 3.15. The Fe states close to the Fermi level have been dramatically attenuated due to the presence of molecular layer at the surface. In this spectra a small satellite peak at roughly $E_K = 7\ eV$ is observed, due to the presence of a satellite emission line in the UV source. In the spectra of C16MT/Fe, a typical shape for $E_K < E_{Fermi}$ is observed similar to what was observed by UPS on alkanethiol grafted on gold [95]. The first peak before E_{Fermi} determines the HOMO of the molecular layer, shown with an arrow in Figure 3.15b

The complementary Low Intensity X-ray Photoemission Spectroscopy (LIXPS) measurements on Fe and C16MT/Fe gives a perspective on dipole formation at the Fe surface. The dipole potential at a particular interface can be determined by comparing the work functions derived from LIXP-spectra

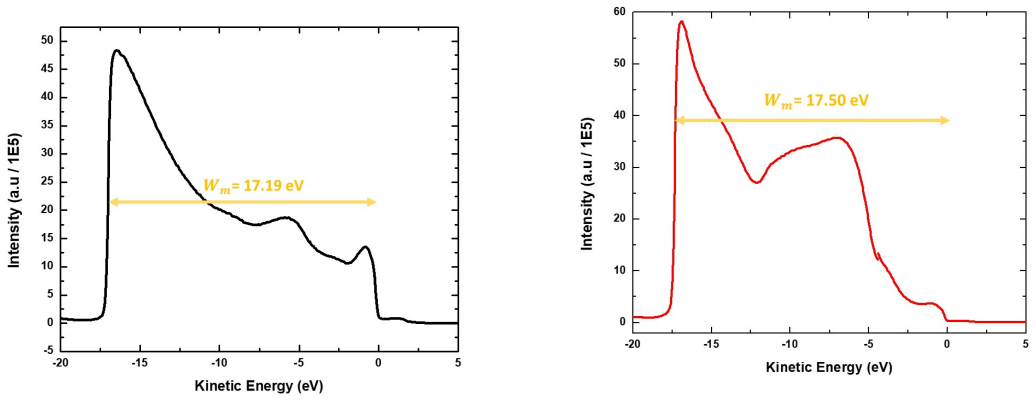

(a) (b)

Figure 3.14: UPS spectrum using $He\ I$ line, $h\nu = 21.21\ eV$, (a) Fe layer, $\Phi_{Fe} = 4.02\ eV$, (b) grafted Fe by C16MT $\Phi_{SAM} = 3.71\ eV$, leading to a dipole formation of $\Delta_{UPS} = \Phi_{Fe} - \Phi_{SAM} = 0.31\ eV$, by UPS.

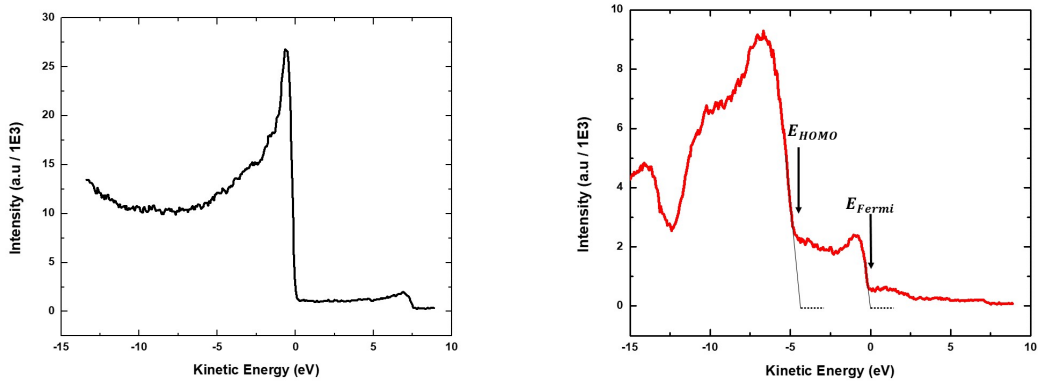

(a) (b)

Figure 3.15: UPS spectrum using $He\ II$ line, (a) Fe layer, (b) grafted Fe by C16MT.

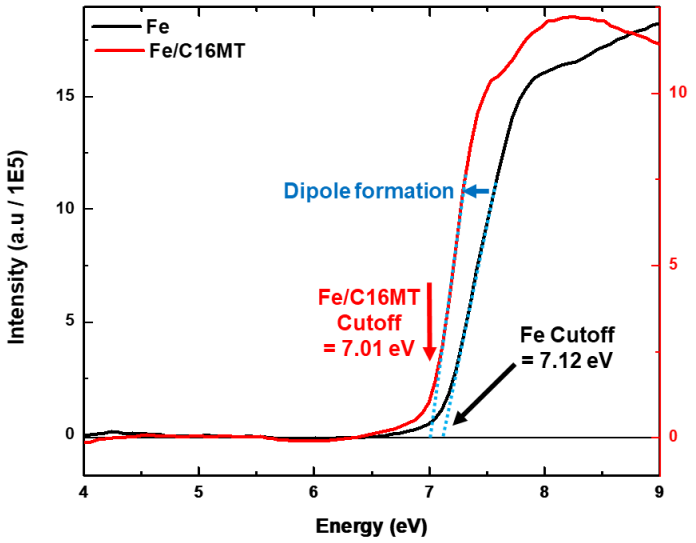

Figure 3.16: Low Intensity X-ray Photoemission Spectroscopy (LIXPS) using $Al - k\alpha$ source, LIXPS-cutoff of Fe (black line) and Fe/C16MT (red line), leading to a dipole formation of $\Delta_{LIXPS} = \Phi_{Fe} - \Phi_{SAM} = 0.10\ eV$, by LIXPS.

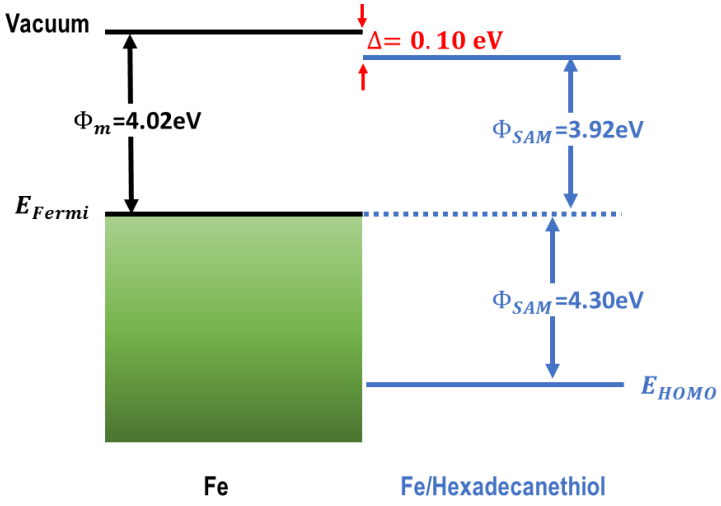

Figure 3.17: Band diagram extracted from UPS measurements, left for metal system, and right for an organic layer deposited on the metal substrate. $\Delta = 0.31eV$, and E_{HOMO} is located $4.31eV$ below the Fermi level.

on Fe before and after grafting SAMs. The LIXPS has been performed on Fe and again on grafted Fe using $Al - k\alpha$ source, displayed in Figure 3.16. These two spectra are shifted by the cutoff energies of $\Delta_{LIXPS} = 0.10\ eV$. This value confirms the dipole formation at the interface of metal/SAMs. UPS measurements of the grafted Fe results in work function of the grafted molecular layer on Fe at $\Phi_{SAM} = 3.71\ eV$, with onset of $W_{SAM} = 17.50\ eV$. A larger shift between the two work functions for metal and SAMs by UPS, $\Delta_{UPS} = 0.31\ eV$, is measured, which was expected due to the charging artifacts caused by the high photon flux used during the UPS measurement. The considering band deduced from our experimental data is presented in Figure 3.17.

Conclusion

The Fe(001)/MgO(001) is selected to as the bottom electrode at this step, and Py to be next studied. A smooth Fe surface has been observed by STM, only 100pm peak-to-peak roughness over 30nm of Fe deposition. Moreover, LEED has shown a mono-crystalline layer of Iron on MgO(001). These two qualities for the deposited Iron layer play a major role in the quality of the self-assembled monolayer in this substrate. Hexadecanethiol SAMs has been grafted as dense as expected, although grafting a carboxylate anchor has not been yet completely understood. The thermal stability of the hexadecanethiol up to 90°C has been established in this study. Moreover, the band diagram of the system has been explored using UPS and LIXPS.

4

Top electrode

Introduction

The following chapter is dedicated to address the challenges of top ferromagnetic electrode deposition on organic self-assembled molecular monolayers without formation of filaments (shorts) through the tunnel barrier. In this regard, we intend to employ a buffer layer assisted growth (BLAG) technique to prevent the top-electrode penetration through the SAM over a relatively large junction (several square micrometers). BEEM and XPS are used to validate this method, and to further study the SAM/top-electrode interface.

In this chapter, I will first introduce the BLAG technique, and several XPS studies specifically designed to investigate all aspects of this method at a macroscopic scale. Then, I will present the nano scale BEEM study of our heterojunctions which will allow to investigate the lateral homogeneity of the organic barrier, the formation of eventual pinholes, as well as the energy position of the LUMO states in the SAM.

4.1 Buffer Layer Assisted Growth (BLAG) technique

Buffer layer assisted growth (BLAG) is used to provide top-electrode soft landing and thus to prevent the FM penetration through the grafted SAM [54]. This method consists of four main steps:

First step: The grafted bottom-electrode is cooled down to 20K under UHV.

Second step: The cooled grafted substrate, then, is exposed to a noble gas (Xe or Kr) partial pressure. Low temperature causes a formation of frozen noble gas layer on top of SAM. The SAM is thus precovered with an overlayer of a condensed noble gas which then serves as a soft landing layer, displayed in Figure 4.1. The thicker the layer, the more one can expect the metal film to be formed without contact with the SAM. To define and control the noble gas layer thickness currently the unit of Langmuir (noted L) is used. A Langmuir corresponds to an exposure under $10^{-6}\,Torr$ ($1\,Torr = 1.33\,mbar$) for one second. In theory, for a sticking coefficient of 1, an exposure to 1 L is enough to obtain a monolayer of atoms adsorbed on a surface.

Third step: The top-electrode is deposited on the sample(on-top of the noble gas layer, at low temperature) with direct metal evaporation under UHV. The formation of noble gas layer assists in quenching the kinetic energies of subsequent vapor deposited metal atoms. Therefore, it prevents direct chemical and physical interactions between the top-electrode atoms and the organic molecular monolayer thereby preventing penetration. Additionally, it helps reducing or eliminating chemical degradation in the case of reactive metals, and overall providing a highly uniform medium for nucleation and growth [96].

Final step: The last step is to warm up the sample up to room temperature to remove the noble gas. The sample is heated sufficiently to allow the buffer layer to sublime into the vacuum, leaving a top layer of immobile metal nanoclusters to make contact with the SAM without diffusion [97].

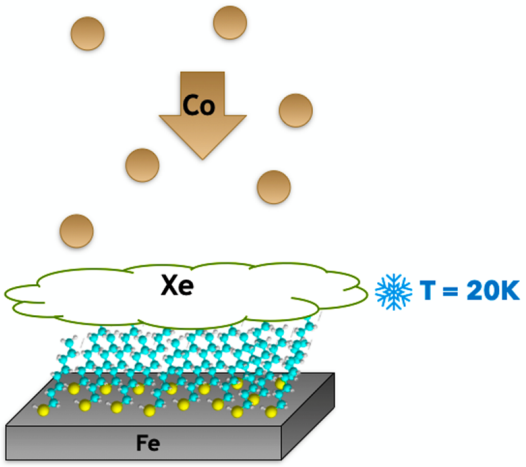

Figure 4.1: Schematic of top-electrode deposition employing BLAG technique.

Top-electrode deposition employing BLAG

Thanks to our multi-chamber UHV setup, a freshly grafted Iron film [C16MT/-Fe(001)/MgO(001)] is transferred to the preparation chamber for top-electrode deposition. The sample is mounted on a sample holder using Silver paste for thermal contact. This paste can tolerate low and high temperatures, which is required for BLAG method and annealing Fe surface, respectively. A close-cycled helium compressor cools down the sample from 293K to 20K at the rate of 4.5 degrees (K)/min. The sample holder is transferred onto a cryostat connected to the compressor for cooling down process. Then, Xe is deposited through a leak-valve for 15 minutes at a pressure of 1.3×10^{-6}mbar, with a base pressure of 1×10^{-10}mbar. The deposited amount (900 L) corresponds to a $100nm$ thick Xe ice layer. For the top-electrode a FM with a different switching field, in comparison to the bottom electrode (Fe), is chosen , Co in our case. Our preparation chamber is equipped with an MBE setup to deposit the Co layer. Co electrode is deposited by MBE at a pressure of 5×10^{-9}mbar with the rate of 1.77 Å/min. The SAM/Fe/MgO(001) specimen is placed on the cryostat facing Co-cell deposition. The samples prepared for STM/BEEM purposes are covered by a 4nm Au cap layer (growth rate of 3.4 Å/min) to protect Co-layer from oxidization during the transfer in the STM chamber. To remove the Xe layer, we warm up the sample to room

temperature at the rate of 0.5 degree(K)/hour, requiring 9 hours to go back to RT. During this Xe removal process, 3 peaks of high pressure are observed which can be an indicator of sublimating the Xe buffer layer into the vacuum. At 40K the pressure increase up to several 10^{-6}mbar, the pressure recovers within a few minutes to a few 10^{-8}mbar. The second rise in pressure is observed at around 60K, and a third boost arrives at 150K. These Xe removal pressure peaks reach higher pressure by increasing the deposited Xe thickness. However, they always have been observed to rise at around the same temperatures.

4.2 XPS study of BLAG-prepared specimen

An XPS study has been designed to confirm the validation of the BLAG technique. For this objective, a thin Co top-electrode is deposited on C16MT/Fe-(001)/MgO(001) employing BLAG method. This sample has been studied by XPS before and after Co-layer deposition. This thin Co layer (11$\mathring{A}$) allows detection of the core levels of C-1s and S-2p of the molecule as well as bottom electrode core-levels. Comparing the measurements before and after Co-layer provides information about the top-electrode formation.

Indeed, deposition of Co on a SAM/Fe bilayer results in a damping of the C, S and Fe core level photoemission intensity. This damping factor β_i is experimentally determined for each core level i (i=C, S, Fe) by dividing the considered core level intensity after Co deposition by its initial value before Co deposition :

$$I_i^{after\ Co} = I_i^{before\ Co} \quad \beta = I_i^{beforeCo} e^{-\frac{d_{Co}}{\lambda_{Co}^i}} \tag{4.1}$$

Where d_{Co} is the cobalt layer thickness and λ_{Co}^i is the electron mean free path in cobalt at the kinetic energy of core level i.

We experimentally determined the damping factors for the C-1s, S-2p and Fe-3p after Co deposition. Since these three core levels have kinetic energies in a relatively narrow energy window, the corresponding electron mean free paths in cobalt (extracted from NIST website [92]) are quite similar. Table 4.1 presents the 3 considered core level kinetic energies, EMFP in cobalt λ_{Co}^i, measured damping factors β_i and deduced Cobalt thickness calculated using equation 4.1.

	Kinetic Energy(eV)	Co-EMFP λ^i_{Co}(Å)	Damping Factor, β_i	Thickness d_{Co} (Å)
C-1s	966	14.2	0.49	10.3
S-2p	1088.2	15.6	0.58	8.4
Fe-3p	1197.6	16.8	0.54	10.5

Table 4.1: BLAG validation, damping factor caused by Co top-layer deposited on a grafted Iron film, and the Co thickness calculated from each core-levels, the core level kinetic energies are given for used Mg-kα source.

The calculated damping factors for the core-levels of C, S and Fe are in good agreement with each other. This result suggests that C-1s and S-2p, which are representative of SAM, are attenuated with the same factor as the Fe bottom electrode signal. This behaviour is typical of a sample with a deposited Cobalt film presenting an homogeneous thickness over sample surface. Alternatively, as will be shown in the following section, C-1s and S-2p signals are expected to show a lower attenuation than the Fe-3p signal in the case of Co penetration through the molecular layer.

4.3 XPS study of RT-prepared specimen

A complementary XPS study has been designed to investigate whether Co-layer penetrates the SAM, on a macroscopic scale during RT deposition. For this objective, we briefly present a complementary STM and XPS study of Co deposition on As-rich GaAs(001) at -10°C by K. Ludge et al. [98]. In this paper, Co deposition on GaAs(001) has shown a formation of a surface CoGa alloy. The XPS spectra of Ga-3d presents the appearance of a second component after Co deposition, with a chemical shift of 1eV. This component is a reacted component attributed to the formation of CoGa-like phase, not shown.

To check the metal penetration through SAM, we have designed a sequential analysis of a series of samples with increasing Co thicknesses (d) deposited on grafted GaAs(001) at RT (d = 0.8$\mathring{A}$, 1.6$\mathring{A}$, 3.2$\mathring{A}$, 6.4$\mathring{A}$ and 12.8$\mathring{A}$). The sample has been studied by XPS after each deposition step,

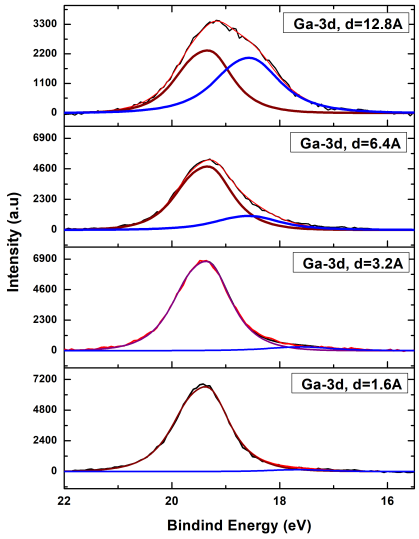

Figure 4.2: XPS study of Ga-3d evolution after Co deposition for thicknesses of d = 1.6, 3.2, 6.4 and 12.8Å(red and blue fitting curves are attributed to Ga-3d core level and GaCo component, respectively).

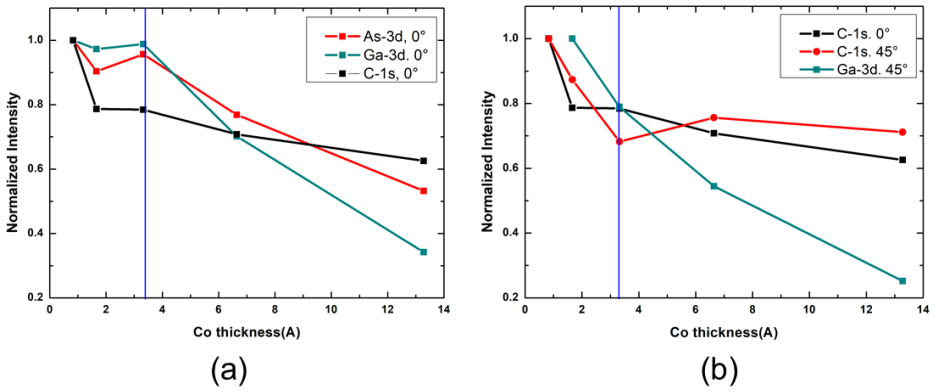

Figure 4.3: XPS study of different Co thicknesses on a grafted GaAs(001) substrate at RT(Mg-kα), all intensities have been normalized to their initial value at 0.8$\mathring{A}$ Co-thickness, (a) Ga-3d, As-3d and C-1s signal evolution with Co deposition at 0 degree, (b) C-1s evolution at 0 and 45 degree, Ga-3d evolution at 45° is presented as a reference of damping factor.

and core levels for Ga, As, C and Co have been recorded. Development of a second component for Ga-3d with a shift of 1eV is clearly visible by increasing the Co thickness, after d = 3.2$\mathring{A}$, shown in Figure 4.2. This second Ga-3p component appearance proves the interfacial Co and Ga reaction due to Co diffusion through the SAM at room temperature.

Additionally, the intensities of Ga-3d, As-3d, and C-1s after each Co deposition at 0 degree are presented in Figure 4.3. All intensities are normalized to their initial values after the first step of Co deposition (d=0.8$\mathring{A}$). The figure presents an almost constant value for all three core levels of Ga-3d As-3d and C-1s up to d=3.2$\mathring{A}$.

After 3.2$\mathring{A}$ deposited cobalt, the C-1s signal is only slowly decreasing, while the Ga-3d and As-3d intensities are further strongly damped by increasing cobalt deposition. This second regime, with a weaker attenuation of the SAM signal compared to the substrate signal is typical of the SAM disruption due to a strong diffusion of Co atoms during the room-temperature deposition process. This is further confirmed by reporting the evolution of the normalized C-1s signal compared to the substrate Ga-3d, but for a 45° detection angle, i.e. for a more surface sensitive experiment geometry. Again, the C layer is first significantly buried by the cobalt layer during the initial deposition stages. After 3.2$\mathring{A}$ of deposited cobalt, the detected signal for grazing detection angle increases, clearly proving the sudden incorporation of C in the bulk of the Co layer and close to the surface, with a larger C signal at 45° than 0°. The observed cobalt diffusion through the organic barrier at room temperature is thus accompanied by the outer diffusion of C towards surface. It should be noted that the magnitude of the effects evidenced by XPS points out that this cobalt diffusion process is an extended phenomenon, and occurs on a macroscopic scale.

XPS study of 12$\mathring{A}$ Co deposition on both C16MT/GaAs(001) and GaAs(001) using BLAG has shown that CoGa alloy formation at the interface is avoided, shown in Figure 4.4. The presence of Xe layer for Co deposition prevents chemical Co-Ga interaction, regardless of the presence of SAM. These observations confirm a better control of the interface offered by BLAG technique, however it can not be conclusive on Co diffusion through the molecular layer.

Beside the cobalt deposition using BLAG and at RT, a third preparation sample condition with Co deposition at 25K without Xe layer has also been studied. This top-electrode deposition at low temperature has shown similar

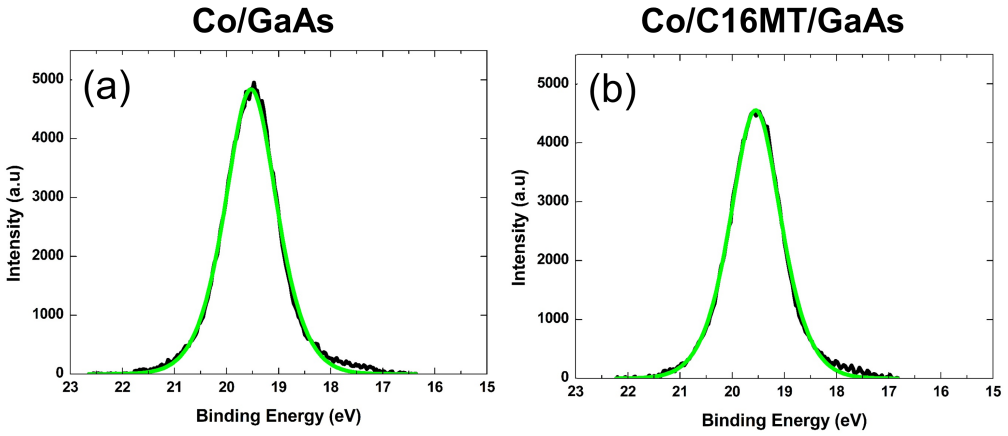

Figure 4.4: XPS study of Ga-3d evolution after Co deposition for thicknesses of 12Å, using BLAG method, (a) Co/GaAs(001) and (b) Co/C16MT/GaAs(001).

results to RT-sample concluding in the Co diffusion through the SAM, the results are not shown here.

Finally, to check the Xe layer influence on the grafted molecular layer, we have also studied a grafted FM (C16MT/Fe) before and after Xe deposition, without metal deposition, using XPS. Similar normalized C-1s to Fe-2p signals before Xe deposition and after Xe lead to the conclusion that established the monolayer remains intact during Xe deposition and removal, with the sensitivity of XPS:

$$\left(\frac{I_{C-1s}}{I_{Fe-2p}}\right)^{beforeXe} \simeq \left(\frac{I_{C-1s}}{I_{Fe-2p}}\right)^{afterXe}$$

In conclusion, XPS study of Co top-electrode deposition on a grafted substrate at RT and low temperature with and without employing BLAG technique has validated the BLAG technique for preventing metal penetration through SAM, in macroscopic scale. Moreover, the Xe deposition on SAM shows to have negligible effect on the grafted monolayer.

4.4 BEEM study

In this section both BLAG- and RT-prepared samples are investigated by BEEM to validate BLAG and study the SAM/top-electrode interface. In BEEM study as it was explained in chapter 1.3, injected electrons travel through the top-electrode, then the molecular layer, and eventually are collected at the back of the substrate. To study a full organic molecular MTJ system by BEEM several issues have to be considered. The BEEM current has to travel through a multi-layer junction, including an insulator molecular layer. Therefore, the thickness of each layer is required to be as thin as possible without affecting their properties. For the bottom electrode, a 1.2nm mono-crystalline Fe(001) layer at on GaAs(001) has been previously studied in our team. The Fe magnetization was observed to be in plane of the film with the strong uniaxial anisotropy along the Fe[110] axis [99]. For the Co top-electrode, an out of plane magnetization has been observed for a thin layer [100], we thus limit ourselves to 3nm thickness. As explained, the BEEM setup is not equipped for BLAG technique, therefore a gold cap layer is deposited on the top-electrode to avoid sample oxidization during air transfer between the XPS/BLAG and STM/BEEM chambers. A spin-valve sample $Au(4nm)/Co(3nm)/C16MT/Fe(1.2nm)/GaAs(500\mu m)$ has been prepared for local BEEM investigations of the hot-electron magneto-transport properties with variable electron energy. One major difficulty in these studies is the extremely low current signals measured on such MTJs with 4 layers and 4 interfaces, strongly reducing the electronic transmission. This first specimen has indeed demonstrated a very low hot-electron signal, at the detection limit of the setup. The future implementation of a liquid nitrogen cryostat on our STM head should open this instrumental limitation.

Meanwhile, a BEEM investigation of Co top-electrode on SAMs, without presence of Fe layer, was proposed. In this study, we intend to increase the hot-electron signal by reducing the layers and interfaces from 4 to 3. Grafting C16MT on GaAs substrate has been widely investigated by our team, showing a reliable grafting quality on arsenic-rich GaAs(001) surface with an As(2×4) type surface reconstruction [67, 53].

To investigate BLAG method validation on cobalt, samples of Co(3nm) deposited on a grafted GaAs(001), protected by a gold layer, have been prepared at RT and with BLAG method.

4.4.1 Room Temperature Specimens

A sample of $Au(4nm)/Co(3nm)/C16MT/GaAs(500\mu m)$ has been prepared at room temperature for STM/BEEM study. As a reference, a similar Schottky RT-sample without SAMs has been also investigated, $Au(4nm)/Co(3nm)-/GaAs-(500\mu m)$.

The STM images display the topography of the Au surface on $Co(3nm)/-GaAs(500\mu m)$ and $Co(3nm)/C16MT/GaAs(500\mu m)$ in Figure 4.5.a and 4.5.c, respectively. $60 \times 60nm^2$ STM image of the Schottky sample displays atomic resolution of Au(100) terraces. This observed topography indicates an epitaxial Au/Co layer growth on GaAs(001). Whereas the surface topography on $Au/Co/C16MT/GaAs(001)$ shows Au 3D islands with a typical lateral size of 5-10nm and a roughness of 1nm. These round shaped islands indicate a poly-crystalline growth of Au/Co on the grafted GaAs substrate. BEEM current images have been recorded simultaneously, presented in Figure 4.5.b and .d. The BEEM image of Schottky sample was taken at a tunnelling bias of $U_{gap} = 1.8V$ and for a tunnelling current of $I_T = 11nA$. The BEEM image for the sample with SAM has been measured at $U_{gap} = 1.75V$ with $I_T = 15.3nA$. On this BEEM image, some contrasts can be observed, with quite well-defined nanometric regions presenting a slightly higher/lower electron transmission. However, the magnitude of the observed contrasts is much smaller than what was observed previously while imaging pinholes in the $Au/C16MT/GaAs(001)$ system (figure 2.9).

Moreover, these contrasts are correlated with the surface topography, with a lower BEEM current observed in the 3D metallic islands and a higher BEEM current in-between. At this point, we thus rather attribute the observed contrasts to a variable attenuation of the hot electron beam due to local thickness variations in the granular metallic film. From our previous experience of BEEM investigations on metal/SAM/GaAs samples, the RT deposited $Au/Co/C16MT/GaAs(001)$ sample thus appears as surprisingly homogeneous. BEEM spectroscopy measurements will bring the necessary additional information to conclude on the interface properties of this sample.

In Figure 4.6, variations of the BEEM current is presented as a function of hot-electron injection energy eU_{gap} for both RT deposited sample, without (Figure 4.6.a) and with SAM (Figure 4.6.b). To improve the signal to noise ratio, the presented BEEM spectra correspond to an average of 400 individual spectra recorded on a grid covering a measurement area typically between

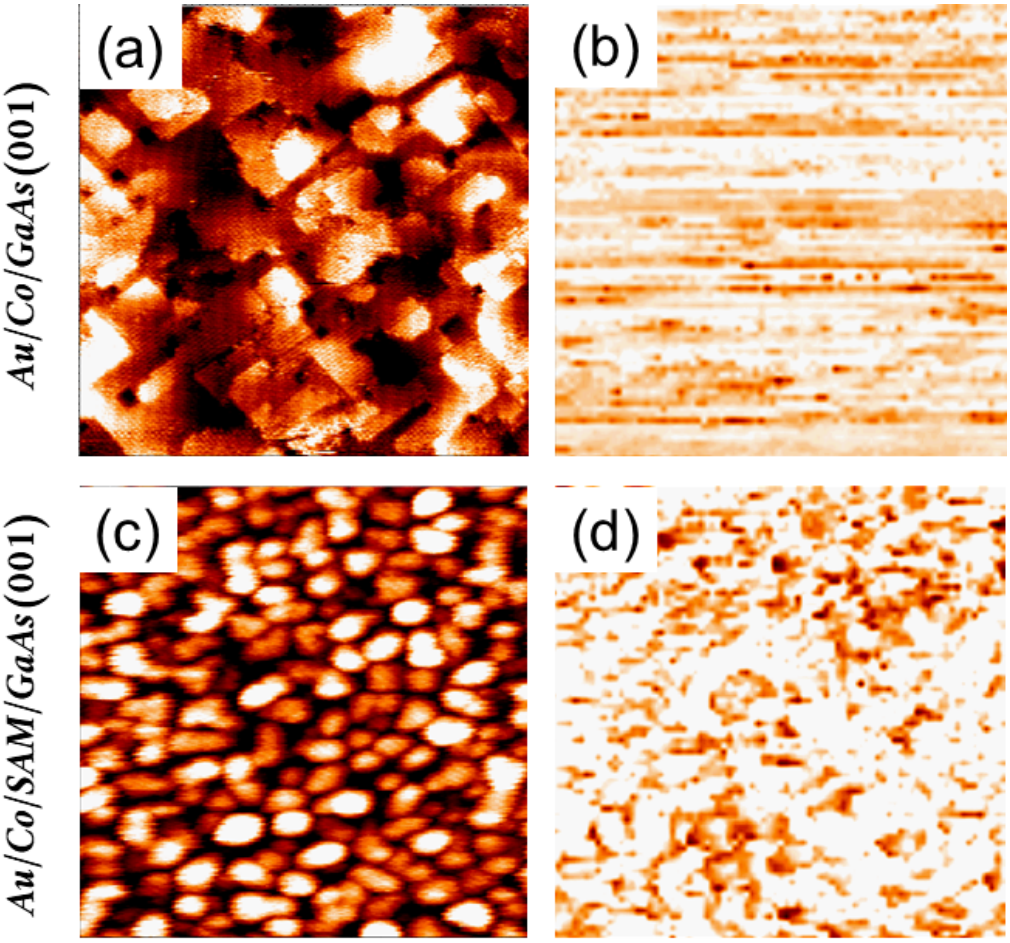

Figure 4.5: Room temperature specimens (a)STM image and (b) simultaneously recorded BEEM image of Au(4nm)/Co(3nm)/GaAs(001) at 1.8 V, $I_T = 11nA$ (color scale: 10 to 50 pA), 60 × 60 nm^2. (c) and (d) STM and BEEM images of Au(4nm)/Co(3nm)/C16MT/GaAs(001) at 1.75 V, $I_T = 15.3nA$ (color scale: 40 to 80 pA), 75 × 75 nm^2.

50×50 to 100×100 nm^2, verified to be spatially homogeneous. A fit of the spectroscopy curves with the commonly used Ludeke-Prietsch 5/2 power law (see section 2.2.1) is also displayed in these figures. For the Schottky contact, two components were introduced to obtain an accurate fit of the BEEM spectra. The first introduced threshold at $\Phi_1^{SC} = 0.660 \pm 0.006eV$ corresponds to the Schottky barrier height value at the Co/GaAs interface, i.e. to electron injection in the lowest point in energy in the GaAs conduction band, the Γ point (see figure 2.9, GaAs band structure). A second transport channel opens at $\Phi_2^{SC} = 0.989 \pm 0.007eV$ and is attributed to electron injection in the L-valley of GaAs conduction band, which is accessible at the Co/GaAs interface at higher energy. The energy difference $\Phi_2^{SC} - \Phi_1^{SC} = 0.329eV$ is in excellent agreement with the theoretical energy difference between Γ and L valleys of GaAs (0.33eV).

The same fitting procedure was applied to the grafted sample (Figure 4.6.b), leading basically to almost perfectly identical results. Two thresholds were introduced, Φ_{SAM}^1 and Φ_{SAM}^2, with absolute values equal to Φ_1^{SC} and Φ_1^{SC} within the data and fitting procedure uncertainties. We further checked that this observation was reproducible while recording BEEM data on various locations on the same sample. Figure 4.6.c presents the typical maximal dispersion of the data that can be observed on one junction with or without SAM, while moving the STM tip laterally by several 10μm around center of the patterned junction (diameter 350μm). The observed experimental dispersions are similar on both samples, and likely due to local metal thickness variations at the edge of the junction patterned by shadow mask deposition. A more complete representation of BEEM data dispersion is presented in Figure 4.6.d. The same fitting procedure was employed to extract the first and second thresholds values Φ_i, and the associated spectral weights a_i for several local averaged spectra (average of 200 spectra as in Figure 4.6.a and 4.6.b) measured with the same experimental conditions, this time on several tip position on a given junction (STM tip lateral motion of several micron) and over different junctions (patterned over several $10mm^2$ on sample surface). For both RT samples, with and without grafted SAM, the threshold values and associated spectral weights are spread around similar absolute values and with similar radial dispersions on this (a_i Φ_i) map. From this statistical study, we can observe that RT deposition of Au/Co on the SAM results in hot electron transmission identical to the Au/Co/GaAs Schottky contact. We thus conclude to an homogeneous and complete RT diffusion of the Co layer through the SAM over macroscopic regions, in good agree-

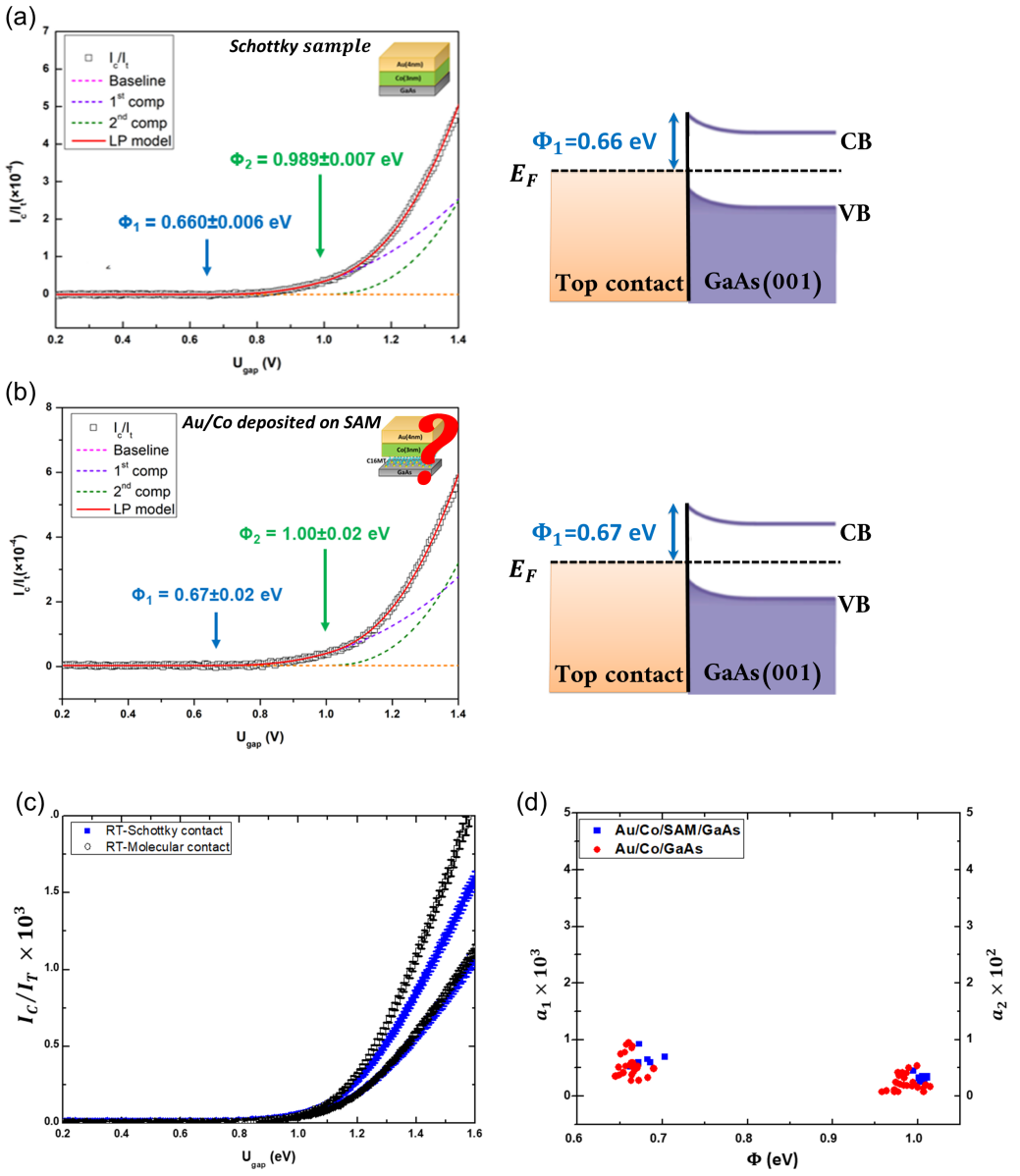

Figure 4.6: Local BEEM spectroscopy curves (average of 400 measurement points over a typical $75 \times 75nm^2$ surface) measured on the RT deposited $Au/Co/GaAs(001)$ (a) and $Au/Co/C16MT/GaAs(001)$ (b) samples. Tunnel current was set to 10nA and 15nA respectively. (c) Typical maximum data dispersions observed for both samples while moving the STM tip laterally over the same junction. (d) (a_i, Φ_i) representation of the experimental dispersion of the first and second thresholds values and associated spectral weights obtained by a Ludeke-Prietsch 5/2 power law fit of local BEEM spectra measured on various locations of various junctions for both RT deposited samples, with and without SAM.

ment with the previous XPS analysis. With our metal deposition chamber geometry (i.e. for our Co evaporation source, at our evaporation temperature, and for our source/sample distance), we could not observe by BEEM any local regions with significantly lower electron transmission that could be associated to a locally preserved molecular patch at the interface.

4.4.2 BLAG Technique Specimens

A set of samples prepared by BLAG technique, Schottky ($Au(4m)/Co(3nm)/-GaAs(001)$) and molecular samples ($Au(4m)/Co(3nm)/C16MT/GaAs(001)$) has been investigated and is presented in the following section.

The two Schottky and molecular BLAG-samples have been studied by STM and BEEM. The STM images of these two samples are displayed in Figure 4.7.a and .c. The Au/Co islands with typical lateral size of 8-15 nm are typical of a poly-crystalline structure in both Schottky and molecular specimens. In the case of Schottky sample the presence of Xe layer prevents a formation of an epitaxial Co/Au layer. The simultaneously collected BEEM current for both samples are presented in Figure 4.7.b and .d. The electron transmission through the $Au/Co/GaAs(001)$ Schottky contact presents moderate local variations correlated with the grain morphology. These correlations are this time not clearly related to local thickness variation in the metal film but rather to variable metal crystallite orientation on the GaAs(001) lattice, resulting in small variation of the electron transmission at the interface. The BEEM image for SAM-sample shows an homogeneous interface with a low current level and no sign of pinholes. The BEEM spectroscopy has been complementary used to explain the electron transport in the two BLAG samples.

Figure 4.8.a presents a representative local BEEM spectroscopy curve (average of 400 individual spectra over a 100 $\times$ 100 nm^2 area) obtained on the reference $Au/Co/GaAs$ Schottky contact deposited using BLAG. The Ludeke-Prietsch fit is also presented leading to a first threshold at $\Phi_1 = 0.82 \pm 0.03eV$ and a second component at $\Phi_2 = 1.11 \pm 0.03eV$. The energy difference between the two thresholds is again in good agreement with the energy separation between the bottoms of the Γ and L valleys of GaAs conduction band. The Schottky barrier height at the Co/GaAs(001) interface is thus determined to be 0.82eV for a BLAG prepared sample, with a 0.16eV increase of barrier height compared to the room-temperature deposited Schottky contact. This significant Schottky barrier height increase

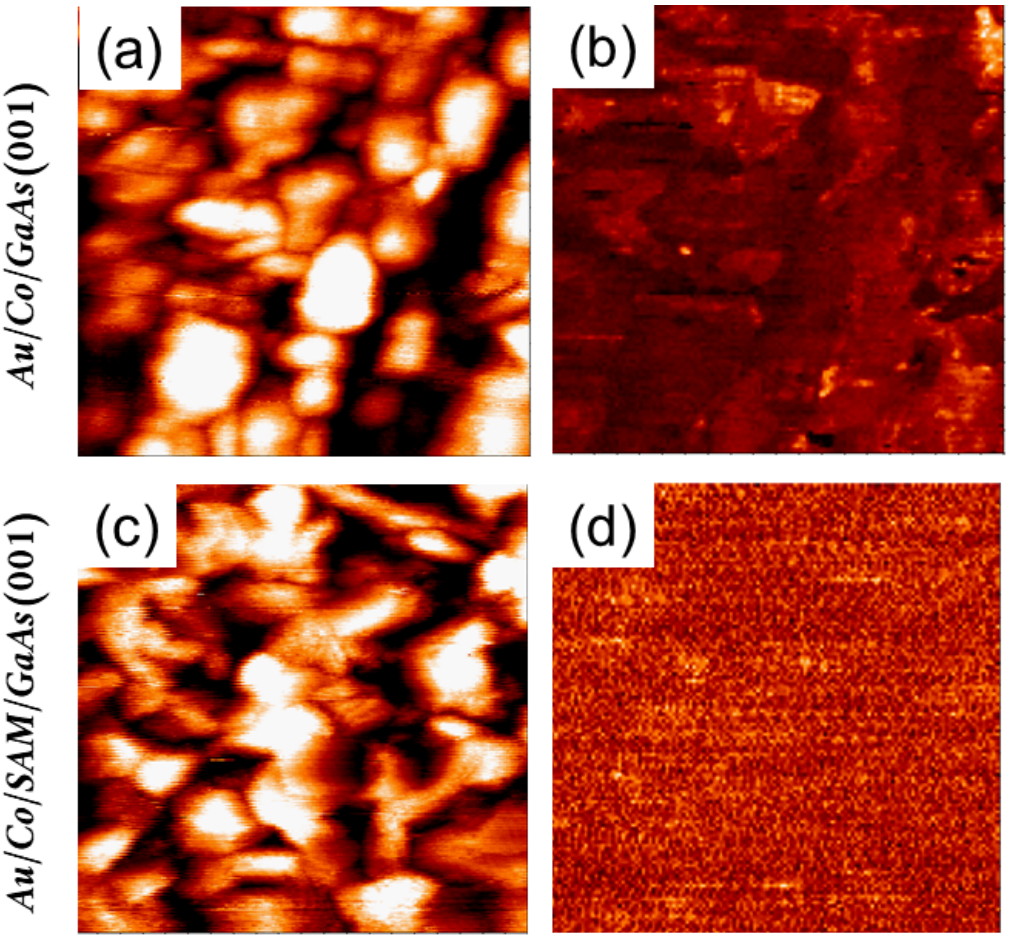

Figure 4.7: BLAG specimens (a)STM image and (b) simultaneously recorded BEEM image of Au(4nm)/Co(3nm)/GaAs(001) at 1.82 V, $I_T = 15nA$ (color scale: 85 to 110 pA), 100 × 100 nm^2. (c) and (d) STM and BEEM images of Au(4nm)/Co(3nm)/C16MT/GaAs(001) at 1.81 V, $I_T = 10nA$ (color scale: 16 to 20 pA), 100 × 100 nm^2.

is due to the fact that Co BLAG deposition prevents the formation of the interface CoGa alloy as confirmed by XPS (shown in Figure 4.4.b). The formation of this chemically abrupt Co/GaAs interface results in a different and higher Schottky barrier height value.

Figure 4.8.b shows a typical BEEM spectroscopy curve obtained with the same BEEM protocol on the $BLAG{-}Au/Co/C16MT/GaAs(001)$ structure. The overall magnitude of the BEEM signal on this sample has this time drastically decreased compared to the reference BLAG-Schottky contact, as observed on Figure 4.8.c where the two spectra are presented on the same graph. For instance, the BEEM current at 1.6eV is roughly 20 time larger on the Schottky contact than on the SAM sample. This supplementary strong additional attenuation of the hot-electron beam is attributed to the presence of a preserved molecular layer at the interface by using BLAG deposition. Since homogeneous BEEM images similar to Figure 4.8 (d) could be obtained at various measurement points of the junction and as well as on different junctions, we conclude that the SAM was efficiently protected by the Xe layer during the soft-landing process on a large scale.

Ludeke-Prietsch fits of the BEEM spectra were possible on the BLAG-$Au/Co/C16MT/GaAs(001)$ sample using only a single component with a threshold value $\Phi_1 = 0.90 \pm 0.03eV$ (Figure 4.8 (b) and (d)). This value, significantly larger than the Schottky barrier height in the BLAG-$Au/Co/-GaAs(001)$ reference is associated to the Γ valley of GaAs conduction band. The Γ point has shifted higher in energy by 0.08eV after insertion of the SAM due to the interface electrostatic dipole introduced by the molecules as previously observed in the $Au/C16MT/GaAs(001)$ system [67]. Alkanethiols are indeed polar molecules with a typical dipole value estimated to be 2-3 Debye [101]. Previous investigation of BLAG-prepared $Au/C16MT/GaAs(001)$ samples have shown BEEM spectra presenting two transport channels [68, 67]. At low energy, a first transport channel by electron tunnelling trough the SAM into the Γ valley of GaAs was first observed. At higher energy, a clear second threshold was observed and attributed to the opening of a transport channel in the LUMO states of the SAM. Since with a cobalt top contact deposited on the molecular layer only one transport channel is observed, we assume that the LUMO states of the SAM are located lower in energy at the metal/molecule interface for the $Co/C16MT/GaAs$ system than for $Au/C16MT/GaAs$. This idea is supported by the electronegativity values of the two considered metals which governs the Fermi level position at the metal/molecule interface. Indeed, the significantly lower Pauling elec-

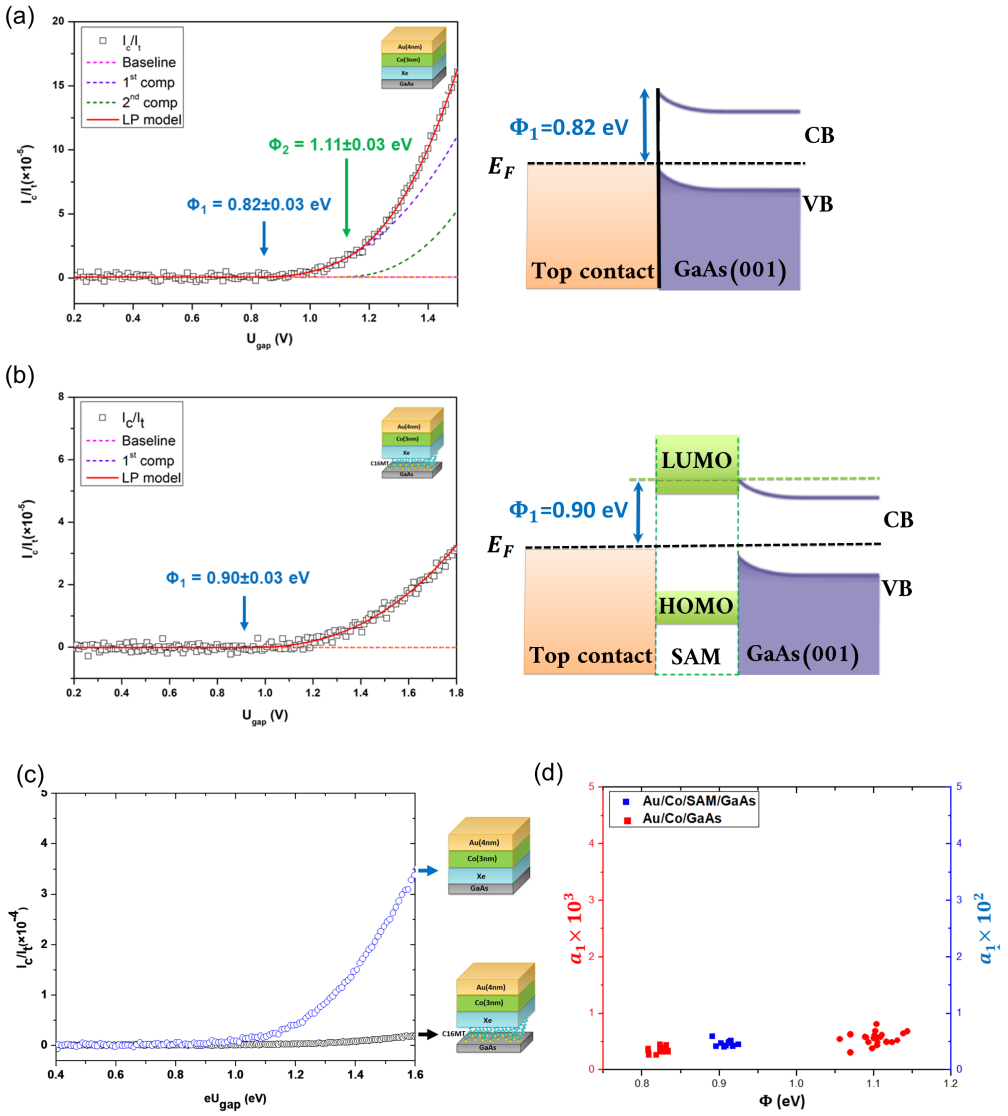

Figure 4.8: BEEM spectra of (a) $Au(4nm)/Co(3nm)/GaAs(001)$ and (b) $Au(4nm)/Co(3nm)/C16MT/GaAs(001)$ both prepared by BLAG, scaled to show properly the two-component fit using LP model, average of 400 spectrum at (a) $U_{gap} = 2.3V$, $I_t = 15.0A$ and (b) $U_{gap} = 2.0V$, $I_t = 15.0A$, (c) comparison of the BEEM spectra magnitudes obtained on the reference BLAG Schottky contact (blue dots) and SAM sample (black dots), (d) spectral weight for Schottky (red axis, 10^3) and molecular (blue axis, 10^2) BLAG-samples, each dot has been extracted from a spectrum of average 200 individual spectra.

tronegativity in cobalt (1.88) than in Au (2.54) will favour a lower tunnel barrier at the Co/C16MT interface than at the Au/C16MT [102], and thus LUMO states lower in energy. If the LUMO states energy lowers around the conduction band minimum, the tunnel transport channel through the SAM will disappear, and a single transport channel is possible by direct electron propagation on the LUMO states to the Γ-valley of GaAs at low energy (see band diagram in figure 4.8 (b)).

Conclusion

A complementary study of XPS, STM/BEEM images and BEEM spectroscopy have illustrated the efficiency of BLAG method in achieving pinhole-free molecular junctions. XPS investigation has shown that RT Co deposition on SAM results in a strong metal penetration through SAM, on macroscopic scale. In parallel, the BEEM images of $Au/Co/C16MT/GaAs(001)$ BLAG-samples has demonstrated homogeneous junctions without electrical shorts, locally. Moreover, the measured BEEM spectra concludes to the presence of molecular LUMO states around $\Phi = 0.90 \pm 0.03eV$ from the Fermi level. Therefore, we confirm that BLAG technique has been successfully employed to achieve a pinhole-free junction of $Au/Co/C16MT/GaAs(001)$, macroscopically and microscopically by XPS and STM/BEEM, respectively.

5

Magnetic tunnel junction preparation

Introduction

In this chapter, we focus on the preparation of $Au/Co/SAM/Fe/MgO(001)$ tunnel junctions. For this purpose, we have designed and prepared shadow masks for *in situ* FM electrode depositions to fabricate junctions in the crossbar geometry. Electrical transport properties (I(V)) of these junctions are mainly the focus of the following chapter. The magnetic properties of the patterned bottom Fe electrode were simulated using micromagnetic simulations. Moreover, the magnetic properties of Co deposited on Xe layer has been studied using Magneto-optic Kerr effect (MOKE) measurement.

To study a fully prepared *in situ* system, we use shadow masks for FM deposition. Even though FM deposition through a shadow mask comes with its difficulties, it allows us to prepare the full junction *in situ* including BLAG deposition of the top FM electrode. This also allows us to characterize the prepared magnetic tunnel junctions immediately after growth, without any additional lithography process. In order to design our tunnel junctions compatible for transport measurements, crossbar geometry has been proposed. In the crossbar geometry the two ferromagnetic electrodes are configured perpendicular to each other and are separated by the organic self-assembled monolayer; the intersection between the top and bottom electrode defines the junction area. To achieve this geometry for our system, two sets of shadow masks have been designed and machined using laser-cutting technique. Two

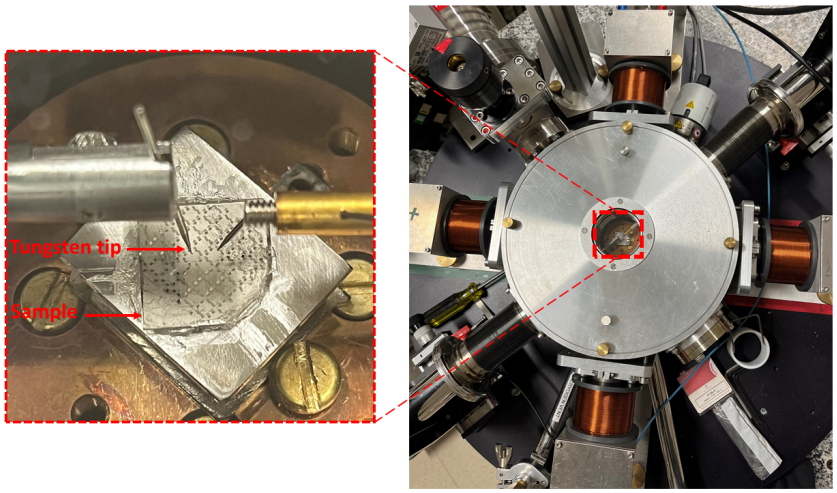

Figure 5.1: Experimental setup used for transport measurements: On the right, cryostat, the sample introduction window is visible in the center, zoomed in on this window, (in left) where we distinguish sample and the tips allowing contact with the junctions top and bottom electrodes.

different junction sizes were prepared and studied, from macroscopic to micronic scale.

5.1 Transport measurements

The transport measurements are carried out in a liquid nitrogen cryostat under vacuum (pressure of the order of several 10^{-6} $mbar$), shown in Figure 5.1. The contact on the pads of the top/bottom electrodes are ensured by tungsten tips visible in this figure. The current versus voltage measurements are made by a picoammeter (Keithley 6482), and the temperature can be varied between 77 K and 292 K. The cryostat is connected by triaxial cables making it possible to measure low currents with a low noise level.

5.2 Large area junctions ($50 \times 50\ \mu m^2$ up to $100 \times 100\ \mu m^2$)

A set of two *in situ* transferable shadow masks have been designed for bottom- and top- electrode deposition, shown in Figure 5.2. The first mask for bottom electrode patterning is made of Copper/Beryllium containing 3 vertical strips with width $w = 50\mu m$, and 3 strips of $w = 100\mu m$, a length $L = 7mm$ for all strips (figure 5.2a). A second mask, for the top-electrode evaporation, contains this time horizontal strips ($L = 800\mu m$, $w = 50\mu m$ or $w = 100\mu m$), to obtain the desirable crossbar geometry, shown in Figure 5.2b. The strips in both masks end with a large pad at both sides, for transport measurements connections. To prepare suitable transport measurement samples, the first shadow mask is placed on the sample holder (displayed previously in section 2.2.3) for bottom-electrode (Fe) deposition on MgO(001) substrate, displayed in Figure 5.2c. Mask is removed for Fe layer annealing, and the entire substrate is exposed to the vapor of molecules during grafting of the Fe electrode. The second mask is then placed on the sample for the top electrode (Au/Co) BLAG deposition (Figure 5.2d), resulting in a full stack of $Au/Co/SAM/Fe$ patterned junction. The different width for strips in the bottom and top electrode provides junctions with three different surface area size of $50 \times 50\ \mu m^2$, $50 \times 100\ \mu m^2$ and $100 \times 100\ \mu m^2$.

5.2.1 Transport properties of large area junctions

Transport measurements are done at both room and low temperature for junctions characterization. For I(V) curve measurement, the flow of current is measured at a given applied voltage, varying between -0.1 V and +0.1 V with 1mV steps. The performed I(V) measurement on top and bottom electrodes with $w = 50\mu m$ results in experimental resistance of 430Ω and 30Ω for Fe and Co/Au strips, respectively. In the following section, the expected strips resistance is calculated using the equation below:

$$R = \frac{\rho_i \times L}{w \times t} \tag{5.1}$$

where ρ_i corresponds to resistivity of metal i, $\rho_{Fe} = 9.7 \times 10^{-8}(\Omega.m)$, $\rho_{Co} = 8.24 \times 10^{-8}(\Omega.m)$ and $\rho_{Au} = 2.44 \times 10^{-8}(\Omega.m)$ [103], L to the length of the strip, and w and t are assigned to width and thickness of strips. The

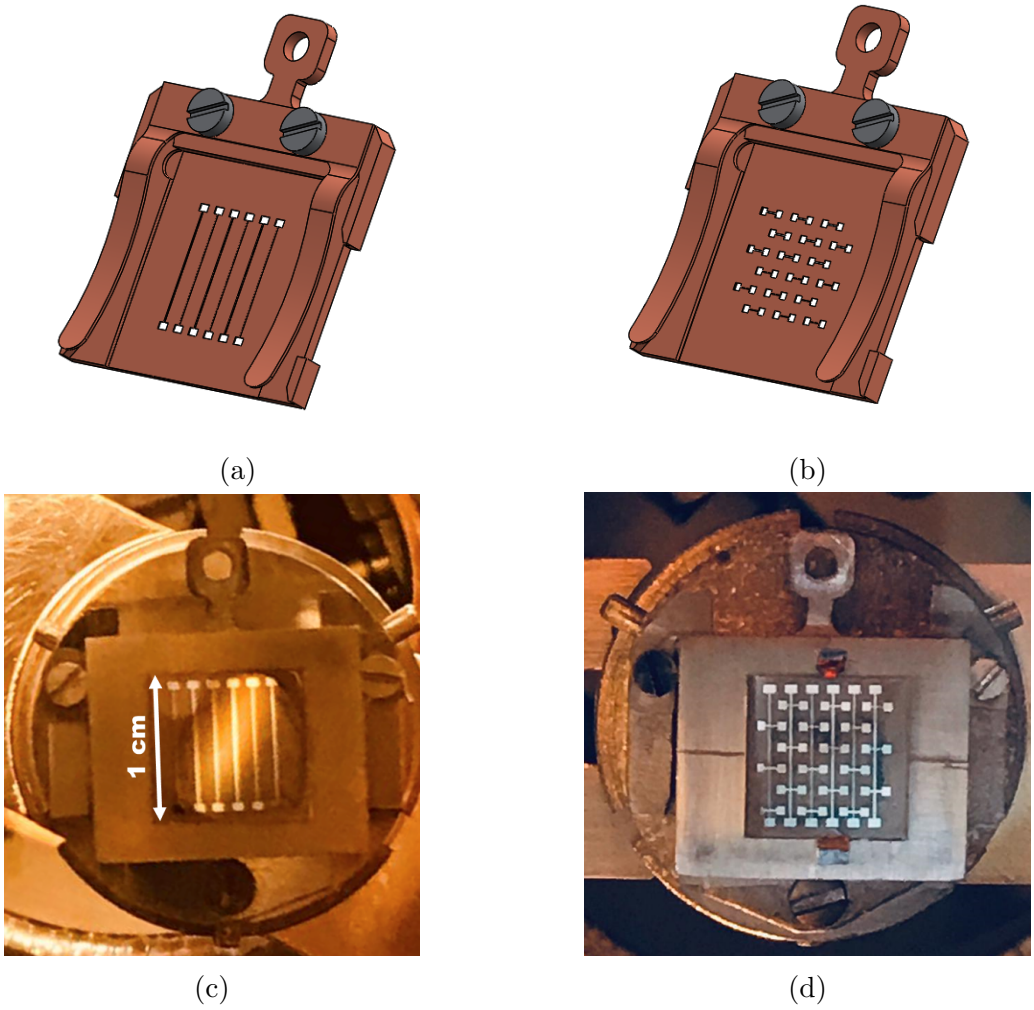

(a) (b)

(c) (d)

Figure 5.2: (a) 3D design of the shadow mask to deposit the bottom electrode and (b) for the top-electrode deposition, (c) image of bottom electrode deposition Fe(30nm), (d) Top view of the full junctions.

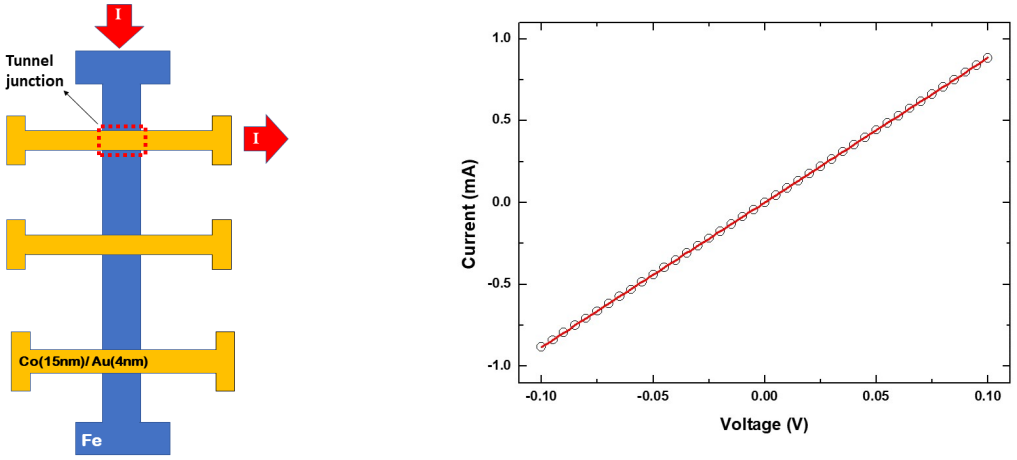

(a) (b)

Figure 5.3: (a) Schematic top view of the junctions prepared for transport measurements, (b) I(V) curve measured on a $50 \times 50\ \mu m^2$ junction at 77K.

calculated resistance strips are 490Ω and 20Ω for Fe(30nm) bottom electrode and Co(15nm)/Au(4nm) top electrode, respectively. The resistance of the top Co/Au bilayer was calculated by considering two resistance in parallel. These calculated resistances are in good agreement with the measured values.

The I(V) curve has been also measured throughout the tunnel junction. The current flows through the Fe layer, passing the SAM, and is collected from the pad connected to the Co/Au strip, shown in Figure 5.3a. The measured I(V) curve through a $50 \times 50\ \mu m^2$ junction at 77K is displayed in 5.3b. As it is shown, a linear I(V) curve is observed, typical of an ohmic contact between top and bottom electrode. In another word, there is at least one pinhole over a junction which causes short circuit. The recorded I(V) in this case results in a resistance 120Ω. The expected resistance for metallic paths, without the presence of molecular barrier, in this geometry calculated to be 135Ω, additionally, the expected resistance for the hexadecanethiol barrier for a $50 \times 50\ \mu m^2$ junction is reported to vary between 4Ω and 400Ω [104]. Since the resistance of the organic barrier is in the same range of the strips' resistance, it might be problematic to discriminate junctions with or without pinholes for this junction surface. We thus introduced a new set of masks to define smaller junctions where the resistance ratio between strips and tunnel barrier will be more favorable.

5.3 Micronic junctions ($5 \times 5\mu m^2$)

The design the new tunnel junction's surface area size has been a compromise between several factors to develop the most efficient junction. The expected resistance for hexadecanethiol-based junctions is required to be larger than the metallic resistance of the strips, at least by one order of magnitude, allowing to distinguish short circuited junctions. Pierre Seneor and his colleagues have studied $Co/C16MT/NiFe$ junctions with the size of $1\mu m^2$ [104], where they establish a highly dispersed junction resistance varying between $10k\Omega$ and $1M\Omega$. Since, employing BLAG technique gives us the opportunity to increase the junction size, we have decided to investigate a larger tunnel junction. For a junction area of $5 \times 5\mu m^2$ a resistance between 400Ω and $40k\Omega$ is estimated, whereas a only resistance of 320Ω for Fe and 290Ω for Co/Au strips is expected for $L = 500\mu m$. At this scale, patterning a $5 \times 500\mu m^2$ strip in a thick CuBe foil using laser-cutting is quite challenging, at the resolution limit of this machining technology. Second, next issues appear for shadow mask deposition when the width of the design is significantly smaller than mask thickness.

5.3.1 Quality of the masks

The quality of the strips deposited through shadow masks with narrow strips have been studied by electron microscopy. We first used a Au thermal evaporator for our first tests. This evaporator is made of a tungsten metal boat containing gold pellets. The Au charge is heated up by direct current passing through the tungsten boat. This evaporation source is generating an evaporation flux with a broad evaporation angle, and the source/sample distance is large, typically 40cm. Two masks with CuBe thicknesses of 50 and 20μm where used to evaporate 110nm thick Au strips with targeted width of 5 and 10μm. Masks were placed in contact to the Si test substrate. The resulting deposited strips were checked optically (Figure 5.4). We observed that up to 40% of the patterned strips present discontinuities as shown in 5.4 (c). These discontinuities could be correlated to the presence of residual metal particles in the mask that are generated during the machining process. For the continuous strips, some local constrictions could also be commonly observed and again correlated to the presence of particles partially occluding the mask. These artefacts could be suppressed by a careful ultrasonic cleaning of the mask before UHV introduction. The width of the deposited strips

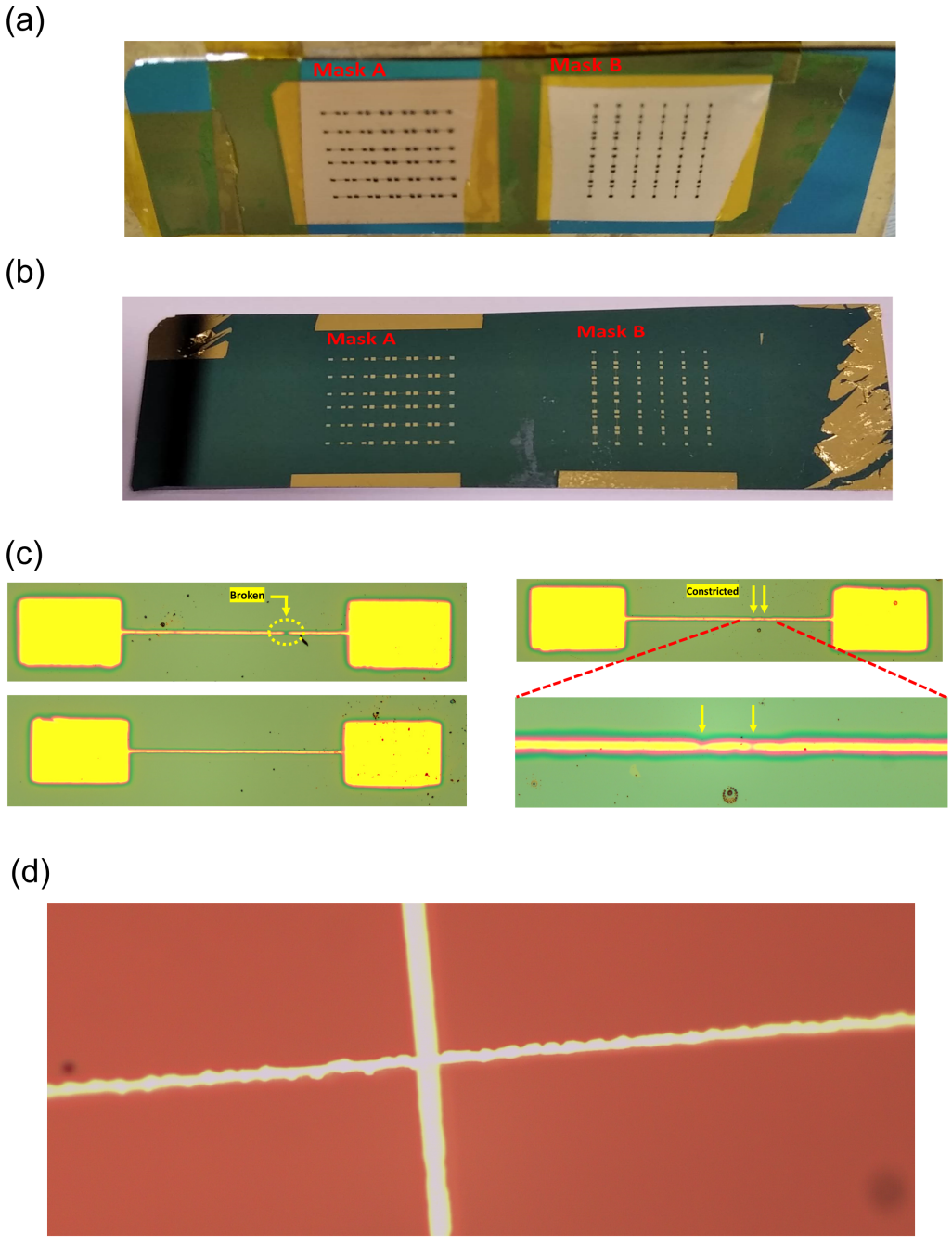

Figure 5.4: (a) $CuBe_2$ shadow mask, Mask A with the thickness of $tmaskA = 50$, and mask B $tmaskB = 20\mu m$ (b) 110nm Au deposition through the Mask A and mask B, (c) Optical images of a broken and a complete strip with the width of $w = 10\mu m$ on mask A, (d) Optical images of a strip containing a zoom-in constriction, $w = 5\mu m$.

was observed to broadened compared to the mask dimension with a typical deposit width of 13-14μm for w=10μm, and a typical deposit width of 7-9μm for w=5μm. This blurring effect is attributed to the bad collimation of the evaporation flux for this evaporator.

In a second step, we used MBE deposition, i.e. a much more directional metal atom flux to pattern a metallic electrode on Si. This time, the highly collimated evaporation beam resulted in a much sharper transfer of the pattern from mask to the deposit, revealing details of the mask intrinsic edge roughness induced by the laser machining technique. Figure 5.4. (d) presents a high magnification optical image of a deposit patterned with a w=5μm mask. Some regular well-defined constrictions are observed periodically at the edge of the track and are due to the shape of the laser pulses used to machine the mask. A single laser scan line was indeed used to open the narrow stripe in the CuBe foil. The pulsed focused laser generates consecutive holes which partially overlap while scanning the CuBe foil, resulting in this typical morphology. The width of the deposit is oscillating between 3-5μm along the strip axis, confirming a conform transfer of the pattern on surface. It should be noted that these lateral constrictions might increase the strip resistance and eventually modify the magnetic properties of the FM patterned electrodes.

5.3.2 AFM study of the full junction prepared by shadow mask deposition

The final masks design is presented in Figure 5.5. It allows to pattern a matrix of $7 \times 7 = 49$ junctions on a $1cm^2$ MgO substrate. The bottom electrode axis is vertical, with a width w=5μm, and a length L=500μm. The top electrode mask is identical, with a simple 90° rotation of the pattern. The contacting pads at the end of the stripes are $200 \times 250\mu m^2$. Figure 5.5 (b) and (c) present optical micrographs of the junction after deposition of the bottom electrode and at the end of the deposition process.

A complete $Au(4nm)/Co(15nm)/C16MT/Fe(30nm)/MgO$ magnetic tunnel junction was prepared with the final set of masks and imaged by atomic force microscopy. Figure 5.6 (a) $20 \times 20\mu m^2$ AFM image of a sample region around an intersection of the top/bottom electrode, i.e. close to a junction. The Fe top electrode presents the typical morphology previously reported

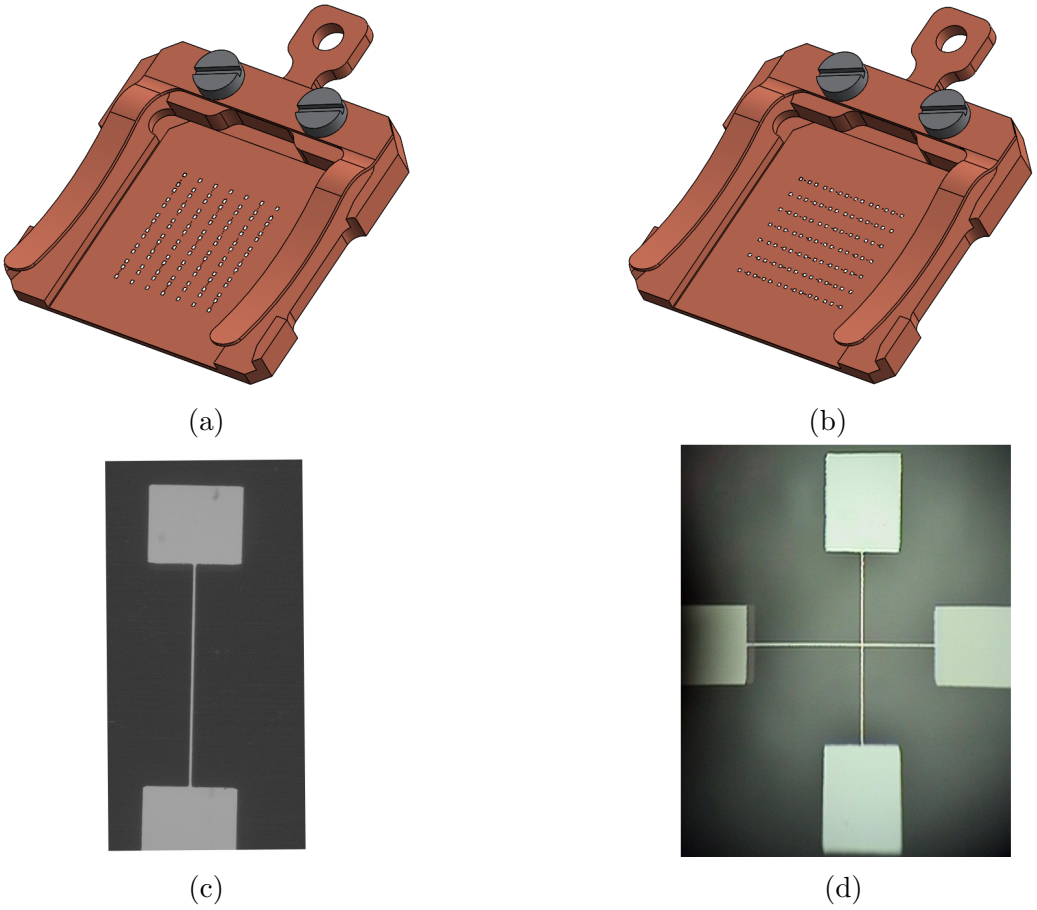

(a) (b)

(c) (d)

Figure 5.5: (a) 3D final design of the used shadow mask to deposit the bottom electrode and (b) for the top-electrode deposition, (c) Optical microscope image of bottom electrode deposition through the mask shown in (a), with magnification of $4\times$, $w = 5\mu m, l = 0.5mm$, (d) Top view of the full junction, $4\times$ optical microscope image.

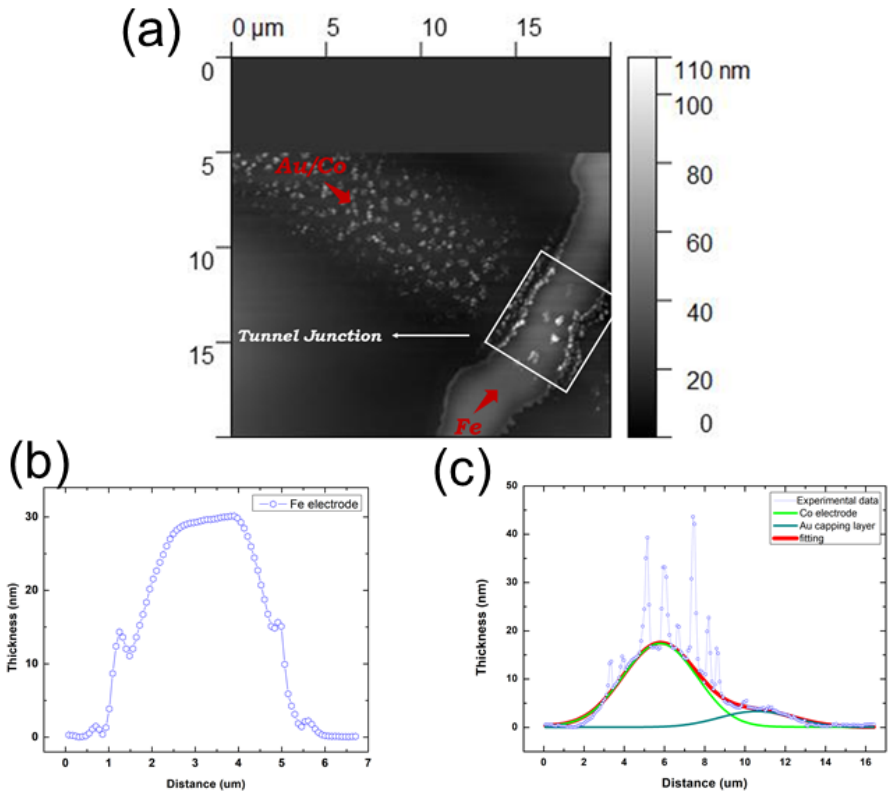

Figure 5.6: (a) $20 \times 20\mu m^2$ AFM image of the Fe and Au/Co electrodes, the $Au/Co/C16MT/Fe$ tunnel junction is located at this intersection, shown in white square, (b) and (c) present a profile line of Fe and Au/Co electrode, respectively.

by optical microscopy, with the presence of lateral constrictions. The minimum/maximum width that could be measured by AFM along the Fe strip were in the 2.2μm/4.2μm range typically. A halo is visible at the edges of the Fe deposit and also visible on the profile perpendicular to the Fe strip presented in Figure 5.6 (b). This halo is attributed to a partial lateral oxidation of the Fe electrode by oxygen diffusion from the edge. Sample was indeed left for 5 days in ambient atmosphere before being imaged by AFM.

The Au/Co top electrode presents some specific features at the surface : a high density of bright spots, with local heights up to 45nm are observed all over the top electrode. Since these features are only observed on the Au/Co layer, it is probably related to the BLAG deposition process, and likely to the

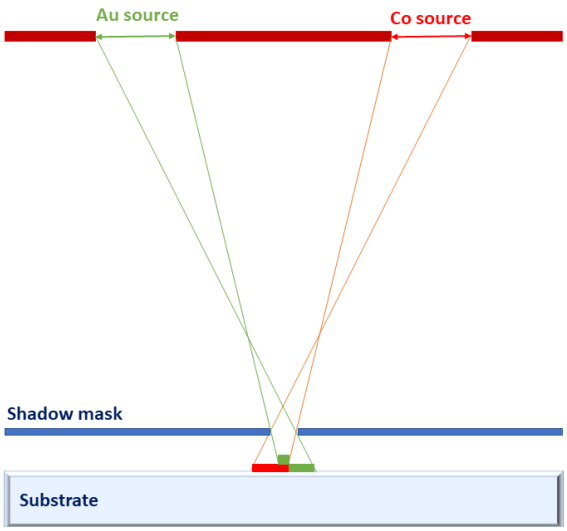

Figure 5.7: Schematic of Au and Co deposition, with different incident angles, through a shadow mask.

formation of defects during the post-growth Xe desorption process through the metal layers. An additional interesting point is observed on a topography profile perpendicular to the Au/Co top electrode (see in figure 5.6 (c)). The Au layer appears as shifted laterally with respect to the cobalt layer. This can be clearly evidenced by fitting the profile with two peaks associated to the two layers. The deduced thicknesses match the targeted one for both Au and Co. This shift is due to the slightly different incidence angles of the Au and Co evaporation sources with respect to sample surface normal during the BLAG deposition as explained in figure 5.7. This led us to suppress the Au cap layer in the following, in order to avoid the potential presence inside the prepared junctions of local $Fe/C16MT/Au$ regions.

5.3.3 Transport properties on micronic junctions

Transport measurements have been performed on samples with the new proposed geometry as explained in section 5.1. These samples have been prepared employing BLAG technique. The measured I(V) curves at 77K on the Fe and Co/Au strips alone demonstrate an average electrode resistance of around 1 $k\Omega$ and 2 $k\Omega$, respectively. As one of the most significant ob-

jectives of this work relies on preventing the metal penetration through the molecular layer, we report that typical 50% of measured junctions in each sample have shown no signs of a short-circuit (9 out of 19 junctions). To be more precise, these junctions have shown high resistance values, and non-linear I(V) curves due to electron tunneling through the SAM. The measured resistances of these junctions without pinholes are scattered between 4.9 $k\Omega$ and 2.2 $M\Omega$, presented in Figure 5.8. This broad distribution of junction resistances is typical of what is reported in these junctions integration alkanethiol SAM and attributed to local variation of the SAM barrier thickness due to variable partial metal penetration in the organic layer [104]. The average resistance value on with ohmic behaviour junctions is measured to be $R = 1.9\ k\Omega$. The measured resistances observed on ohmic or tunnel junctions for several prepared samples remains in this range. To have a clearer perspective, a sample has been prepared at room temperature. The transport measurements on this sample present junction resistances of less then 900 Ω, whereas twice larger resistances have been observed on broken junctions in BLAG samples. Hence, BLAG technique has certainly reduced the top-electrode penetration compared to RT deposition. In Figure 5.9, we represent typical I(V) measurements on the two RT- and BLAG- samples. In this figure, a large slope difference around $V = 0\ V$is observed between RT-sample and the BLAG-sample. Moreover, this current Vs. voltage figure displays the non-linearity of the BLAG sample vividly. Whereas the RT sample results in a linear I(V) curve, coherent with Ohm's law.

From our experience, the junctions located at the edges of the substrate are more likely to contain a shortcut which suggests a possible geometrical effect during junction growth. Moreover, we observe that all junctions seem to break over a few days time. This short lifetime can be due to progressive formation of metallic filaments through the SAM induced by the applied electric field. Such hypothesis might be checked by BEEM by measuring a Co/SAM/GaAs junction before and after bias application. Another possibility to explain our junctions frangibility is to consider progressive lateral oxidization of the junctions by their edges. To tackle this obstacle, we are considering an Al capping layer on the sample. Hence, the thin Al layer will be oxidized at ambient pressure, and form an insulatorAl_2O_3. This insulator layer might protect the junctions and the strips from oxidization.

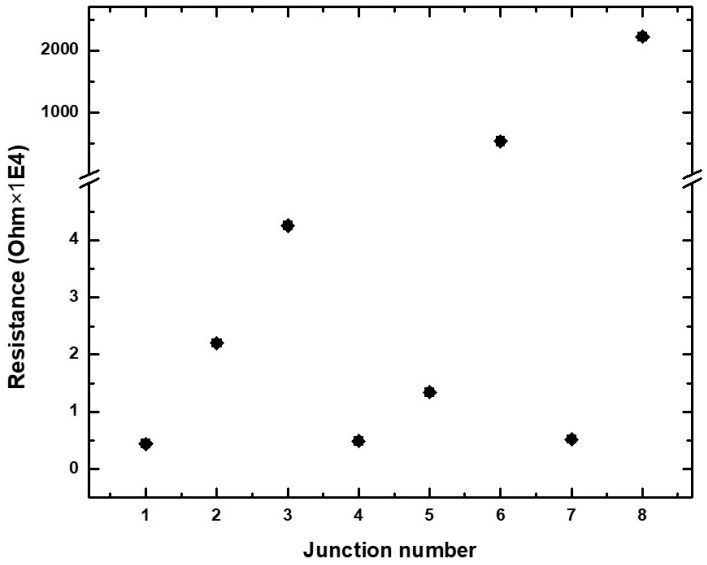

Figure 5.8: Measured resistance of 5×5 μm^2, $Au/Co/SAM/Fe$ molecular junctions presenting non linear I(V) curves.

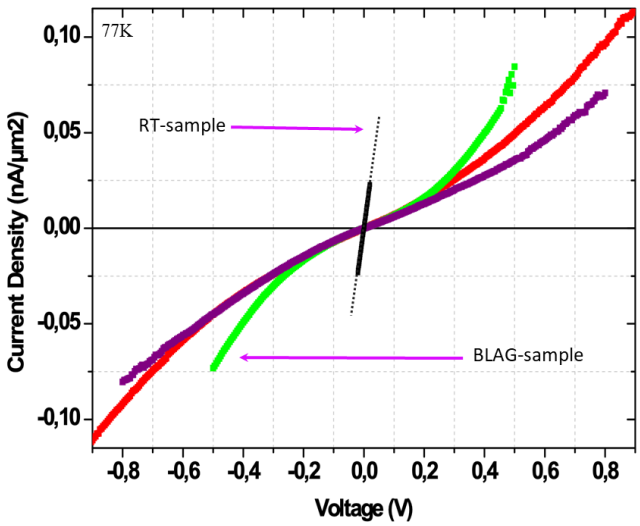

Figure 5.9: Measured resistance of molecular junctions with a surface area of 5×5 μm, $Au/Co/SAM/Fe$, for the sample prepared at RT(RT-sample) and with BLAG technique(BLAG-sample).

5.3.4 Analysis of the I(V) curves

Several theories have been established to describe the flow of current between two metal layers separated by thin insulating film. The electronic current can flow through the insulating region between the two electrodes if: (a) the electrons in the electrodes have enough thermal energy to surmount the potential barrier and flow in the conduction band. (b) the barrier is thin enough to permit its penetration by the tunnel effect.

Commonly used theories have considered conditions for low temperatures so that thermal current could be neglected, thus restricting the electron transport between electrodes to the tunnel effect. The theory applied to the problem of the systems with rectangular barrier has been established by Sommerfeld and Bethe [105], and by Holm [106]. In 1963, John G. Simmons derived a formula for the electric tunnel effect through a generalized barrier [107]. The widely used Simmons model is an excellent approximation. This model expresses the tunneling current density through a barrier in the tunneling regime of low and high bias. The tunneling currents in both bias regimes are exponentially dependent on the barrier width d. In the low-bias regime, the tunneling current density is:

$$J \propto \frac{1}{d}\, exp(-\beta_0\, d) \tag{5.2}$$

where β_0 is a bias-independent decay coefficient:

$$\beta_0 = \frac{2(2m^{1/2})}{\hbar}\, \alpha(\Phi_B)^{1/2} \tag{5.3}$$

m corresponds to the electron mass and Φ_B to the barrier height. The α parameter is a unitless adjustable parameter that modifies Simmons model for a molecular system [108].

In the high-bias regime:

$$J \propto \frac{1}{d^2}\, exp(-\beta_v\, d) \tag{5.4}$$

where V is the applied bias and β_v is a bias-dependent decay coefficient

$$\beta_v = \frac{2(2m^{1/2})}{\hbar}\, \alpha \left(\Phi_B - \frac{eV}{2}\right)^{1/2} = \beta_0 \left(1 - \frac{eV}{2\Phi_B}\right)^{1/2} \tag{5.5}$$

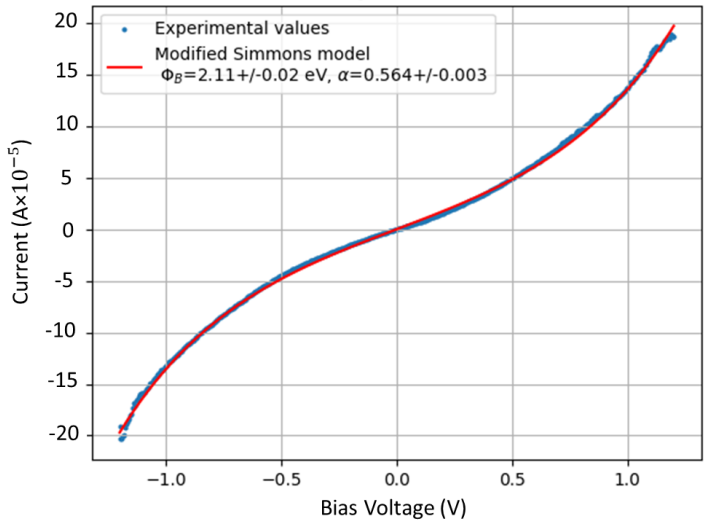

Figure 5.10: Experimental I(V) curve from a junction of Au/Co/C16MT/Fe, fitted by modified Simmons model, $\Phi = 2.11 \pm 0.02eV$ and $\alpha = 0.564 \pm 0.003$.

At high bias, β_v decreases as bias increases, which results from a barrier lowering effect due to the applied bias.

The α parameter is introduced to provide a way of applying the tunneling model of a rectangular barrier to tunneling through a nonrectangular barrier [109]. It can also be an adjustment to account for the effective mass (m*) of the tunneling electrons through a rectangular barrier [110]. $\alpha = 1$ corresponds to the case for a rectangular barrier and bare electron mass.

Wenyong Wang and his colleagues have investigated $Au/C16MT/Au$ tunnel junctions [108], and have reported $\Phi_B = 1.4 \pm 0.03eV$ and $\alpha = 0.68 \pm 0.01e$, using a modified Simmons model. The modified Simmons model have been used to fit the extracted I(V) curves of the tunneling junctions. Our colleague, Sylvain Tricot has provided us with a Python program to tailor data. The modified Simmons model for the junctions (red and black curves of figure 5.9) leads to typical $\Phi = 2.11 \pm 0.02eV$ and $\alpha = 0.564 \pm 0.003$, presented in Figure 5.10. These extracted Φ and α have been calculated for a molecular thickness of $d = 1.8nm$. An increase of 10% in molecular thickness leads to a decrease of 10% in α. Although, the molecular thickness does not seem to affect the barrier height, Φ.

5.4 Bottom electrode magnetic properties

Computational micromagnetics is widely used for the design and development of magnetic devices. The theoretical background of these simulations is the continuum theory of micromagnetism. It treats magnetization processes on a significant length scale which is small enough to resolve magnetic domain walls and large enough to replace atomic spins by a continuous function of position. Micromagnetism is based on continuum theoretical expressions for the intrinsic energy terms contained in the internal energy. These theoretical expressions have been derived and explained on NIST website, [92, 111, 112], herein we briefly describe the general perspective. In a ferromagnetic material, the magnetization orientation is determined by the minimization of the system Gibbs free energy of the system. This Gibbs free energy contains several contributions :

1) The exchange energy : in a ferromagnet, the exchange interaction (or Heisenberg interaction) tends to align the magnetic moment in a parallel configuration. This short range interaction is characterized by the exchange constant A, equal to $1.13 \times 10^{-11} J.m^{-1}$ in iron.

2) The magnetocrystalline anisotropy energy : in a crystalline ferromagnet, the symmetry of the atom local environment defines preferential (respectively unfavourable) orientations of the magnetic moments along specific crystal directions defining magnetic easy axis (respectively hard axis).

3) The Zeeman energy related to the magnetic energy of a magnetic moment in a magnetic field promoting parallel alignment of the magnetization in the field direction.

4) The magnetostatic energy, also called dipolar interaction energy. In a ferromagnetic material the presence of a permanent magnetization results in the apparition of surface or bulk magnetostatic charges generating a demagnetizing field in space. This dipolar interaction is a long-range interaction. In a magnetic element presenting a shape anisotropy, the magnetostatic energy will be minimum when the magnetization is aligned along the long axis of the system.

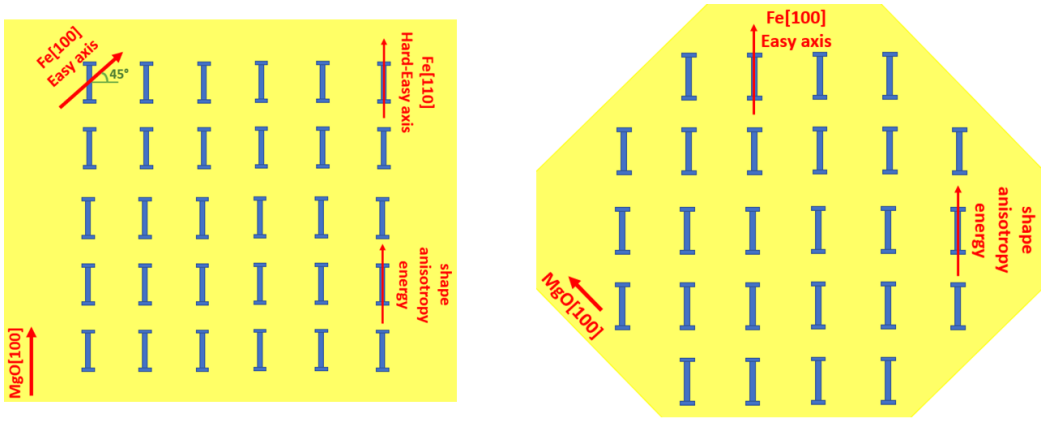

(a) (b)

Figure 5.11: Definition of the two considered sample geometries for the 30nm thick patterned bottom Fe(001)/MgO electrode. (a) Sample 1 : Strip axis of the bottom electrode is parallel to the Fe [110] direction. (b) Sample 2 : Strip axis of the bottom electrode is parallel to the Fe [100] direction.

We used the OOMF code (Object Oriented Micromagnetic Framework) to compute the minimum of our system energy using a finite difference method [113]. The material magnetic parameters (exchange constant, saturation magnetization, magnetocrystalline anisotropy constants) are obtained from tabulated values for bulk iron [114]. The bottom electrode structural properties been well studied in chapter 2.2.4. The MBE deposition of 30nm of Fe on MgO(001) results in mono-crystalline Fe(001) which magnetic properties are well documented in literature [115]. In these films, magnetization is in plane of the film, and the [100] and [010] axis are equivalent easy axis, while the [110] and [1-10] axis are equivalent hard-easy axis. We simulated the hysteresis loops of our patterned bottom Fe electrode for two different geometries that were experimentally considered.

First, in sample 1, we placed the long axis of the electrode parallel to the [110] direction of the Fe film, i.e. with the long axis parallel to the edges of the MgO(001) substrate (see figure 5.11 (a)). In this case, we will have a competition between the shape anisotropy of the strip which favours an easy axis parallel to the strip long axis, and the magnetocrystalline anisotropy, which would rather align the magnetization 45° away from the strip axis.

Second, for sample 2, we oriented the long axis of the Fe strip parallel to

the [100] direction of the Fe film, i.e. parallel to the diagonal of the MgO substrate (see figure 5.11 (b)). In this case we will have a minimum for both anisotropy and magnetostatic energy when the magnetization of the stripe is parallel to the [100] direction, defining unambiguously a system easy axis.

We also introduced in the micromagnetic simulation a periodic modulation of the Fe strip width with an amplitude and spatial period similar to the one experimentally observed on Figure 5.4 (d). This edge roughness might indeed modify the magnetic behaviour of the strip by eventually trapping some magnetic domains between two constrictions.

Figure 5.12 present the calculated hysteresis loops simulated using OOMF for the two samples geometry. For sample 1, we first applied the magnetic field along the Fe [100] axis (Figure 5.12 (a)) and then along the Fe [110] axis (Figure 5.12 (b)). We still observe a magnetic behaviour dominated by the magnetocrystalline anisotropy of the Fe film. The Fe [100] is indeed observed to still be an easy axis, while the [110] axis is still slightly harder despite the introduced shape anisotropy. Both configuration result in a soft bottom electrode that can be easily switched under low external magnetic field. Finally, Figure 5.12 (c) presents the hysteresis loop simulated for sample 2, with applied field along the Fe [100] axis. Without surprise, a square hysteresis loop typical of an easy axis is obtained with a low coercive field. It should be mentioned that even with magnetic initialization of the system state with opposite magnetic domains within two consecutive constrictions, no domain pinning was observed in this soft system. To conclude on the bottom electrode magnetic properties, micromagnetic simulations has revealed a globally soft bottom electrode, with magnetic properties that are marginally modified by the patterning process and that should be easily switched under moderate magnetic field value, which is convenient for future magnetotransport experiments.

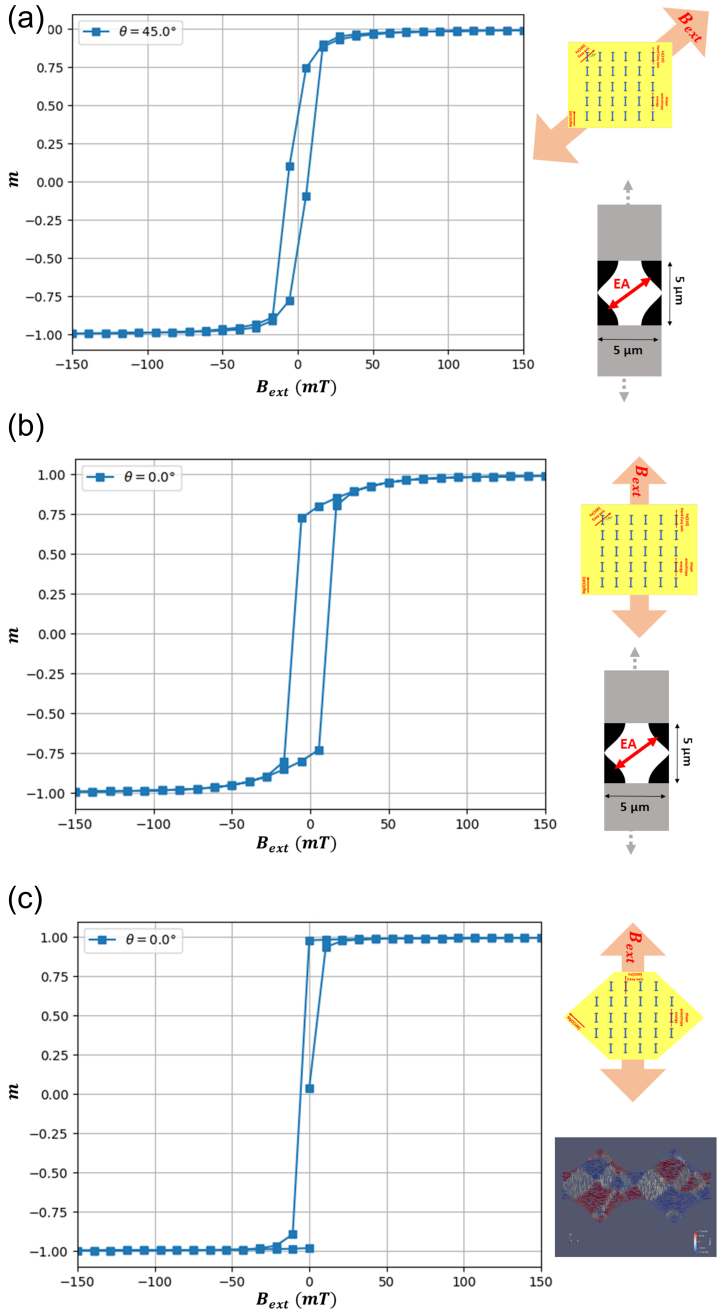

Figure 5.12: Simulated hysteresis loops obtained on sample 1 : (a) for a magnetic field applied along the [100] Fe axis; and (b) for a magnetic field applied along the [110] Fe axis. (c) : Simulated hysteresis loop obtained on sample 2for a magnetic field applied along the [100] Fe axis. The inset presents the unit cell used to simulate the periodic edge roughness experimentally observed after shadow mask deposition.

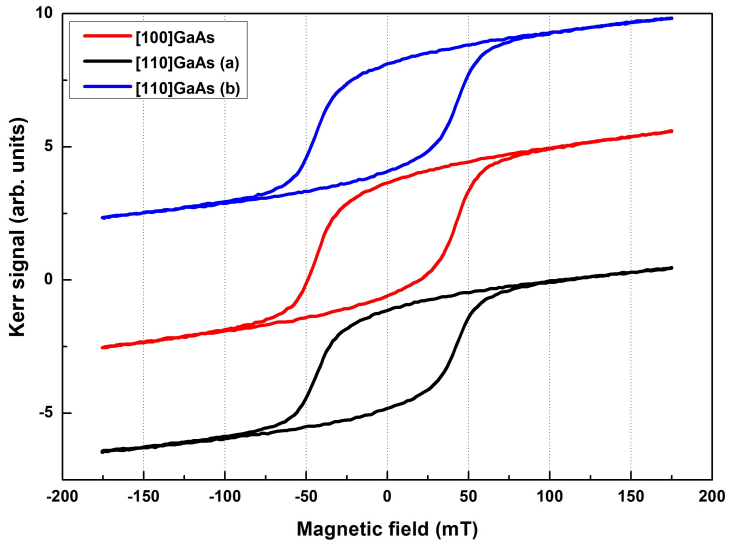

Figure 5.13: Magneto-optical Kerr Effect measurements on BLAG-[Au(4nm)/Co(15nm)]/C16MT/GaAs(001), sample with magnetic field along GaAs[100] direction, GaAs[110] and GaAs[1-10] direction.

5.5 Top electrode magnetic properties

The magnetic properties of Co layer deposited on SAM using BLAG has never been studied. Since the crystalline structure of this layer in unknown, we used Magneto-optical Kerr Effect (MOKE) to study the behaviour of this film. For this measurement, a layer of 15nm Co have been deposited on a full plane of grafted GaAs(001) (no shadow mask), using BLAG method. A 4nm Au cap layer was the deposited. The MOKE measurements for magnetic field applied along the 3 main high-symmetry directions of the substrate are given in Figure 5.13. The Co film has shown no in-plane anisotropy, and a hard magnetic behaviour with a coercive field of $H_c = 40\ mT(400\ Oe)$. This isotropic behaviour might be a consequence of the granular morphology of the BLAG deposited layer. From this observation, we suspect that a Co strip with the width of a few μm have a pinned magnetization along the strips due to the shape anisotropy.

Conclusion

Crossbar geometry junctions are developed for *insitu* BLAG-sample preparation compatible with transport measurements. A set of transferable shadow masks has been designed and studied for several surface area junctions. Transport measurements of junctions with a surface area of $5 \times 5\mu m^2$ have shown tunneling behaviour on 50% of junctions. The measured resistance of these junctions without pinholes is scattered between $4.9k\Omega$ and $2.2M\Omega$. To investigate the magnetic properties of these MTJs, micromagnetic simulation of the bottom-electrode has been studied, resulting in a globally soft bottom electrode with modifiable magnetic properties by patterning process. Whereas, MOKE measurements on Co deposited on C16MT by BLAG technique leads to a conclusion of pinned magnetization along the strips with the width of a few μm due to the shape anisotropy.

6

Conclusion and Outlook

The proposal of this work in the field of molecular Spintronics was essentially inspired by the tremendous emphasis given to spinterface concept over the past few years. The somehow uncontrolled influence of metal/molecule interface on spin-transport caused a growing demand for a well-characterized and well-controlled MTJ system for both fundamental and applied physics purposes. On the other hand, practical fabrication of these FM/SAMs/FM systems is still one major challenge of this field, due both to the intrinsic difficulties to contact a SAM and the additional issue of oxide-free ferromagnetic electrode interfaces. The main objectives of my Ph.D. was to contribute to both of these aspects addressing the precise interface characterization of model hybrid magnetic tunnel junctions up to the development of an innovative fabrication method.

To pursue the former of these objectives, a $Au/Co/Hexadecanethiol/Fe/-MgO(001)$ model MTJ was successfully developed in ultrahigh vacuum environment. The junction growth was monitored after every preparation step by a multi-technique approach. We have achieved a dense Hexadecanethiol self-assembled monolayer grafted on a single crystalline Fe(001) surface as shown by electron spectroscopy analysis. The filled state band structure of SAM/bottom-electrode (Fe) was also investigated by UPS. The top ferromagnetic Co electrode deposition was studied at various scales and optimized by combining macroscopic XPS and nanoscale BEEM experiments. Buffer-layer assisted growth of this cobalt top contact was proved to prevent the strong metal diffusion through the organic monolayer observed for room temperature deposition. The local empty state electronic properties of Co/SAM

interface were further investigated by BEEM, giving access to the LUMO states of the SAM.

The latter objective was addressed by developing a complete *in situ* MTJ patterning process by using shadow mask deposition. This method is compatible with BLAG deposition of the top FM electrode and allowed to prepare $5 \times 5\mu m^2$ junctions in the crossbar geometry that can be measured immediately after growth. Preliminary results show a high success ratio, with typically half of the prepared junctions presenting non linear I(V) curves, signature of a pinhole-free device at a relatively large scale.

The natural outlook of this work will first focus on the magneto-transport study of the BLAG prepared junctions. First experiments in this direction have been performed. Some tunnelling junctions were observed to present reproducible abrupt resistance changes up to 60% at 77K, but the shape of the R(H) curves is for the moment not understood and should be further studied to discriminate a possible TMR effect from eventual metallic filament formation in the barrier. Generally speaking, the junction patterning process will also need to be improved to increase the lifetime of the prepared MTJs. At this point, junction aging is indeed limiting the experimental time to typically 48h before the junction breaks. This timescale is not sufficient to run a complete magneto-transport study with variable applied bias, temperature, field direction. A surface passivation will be first needed to avoid lateral oxidation of junctions in ambient conditions. Second, we plan to use BEEM to investigate the time evolution of the initially homogeneous Co/SAM interface under applied bias, and study the eventual post-growth formation of pinholes by electromigration.

Other molecules will be considered for the SAM tunnel barrier. The developed MTJ growth process is highly versatile and will be easily adapted for this purpose. We will first consider alkanedithiols SAM, which will allow to connect the upper chain end to the Co top contact. Previous BEEM studies have revealed a significant reduction of the pinhole density for room-temperature formed Au/alkanedithiols junctions. This should also be considered as a promising direction to improve the robustness of the prepared MTJs. On a midterm perspective, the use of unsaturated molecules, presenting lower HOMO-LUMO gap, as well as alternative anchor group will also be considered to modify the electronic coupling at the metal/molecules interfaces, and thus the system spinterfaces.

The implementation of a liquid nitrogen cryostat on the STM/BEEM setup will allow to significantly improve the setup signal to noise ratio, open-

ing the way to a BEEM study under magnetic field of a full MTJ stack grown on GaAs. This study will allow to probe the energy dependence of the spin-transport on the molecular unoccupied orbitals which is of high interest from a fundamental point of view. Finally, another powerful complementary spectroscopic tool, i.e. spin- and angle-resolved IPES (Inverse Photoemission Spectroscopy), will be considered to investigate the spin-resolved electronic properties of the unoccupied molecular orbitals after grafting of the ferromagnetic surface. This study will be done in collaboration with A. Tejeda (Laboratoire de Physique des Solides, Université Paris-Saclay-CNRS). Spin-IPES will allow to directly analyse the spin resolved energy broadenings and energy shifts of the frontier unoccupied orbitals which are responsible of the magneto-transport properties of these hybrid systems. A grafting module adapted to the LPS setup was designed and will allow to investigate *in situ* prepared $SAM/Fe(001)/MgO(001)$ bottom electrode. The measured spinterface electronic properties will be useful inputs to analyse the magneto transport properties of MTJs integrating the exact same model bottom electrode and SAM.

Résumé

Introduction et contexte de l'étude:

L'électronique de spin moléculaire repose sur l'intégration de monocouches organiques auto-assemblées (SAM) au sein de dispositifs spintroniques tels que vannes de spin et jonctions tunnel magnétiques. Ces dispositifs hybrides permettent à la fois de tirer parti de la grande versatilité offerte par la synthèse organique à bas coût de molécules fonctionnelles et du long temps de vie du spin observé dans ces matériaux à faible couplage spin-orbite et faible interaction hyperfine.

Depuis la première observation d'un fort signal de magnétorésistance à basse température dans une jonction intégrant une couche moléculaire [16], la spintronique moléculaire s'est heurtée à un certain nombre de difficultés scientifiques et techniques. Ainsi, lors du dépôt d'une électrode métallique ferromagnétique sur un SAM, la diffusion du métal à travers le peigne moléculaire conduit fréquemment à la formation de courts-circuits (pinholes en anglais) dans les jonctions formées, rendant ces dispositifs inopérants. Dans la littérature, les solutions proposées [45, 47] pour limiter ce problème reposent sur la lithographie de jonctions de dimensions latérales très réduites. Si la structuration de jonctions de dimensions latérales nanométriques permet effectivement de diminuer la probabilité de présence de pinholes, le taux de jonctions moléculaires non court-circuitées (typiquement 30% des jonctions lithographiées pour les meilleurs résultats reportés dans la littérature) reste insuffisant pour une future intégration viable dans des composants

nanoélectroniques. Par ailleurs, un second verrou, scientifique cette fois, concerne la diversité de comportement de magnéto-transport reportés sur les jonctions moléculaires fonctionnelles. Ainsi pour un même système hybride, les mesures de magnétorésistance reportées par différents groupes peuvent s'avérer contradictoires. Pire, au sein d'un seul et même échantillon, des jonctions tunnels magnétiques peuvent présenter des magnétorésistance positives ou négatives, pointant du doigt l'existence d'un paramètre expérimental non contrôlé dans ces échantillons. Ces fluctuations expérimentales ont été attribuées à des variations de propriétés électroniques aux interfaces entre électrodes ferromagnétiques inférieures et supérieures et le peigne moléculaire. Ainsi, le modèle de « spinterface » développé par Barrault et al. [18] prend-il en compte le rôle de l'hybridation d'interface entre les orbitales moléculaires frontières des molécules et les électrodes métalliques ferromagnétiques de la jonction, démontrant la nécessité d'un contrôle poussé des interfaces dans ces jonctions hybrides. Lors de la formation de la spinterface (cf figure Résumé 1), le modèle de Barrault démontre que dans le cas d'un fort couplage électronique à l'interface ferromagnétique/molécules, les états électroniques participant au transport tunnel peuvent présenter une inversion de polarisation en spin par rapport à l'électrode ferromagnétique nue. A contrario, dans le cas d'une faible hybridation d'interface, les premières orbitales moléculaires inoccupées peuvent jouer le rôle d'un filtre à spin, renforçant, sans changement de signe cette fois, la polarisation en spin des états électroniques participant au transport. Dans ce contexte, les objectifs de ce travail de thèse sont :

i de réaliser entièrement sous ultravide la croissance de jonctions tunnel magnétiques hybrides intégrant un SAM comme barrière isolante greffé sur une électrode inférieure ferromagnétique monocristalline. Cette approche vise à développer à terme un système modèle parfaitement contrôlé, en particulier au niveau de ses spinterfaces.

ii de développer une méthode de dépôt de l'électrode ferromagnétique supérieure sur le peigne moléculaire permettant de réduire voire d'empêcher la formation de pinholes. Ceci permettra à terme de préparer des jonctions tunnel magnétiques hybrides viables et homogènes à grande échelle.

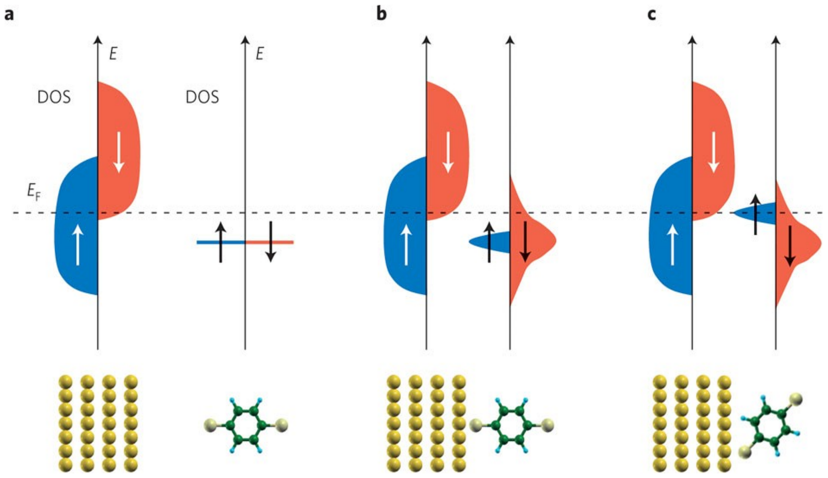

Figure Résumé 1: Principe de formation d'une spinterface entre une molécule et une électrode ferromagnétique [21]. (a) molécule découplée du ferromagnétique ; (b) molécule greffée en faible interaction électronique avec la surface ; (c) molécule greffée en forte interaction électronique avec la surface.

Choix de l'électrode ferromagnétique inférieure et greffage :

Le greffage sous ultravide de différentes électrodes ferromagnétiques (Co polycristallin, $Fe_{80}Ni_{20}$ monocristallin, Fe polycristallin et monocristallin) par une monocouche moléculaire d'hexadécanethiols ($CH_3(CH_2)_{15}SH$) a été systématiquement étudié par spectroscopie de photoélectrons X (XPS). Pour les électrodes polycristallines de fer et cobalt, l'analyse des spectres de photoémission démontre la présence d'atomes de souffre non liés à une chaine carbonée en surface, témoignant d'une dégradation partielle des chaines alcanes en surface après greffage. Le taux de greffage en molécules intactes est en conséquence réduit et le SAM formé peu dense et donc peu à même de former une barrière tunnel continue. A contrario, nous avons observé que le greffage de couches de Fe(001) épitaxiées sur substrat de MgO(001) permettait de former un SAM dense et préservant l'intégrité des molécules, avec un site de surface greffé sur quatre, soit la densité maximale attendue compte tenu de l'encombrement stérique des molécules. Ce SAM dense greffé sur Fe(001) a par ailleurs démontré en XPS une stabilité thermique jusque $90 \circ C$ et une morphologie de surface très plane à grande échelle comme observé en STM .

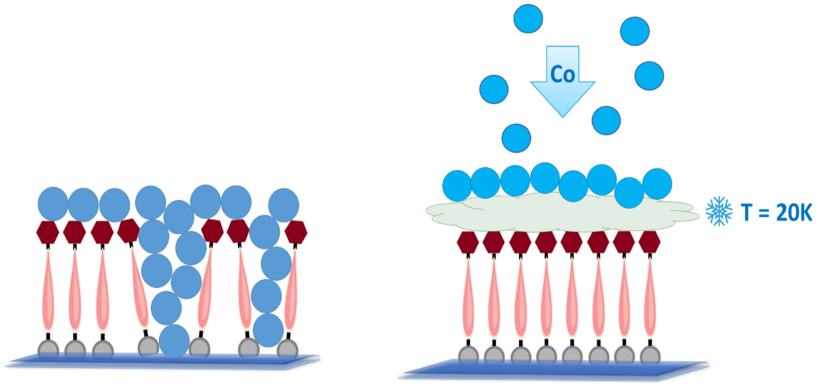

Figure Résumé 2: Formation de pinholes par diffusion du métal à travers un peigne moléculaire et principe du dépôt de l'électrode ferromagnétique supérieure de cobalt par la méthode de soft-landing.

Le système $CH_3(CH_2)_{15}SH$ greffé sur Fe(001) a en conséquence été retenu pour la suite de notre étude.

Dépôt et caractérisations de l'électrode supérieure :

Une électrode supérieure ferromagnétique de cobalt a été retenue afin d'obtenir un champ coercitif différent de l'électrode inférieure de Fe(001) dans les jonctions tunnel préparées. Dans un premier temps, nous avons étudié le dépôt d'électrodes de cobalt à température ambiante sur un SAM d'hexadécanethiols greffé sur GaAs(001) afin de pouvoir caractériser à l'échelle nanométrique l'homogénéité des contacts formés par microscopie à émission d'électrons balistiques (BEEM) [54]. Les cartographies BEEM révèlent une transmission électronique homogène à toutes les échelles pour ces échantillons réalisés à température ambiante. Les courbes de spectroscopie BEEM démontrent elles une signature spectroscopique parfaitement identique à un contact Schottky Co/GaAs(001) démontrant la diffusion massive et homogène du cobalt à température ambiante à travers le peigne moléculaire. Des expériences XPS menées lors du dépôt séquentiel de cobalt sur le SAM confirment cette diffusion massive du métal magnétique à travers le SAM, des composantes de réaction typiques d'un alliage d'interface CoGa apparaissant dès les premiers

stades du dépôt. Cette diffusion à grande échelle du cobalt à travers la barrière moléculaire est à l'évidence rédhibitoire pour le développement de jonctions tunnel magnétiques avec cette méthode de dépôt.

Afin de réduire la diffusion du cobalt à travers le SAM lors du dépôt de l'électrode supérieure, nous avons mis en œuvre une méthode dite de « soft-landing » (cf Résumé 2). Cette approche consiste, après greffage, à refroidir l'échantillon à une température de 20K puis à introduire une pression partielle de gaz rare (Xénon) dans l'enceinte expérimentale afin de former une couche épaisse de Xénon solide (100nm) sur le SAM. Le dépôt de cobalt se fait alors sur la surface solide de la glace de Xénon qui joue le rôle d'une couche tampon permettant de considérablement réduire la diffusion du métal à travers le SAM. Après dépôt, l'échantillon est ramené lentement à température ambiante afin de désorber la couche de Xénon.

Nous avons étudié par XPS et BEEM des dépôts de cobalt réalisés par soft-landing sur une monocouche moléculaire greffée sur GaAs(001). L'imagerie BEEM révèle à nouveau une transmission électronique homogène latéralement, mais avec cette fois une atténuation d'un ordre de grandeur du courant comparativement au contact Schottky de référence Co/GaAs(001) préparé également par soft-landing. Cette atténuation est attribuée à la présence d'une barrière moléculaire préservée et homogène à l'interface Co/GaAs, sans pinholes détectés avec cette méthode de dépôt.

Préparation et caractérisations de jonctions tunnel magnétiques hybrides :

La dernière partie de ce travail de thèse a été dédiée au développement d'une méthode de microstructuration de jonctions tunnel magnétiques par dépôt sous masques in situ. Nous avons conçu des masques transférables et compatibles avec la méthode de soft-landing dont les motifs définis par découpe laser permettent la mise en œuvre de jonctions en géométrie cross-bar. Les dimensions des pistes et jonctions ont été optimisées afin d'atteindre une résistance de jonction moléculaire bien supérieure à la résistance des amenées de courant. Les propriétés magnétiques des deux électrodes de fer et cobalt ont été étudiées par effet Kerr magnéto-optiques et simulations micromagnétiques. Les caractérisations électriques de jonctions de surface $5 \times 5\mu m^2$ $Co/CH_3(CH_2)_{15}SH/Fe(001)$ préparées par soft-landing

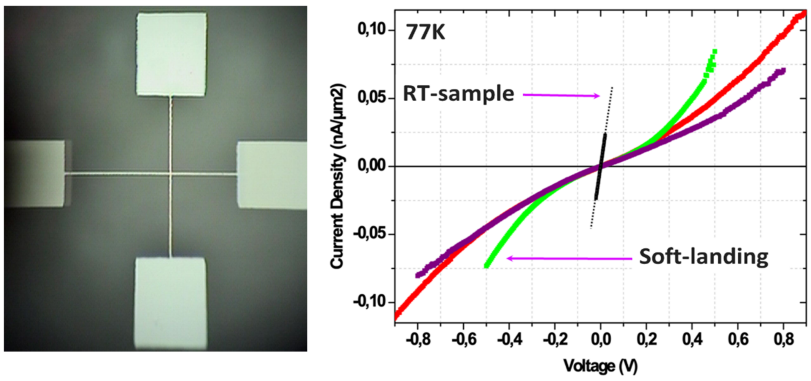

Figure Résumé 3: Jonction tunnel magnétique hybride $Co/CH_3(CH_2)_{15}SH/Fe(001)$ (surface $5 \times 5\mu m^2$) préparée par dépôt sous masque. Courbes J(V) mesurées sur des jonctions préparées par soft-landing ou à température ambiante. Une caractéristique non-linéaire associée au transport tunnel à travers le peigne moléculaire est observée pour plus de 50% des jonctions mesurées.

démontrent un transport tunnel à travers le peigne moléculaire pour plus de 50% des jonctions microstructurées (cf figure Résumé 3). Ce taux de jonctions opérationnelles tombe à 0% pour des jonctions similaires préparées à température ambiante, démontrant l'efficacité de la méthode de soft-landing pour la préparation de jonctions moléculaires de grandes surfaces.

A

Appendix

Cross section

The reference of the relative cross sections of photo-ionization is that of the carbon 1s level (C-1s). Different cross sections for the used materials in this study for $Al-K\alpha$ and $Mg-K\alpha$ X-ray sources are taken from NIST website [92] and presented in Table1.1.

Cross section		
Elements	$Mg-K\alpha$	$Al-K\alpha$
$Ni-2p_{1/2}$	7.18	7.57
$Co-2p_{3/2}$	12.2	12.62
$Fe-2p_{3/2}$	10.54	10.8
$S-2p_{3/2}$	1.47	1.72

Table 1.1

Electron Mean Free Path (EMFP)

The electron mean free path at different kinetic energies using $Al-K\alpha$ and $Mg-K\alpha$ taken from NIST website [92] is presented in Table1.2:

EMFP				
	$Mg - K\alpha$		$Al - K\alpha$	
Elements	$E_K(eV)$	EMFP ($\mathring{A}$)	$E_K(eV)$	EMFP ($\mathring{A}$)
$Ni - 2p_{1/2}$	383	7.8	616	10.5
$Co - 2p_{3/2}$	475	8.5	708	11
$Fe - 2p_{1/2}$	533	10.6	766	13.6
$Fe - 3p$	1200	19.2	1433	21.9

Table 1.2

Moreover, the EMFP λ through the Hexadecanethiol (C16MT) at the kinetic energy of each elements is presented in Table1.3.

EMFP of C16MT ($\mathring{A}$)		
Elements	$Mg - K\alpha$	$Al - K\alpha$
$Ni - 2p_{1/2}$	15.1	21.1
$Co - 2p_{3/2}$	17.8	23.5
$Fe - 2p_{1/2}$	19.2	25.2
$Fe - 3p$	35.9	41.5
$C - 1s$	30	36
$S - 2p_{3/2}$	33.1	38.9

Table 1.3

Bibliography

[1] Claude Chappert, Albert Fert, and Frédéric Nguyen Van Dau. The emergence of spin electronics in data storage. *Nature materials*, 6(11):813–823, 2007.

[2] Igor Žutić, Jaroslav Fabian, and S Das Sarma. Spintronics: Fundamentals and applications. *Reviews of modern physics*, 76(2):323, 2004.

[3] SA Wolf, DD Awschalom, RA Buhrman, JM Daughton, von S von Molnár, ML Roukes, A Yu Chtchelkanova, and DM Treger. Spintronics: a spin-based electronics vision for the future. *science*, 294(5546):1488–1495, 2001.

[4] V Dediu, M Murgia, FC Matacotta, C Taliani, and S Barbanera. Room temperature spin polarized injection in organic semiconductor. *Solid State Communications*, 122(3-4):181–184, 2002.

[5] Mario Norberto Baibich, Jean Marc Broto, Albert Fert, F Nguyen Van Dau, Frédéric Petroff, P Etienne, G Creuzet, A Friederich, and J Chazelas. Giant magnetoresistance of (001) fe/(001) cr magnetic superlattices. *Physical review letters*, 61(21):2472, 1988.

[6] Grünberg Binasch, Peter Grünberg, F Saurenbach, and W Zinn. Enhanced magnetoresistance in layered magnetic structures with antiferromagnetic interlayer exchange. *Physical review B*, 39(7):4828, 1989.

[7] M. Julliere. Tunneling between ferromagnetic films. *Physics Letters A*, 54(3):225–226, 1975.

[8] T. Miyazaki and N. Tezuka. Giant magnetic tunneling effect in fe/al2o3/fe junction. *Journal of Magnetism and Magnetic Materials*, 139(3):L231–L234, 1995.

[9] JS Moodera, LR Kinder, J Nowak, P LeClair, and R Meservey. Geometrically enhanced magnetoresistance in ferromagnet–insulator–ferromagnet tunnel junctions. *Applied physics letters*, 69(5):708–710, 1996.

[10] Michael Häfner, Janne Viljas, Diego Frustaglia, Fabian Pauly, Melanie Dreher, Peter Nielaba, and Juan Cuevas. Theoretical study of the conductance of ferromagnetic atomic-sized contacts. *Publ. in: Physical Review B 77 (2008), 10, 104409*, 77, 03 2008.

[11] Jose Maria De Teresa, Agnes Barthelemy, Albert Fert, Jean Pierre Contour, François Montaigne, and Pierre Seneor. Role of metal-oxide interface in determining the spin polarization of magnetic tunnel junctions. *Science*, 286(5439):507–509, 1999.

[12] W Xu, GJ Szulczewski, P LeClair, I Navarrete, R Schad, G Miao, H Guo, and A Gupta. Tunneling magnetoresistance observed in la 0.67 sr 0.33 mn o 3/organic molecule/co junctions. *Applied Physics Letters*, 90(7):072506, 2007.

[13] DR McCamey, HA Seipel, S-Y Paik, MJ Walter, NJ Borys, JM Lupton, and C Boehme. Spin rabi flopping in the photocurrent of a polymer light-emitting diode. *Nature Materials*, 7(9):723–728, 2008.

[14] CG Yang, E Ehrenfreund, and ZV Vardeny. Polaron spin-lattice relaxation time in π-conjugated polymers from optically detected magnetic resonance. *Physical review letters*, 99(15):157401, 2007.

[15] Stefano Sanvito and A Reily Rocha. Molecular-spintronics: The art of driving spin through molecules. *Journal of Computational and Theoretical Nanoscience*, 3(5):624–642, 2006.

[16] ZH Xiong, Di Wu, Z Valy Vardeny, and Jing Shi. Giant magnetoresistance in organic spin-valves. *Nature*, 427(6977):821–824, 2004.

[17] JR Petta, SK Slater, and DC Ralph. Spin-dependent transport in molecular tunnel junctions. *Physical review letters*, 93(13):136601, 2004.

[18] Clément Barraud, Pierre Seneor, Richard Mattana, Stéphane Fusil, Karim Bouzehouane, Cyrile Deranlot, Patrizio Graziosi, Luis Hueso, Ilaria Bergenti, Valentin Dediu, et al. Unravelling the role of the interface for spin injection into organic semiconductors. *Nature Physics*, 6(8):615–620, 2010.

[19] SL Kawahara, J Lagoute, V Repain, C Chacon, Y Girard, S Rousset, A Smogunov, and C Barreteau. Large magnetoresistance through a single molecule due to a spin-split hybridized orbital. *Nano letters*, 12(9):4558–4563, 2012.

[20] Nicolae Atodiresei, Jens Brede, Predrag Lazić, Vasile Caciuc, Germar Hoffmann, Roland Wiesendanger, and Stefan Blügel. Design of the local spin polarization at the organic-ferromagnetic interface. *Physical review letters*, 105(6):066601, 2010.

[21] Stefano Sanvito. The rise of spinterface science. *Nature Physics*, 6(8):562–564, 2010.

[22] H Vázquez, R Oszwaldowski, P Pou, J Ortega, R Pérez, F Flores, and Antoine Kahn. Dipole formation at metal/ptcda interfaces: Role of the charge neutrality level. *Europhysics Letters*, 65(6):802, 2004.

[23] Mickael L Perrin, Christopher JO Verzijl, Christian A Martin, Ahson J Shaikh, Rienk Eelkema, Jan H Van Esch, Jan M Van Ruitenbeek, Joseph M Thijssen, Herre SJ Van Der Zant, and Diana Dulić. Large tunable image-charge effects in single-molecule junctions. *Nature nanotechnology*, 8(4):282–287, 2013.

[24] F Djeghloul, F Ibrahim, Matteo Cantoni, M Bowen, L Joly, S Boukari, P Ohresser, F Bertran, P Le Fèvre, P Thakur, et al. Direct observation of a highly spin-polarized organic spinterface at room temperature. *Scientific reports*, 3(1):1–7, 2013.

[25] Hossam Haick and David Cahen. Making contact: Connecting molecules electrically to the macroscopic world. *Progress in Surface Science*, 83(4):217–261, 2008.

[26] Marta Galbiati. *Molecular spintronics: from organic semiconductors to self-assembled monolayers*. Springer, 2015.

[27] Yueh-Lin Loo, Robert L Willett, Kirk W Baldwin, and John A Rogers. Interfacial chemistries for nanoscale transfer printing. *Journal of the American Chemical Society*, 124(26):7654–7655, 2002.

[28] Yueh-Lin Loo, David V Lang, John A Rogers, and Julia WP Hsu. Electrical contacts to molecular layers by nanotransfer printing. *Nano Letters*, 3(7):913–917, 2003.

[29] Julia W.P. Hsu. Soft lithography contacts to organics. *Materials Today*, 8(7):42–54, 2005.

[30] JG Kushmerick, DB Holt, JC Yang, J Naciri, MH Moore, and Ry Shashidhar. Metal-molecule contacts and charge transport across monomolecular layers: measurement and theory. *Physical review letters*, 89(8):086802, 2002.

[31] James G Kushmerick, David B Holt, Steven K Pollack, Mark A Ratner, John C Yang, Terence L Schull, Jawad Naciri, Martin H Moore, and Ranganathan Shashidhar. Effect of bond-length alternation in molecular wires. *Journal of the American Chemical Society*, 124(36):10654–10655, 2002.

[32] Jeremy M Beebe, Vincent B Engelkes, Larry L Miller, and C Daniel Frisbie. Contact resistance in metal- molecule- metal junctions based on aliphatic sams: effects of surface linker and metal work function. *Journal of the American Chemical Society*, 124(38):11268–11269, 2002.

[33] David J Wold and C Daniel Frisbie. Formation of metal- molecule-metal tunnel junctions: Microcontacts to alkanethiol monolayers with a conducting afm tip. *Journal of the American Chemical Society*, 122(12):2970–2971, 2000.

[34] David J Wold, Rainer Haag, Maria Anita Rampi, and C Daniel Frisbie. Distance dependence of electron tunneling through self-assembled monolayers measured by conducting probe atomic force microscopy: Unsaturated versus saturated molecular junctions. *The Journal of Physical Chemistry B*, 106(11):2813–2816, 2002.

[35] Lambertus Groenendaal, Friedrich Jonas, Dieter Freitag, Harald Pielartzik, and John R Reynolds. Poly (3, 4-ethylenedioxythiophene) and its derivatives: past, present, and future. *Advanced materials*, 12(7):481–494, 2000.

[36] Hylke B Akkerman, Paul WM Blom, Dago M De Leeuw, and Bert De Boer. Towards molecular electronics with large-area molecular junctions. *Nature*, 441(7089):69–72, 2006.

[37] BC Haynie, AV Walker, TB Tighe, DL Allara, and N Winograd. Adventures in molecular electronics: how to attach wires to molecules. *Applied surface science*, 203:433–436, 2003.

[38] Bert De Boer, Martin M Frank, Yves J Chabal, Weirong Jiang, Eric Garfunkel, and Zhenan Bao. Metallic contact formation for molecular electronics: interactions between vapor-deposited metals and self-assembled monolayers of conjugated mono-and dithiols. *Langmuir*, 20(5):1539–1542, 2004.

[39] T Ohgi, H-Y Sheng, Z-C Dong, and H Nejoh. Observation of au deposited self-assembled monolayers of octanethiol by scanning tunneling microscopy. *Surface science*, 442(2):277–282, 1999.

[40] DR Jung, AW Czanderna, and GC Herdt. Interactions and penetration at metal/self-assembled organic monolayer interfaces. *Journal of Vacuum Science & Technology A: Vacuum, Surfaces, and Films*, 14(3):1779–1787, 1996.

[41] Hossam Haick, Marianna Ambrico, Jamal Ghabboun, Teresa Ligonzo, and David Cahen. Contacting organic molecules by metal evaporation. *Physical Chemistry Chemical Physics*, 6(19):4538–4541, 2004.

[42] Hossam Haick, Olivia Niitsoo, Jamal Ghabboun, and David Cahen. Electrical contacts to organic molecular films by metal evaporation: effect of contacting details. *The Journal of Physical Chemistry C*, 111(5):2318–2329, 2007.

[43] C Zhou, MR Deshpande, MA Reed, L Jones, and JM Tour. Nanoscale metal/self-assembled monolayer/metal heterostructures. *Applied Physics Letters*, 71(5):611–613, 1997.

[44] J Chen, W Wang, MA Reed, AM Rawlett, DW Price, and JM Tour. Room-temperature negative differential resistance in nanoscale molecular junctions. *Applied physics letters*, 77(8):1224–1226, 2000.

[45] K Bouzehouane, S Fusil, M Bibes, J Carrey, T Blon, M Le Du, P Seneor, V Cros, and Laurent Vila. Nanolithography based on real-time electrically controlled indentation with an atomic force microscope for nanocontact elaboration. *Nano Letters*, 3(11):1599–1602, 2003.

[46] Sergio Tatay, Marta Galbiati, Sophie Delprat, Clément Barraud, Karim Bouzehouane, Sophie Collin, Cyrile Deranlot, Eric Jacquet, Pierre Seneor, Richard Mattana, et al. Self-assembled monolayers based spintronics: from ferromagnetic surface functionalization to spin-dependent transport. *Journal of Physics: Condensed Matter*, 28(9):094010, 2016.

[47] Etienne Urbain. *Utilisation de semi-conducteurs organiques comme barrière tunnel pour l'électronique de spin*. Theses, Université de Strasbourg, December 2017.

[48] H. Hertz. Ueber einen einfluss des ultravioletten lichtes auf die electrische entladung. *Annalen der Physik und Chemie*, 267(8):983–1000, 1887.

[49] H. P. Bonzel and C. Kleint. On the history of photoemission. *Progress in Surface Science*, 49(2):107–153, 1995.

[50] Albert Einstein. Über die von der molekularkinetischen theorie der wärme geforderte bewegung von in ruhenden flüssigkeiten suspendierten teilchen. *Annalen der Physik*, 4, t. 17:549–560, 1905.

[51] Stephan Hufner. Photoelectron spectroscopy. *Springer*, 1995.

[52] B. Q. Lv, T. Qian, and H. Ding. Angle-resolved photoemission spectroscopy and its application to topological materials. *Nature Reviews Physics*, 1(10):609–626, 2019.

[53] Alexandra Junay. *Étude des propriétés électroniques et de transport multi-échelle de jonctions tunnel Au/Alcanethiols/n-GaAs (001)*. PhD thesis, Université Rennes 1, 2015.

[54] Alexandra Junay, Sophie Guézo, Pascal Turban, Sylvain Tricot, Arnaud Le Pottier, J Avila, Soraya Ababou-Girard, Philippe Schieffer, and F Solal. Effective metal top contact on the organic layer via buffer-layer-assisted growth: A multiscale characterization of au/hexadecanethiol/n-gaas (100) junctions. *The Journal of Physical Chemistry C*, 120(42):24056–24062, 2016.

[55] A. Junay, S. Guezo, P. Turban, G. Delhaye, B. Lepine, S. Tricot, S. Ababou-Girard, and F. Solal. Spatially resolved band alignments at au-hexadecanethiol monolayer-gaas(001) interfaces by ballistic electron emission microscopy. *Journal of Applied Physics*, 118(8), 2015.

[56] W. J. Kaiser and L. D. Bell. Direct investigation of subsurface interface electronic structure by ballistic-electron-emission microscopy. *Phys Rev Lett*, 60(14):1406–1409, 1988.

[57] Mario Prietsch. Ballistic-electron emission microscopy (beem): Studies of metal/semiconductor interfaces with nanometer resolution. *Physics Reports*, 253(4):163–233, 1995.

[58] R Ludeke, HJ Wen, and Andreas Schenk. Quantum interference in sio 2: A conduction-band mass reappraisal. *Applied Physics Letters*, 73(9):1221–1223, 1998.

[59] Rudolf Ludeke. Hot-electron effects and oxide degradation in mos structures studied with ballistic electron emission microscopy. *IBM Journal of Research and Development*, 44(4):517–534, 2000.

[60] Amin Bannani, Christian Bobisch, and Rolf Moller. Ballistic electron microscopy of individual molecules. *Science*, 315(5820):1824–1828, 2007.

[61] LD Bell and WJ Kaiser. Observation of interface band structure by ballistic-electron-emission microscopy. *Physical review letters*, 61(20):2368, 1988.

[62] M Prietsch and R Ludeke. Beem spectroscopy at interfaces of au, ag, cu, mg and ni films with n-gap (110). *Surface Science*, 251:413–417, 1991.

[63] R Ludeke, M Prietsch, and A Samsavar. Ballistic electron emission spectroscopy of metals on gap (110). *Journal of Vacuum Science & Technology B: Microelectronics and Nanometer Structures Processing, Measurement, and Phenomena*, 9(4):2342–2348, 1991.

[64] Igor Vurgaftman, J áR Meyer, and L Ramdas Ram-Mohan. Band parameters for iii–v compound semiconductors and their alloys. *Journal of applied physics*, 89(11):5815–5875, 2001.

[65] Sophie Guézo. *Microscopie à Emission d'Electrons Balistiques (BEEM): étude des propriétés électroniques locales d'hétérostructures.* PhD thesis, Université Rennes 1, 2009.

[66] Sophie Guézo, Pascal Turban, Sergio Di Matteo, Philippe Schieffer, S Le Gall, Bruno Lépine, C Lallaizon, and Guy Jézéquel. Transverse-momentum selection rules for ballistic electrons at epitaxial metal/gaas (001) interfaces. *Physical Review B*, 81(8):085319, 2010.

[67] Alexandra Junay, Sophie Guézo, Pascal Turban, Sylvain Tricot, Arnaud Le Pottier, J. Avila, Soraya Ababou-Girard, Philippe Schieffer, and F. Solal. Effective Metal Top Contact on the Organic Layer via Buffer-Layer-Assisted Growth: A Multiscale Characterization of Au/Hexadecanethiol/n-GaAs(100) Junctions. *Journal of Physical Chemistry C*, 120(42):24056–24062, 2016.

[68] A. Junay, S. Guezo, P. Turban, S. Tricot, A. Le Pottier, J. Avila, S. Ababou-Girard, P. Schieffer, and F. Solal. Effective metal top contact on the organic layer via buffer-layer-assisted growth: A multiscale characterization of au/hexadecanethiol/n-gaas(100) junctions. *Journal of Physical Chemistry C*, 120(42):24056–24062, 2016.

[69] Albert C Thompson, Douglas Vaughan, et al. *X-ray data booklet*, volume 8. Lawrence Berkeley National Laboratory, University of California Berkeley, CA, 2001.

[70] O Heckmann, H Magnan, P Le Fevre, D Chandesris, and JJ Rehr. Crystallographic structure of cobalt films on cu (001): elastic deformation to a tetragonal structure. *Surface science*, 312(1-2):62–72, 1994.

[71] JCA Huang, TE Wang, CC Yu, YM Hu, PB Lee, and MS Yang. Epitaxial growth and characterization of (100) and (110) permalloy films. *Journal of Crystal growth*, 171(3-4):442–446, 1997.

[72] Pierre Catrou, Sylvain Tricot, Gabriel Delhaye, Jean-Christophe Le Breton, Pascal Turban, B. Lépine, and Philippe Schieffer. Effect of oxygen vacancies at the Fe/SrTiO3(001) interface Schottky barrier and surface electron accumulation layer. *Physical Review B*, 98(11):115402, 2018.

[73] F Michelini, L Ressier, J Degauque, P Baules, AR Fert, JP Peyrade, and JF Bobo. Permalloy thin films on MgO (001): Epitaxial growth and physical properties. *Journal of applied physics*, 92(12):7337–7340, 2002.

[74] YQ Zhang, NY Sun, R Shan, JW Zhang, SM Zhou, Z Shi, and GY Guo. Anomalous hall effect in epitaxial permalloy thin films. *Journal of Applied Physics*, 114(16):163714, 2013.

[75] K. Thürmer, R. Koch, M. Weber, and K. H. Rieder. Dynamic evolution of pyramid structures during growth of epitaxial fe (001) films. *Phys. Rev. Lett.*, 75:1767–1770, Aug 1995.

[76] Agus Subagyo, Hirofumi Oka, Guido Eilers, Kazuhisa Sueoka, and Koichi Mukasa. Scanning tunneling microscopy observation of epitaxial bcc-fe(001) surface. *Japanese Journal of Applied Physics*, 39(6S):3777, jun 2000.

[77] John Giapintzakis, DM Ginsberg, MA Kirk, and S Ockers. Testing models of the symmetry of the superconducting pairing state by low-temperature electron irradiation of an untwinned single crystal of yba 2 cu 3 o 7- δ. *Physical Review B*, 50(21):15967, 1994.

[78] SP Pai, R Pinto, PR Apte, CP D'Souza, AG Chourey, and Dhananjay Kumar. Oxygen incorporation duringin situ growth of ybco films on both sides of substrates. *Bulletin of Materials Science*, 16(6):685–692, 1993.

[79] EM Kneedler, BT Jonker, PM Thibado, RJ Wagner, BV Shanabrook, and LJ Whitman. Influence of substrate surface reconstruction on the

growth and magnetic properties of fe on gaas (001). *Physical Review B*, 56(13):8163, 1997.

[80] E Kneedler, PM Thibado, BT Jonker, BR Bennett, BV Shanabrook, RJ Wagner, and LJ Whitman. Epitaxial growth, structure, and composition of fe films on gaas (001)-2× 4. *Journal of Vacuum Science & Technology B: Microelectronics and Nanometer Structures Processing, Measurement, and Phenomena*, 14(4):3193–3198, 1996.

[81] Bruno Lépine, S Ababou, A Guivarc'h, G Jézéquel, S Députier, R Guérin, A Filipe, A Schuhl, F Abel, C Cohen, et al. Solid state interdiffusions in epitaxial fe/gaas (001) heterostructures during ultrahigh vacuum annealings up to 450° c. *Journal of applied physics*, 83(6):3077–3080, 1998.

[82] J Alvarez, AL Vazquez De Parga, JJ Hinarejos, J De la Figuera, EG Michel, C Ocal, and R Miranda. Initial stages of the growth of fe on si (111) 7× 7. *Physical Review B*, 47(23):16048, 1993.

[83] J.S. Rudra and J.H. Collier. 2.205 - self-assembling biomaterials. In Paul Ducheyne, editor, *Comprehensive Biomaterials*, pages 77–94. Elsevier, Oxford, 2011.

[84] Paul G. Hoertz, Jeremy R. Niskala, Peng Dai, Hayden T. Black, and Wei You. Comprehensive investigation of self-assembled monolayer formation on ferromagnetic thin film surfaces. *Journal of the American Chemical Society*, 130(30):9763–9772, 2008.

[85] Sébastien Devillers, Alexandre Hennart, Joseph Delhalle, and Zineb Mekhalif. 1-dodecanethiol self-assembled monolayers on cobalt. *Langmuir*, 27(24):14849–14860, 2011.

[86] Zineb Mekhalif, Joseph Riga, J-J Pireaux, and Joseph Delhalle. Self-assembled monolayers of n-dodecanethiol on electrochemically modified polycrystalline nickel surfaces. *Langmuir*, 13(8):2285–2290, 1997.

[87] Zineb Mekhalif, Fabrice Laffineur, Nathalie Couturier, and Joseph Delhalle. Elaboration of self-assembled monolayers of n-alkanethiols on nickel polycrystalline substrates: Time, concentration, and solvent effects. *Langmuir*, 19(3):637–645, 2003.

[88] Sundar Rajalingam, Sébastien Devillers, Joseph Dehalle, and Zineb Mekhalif. A two step process to form organothiol self-assembled monolayers on nickel surfaces. *Thin Solid Films*, 522:247–253, 2012.

[89] M Volmer, M Stratmann, and H Viefhaus. Electrochemical and electron spectroscopic investigations of iron surfaces modified with thiols. *Surface and Interface Analysis*, 16(1-12):278–282, 1990.

[90] Marta Galbiati. *Molecular Spintronics : from Organic Semiconductors to Self-Assembled Monolayers*. Theses, Université Paris Sud - Paris XI, July 2014.

[91] L Motte and MP Pileni. Self-assemblies of silver sulfide nanocrystals: influence of length of thio-alkyl chains used as coating agent. *Applied surface science*, 164(1-4):60–67, 2000.

[92] NIST X ray Photoelectron Spectroscopy Database. National institute of standards and technology standard reference database number 20. *Gaithersburg MD, 20899*, 10.18434/T4T88K, 2000.

[93] D Wo Turner and MI Al Jobory. Determination of ionization potentials by photoelectron energy measurement. *The Journal of Chemical Physics*, 37(12):3007–3008, 1962.

[94] AW Potts, HJ Lempka, DG Streets, and WC Price. Photoelectron spectra of the halides of elements in groups iii, iv, v and vi. *Philosophical Transactions for the Royal Society of London. Series A, Mathematical and Physical Sciences*, pages 59–76, 1970.

[95] A-S Duwez, Geneviève Pfister-Guillouzo, Joseph Delhalle, and Joseph Riga. Probing organization and structural characteristics of alkanethiols adsorbed on gold and of model alkane compounds through their valence electronic structure: an ultraviolet photoelectron spectroscopy study. *The Journal of Physical Chemistry B*, 104(38):9029–9037, 2000.

[96] Masato M Maitani, David L Allara, Douglas AA Ohlberg, Zhiyong Li, R Stanley Williams, and Duncan R Stewart. High integrity metal/organic device interfaces via low temperature buffer layer assisted metal atom nucleation. *Applied Physics Letters*, 96(17):173109, 2010.

[97] GD Waddill, IM Vitomirov, CM Aldao, and JH Weaver. Cluster deposition on gaas (110): formation of abrupt, defect-free interfaces. *Physical review letters*, 62(13):1568, 1989.

[98] K Lüdge, BD Schultz, P Vogt, MMR Evans, W Braun, CJ Palmstrøm, W Richter, and N Esser. Structure and interface composition of co layers grown on as-rich gaas (001) c (4× 4) surfaces. *Journal of Vacuum Science & Technology B: Microelectronics and Nanometer Structures Processing, Measurement, and Phenomena*, 20(4):1591–1599, 2002.

[99] Marie Hervé, Sylvain Tricot, Yann Claveau, Gabriel Delhaye, Bruno Lépine, Sergio Di Matteo, Philippe Schieffer, and Pascal Turban. k-space spin filtering effect in the epitaxial Fe/Au/Fe/GaAs (001) spin-valve. *Applied Physics Letters*, 103(20):2408, 2013.

[100] R Allenspach, M Stampanoni, and A Bischof. Magnetic domains in thin epitaxial co/au (111) films. *Physical Review Letters*, 65(26):3344, 1990.

[101] Hossam Haick, Jonathan P Pelz, Teresa Ligonzo, Marianna Ambrico, David Cahen, Wei Cai, Camelia Marginean, Cristian Tivarus, and Raymond T Tung. Controlling au/n-gaas junctions by partial molecular monolayers. *physica status solidi (a)*, 203(14):3438–3451, 2006.

[102] Y Lu, JC Le Breton, Pascal Turban, Bruno Lépine, Philippe Schieffer, and G Jézéquel. Band structure of the epitaxial fe/ mgo/ gaas (001) tunnel junction studied by x-ray and ultraviolet photoelectron spectroscopies. *Applied physics letters*, 89(15), 2006.

[103] Fouad Sabry. *Multi Function Structure: Future Air Force systems will become integrated into multi-function material airframes with embedded sensor, and network components*, volume 17. One Billion Knowledgeable, 2022.

[104] Sophie Delprat. *Jonctions tunnel magnétiques avec des monocouches moléculaires auto-assemblées*. Theses, Université Pierre et Marie Curie - Paris VI, June 2017.

[105] A. Sommerfeld and H. Bethe. Handblich de physik von geiger und scheel. *Julius Springer-Verlag*, 24/2:450, 1993.

[106] Ragnar Holm. The electric tunnel effect across thin insulator films in contacts. *Journal of Applied Physics*, 22(5):569–574, 1951.

[107] John G Simmons. Generalized formula for the electric tunnel effect between similar electrodes separated by a thin insulating film. *Journal of applied physics*, 34(6):1793–1803, 1963.

[108] Wenyong Wang, Takhee Lee, and Mark A Reed. Elastic and inelastic electron tunneling in alkane self-assembled monolayers, 2004.

[109] R Erik Holmlin, Rainer Haag, Michael L Chabinyc, Rustem F Ismagilov, Adam E Cohen, Andreas Terfort, Maria Anita Rampi, and George M Whitesides. Electron transport through thin organic films in metal- insulator- metal junctions based on self-assembled monolayers [j. am. chem. soc. 2001, 123, 5075- 5085]. *Journal of the American Chemical Society*, 124(29):8762–8762, 2002.

[110] Wenyong Wang, Takhee Lee, and Mark A Reed. Mechanism of electron conduction in self-assembled alkanethiol monolayer devices. *Physical Review B*, 68(3):035416, 2003.

[111] Philip M Morse. The theory of electric and magnetic susceptibilities. by jh van vleck. oxford university press, 384 pages, 1932. *Science*, 76(1971):326–328, 1932.

[112] Helmut Kronmüller. General micromagnetic theory and applications. *Materials Science and Technology*, pages 1–43, 2006.

[113] M.J. Donahue and D.G. Porter. Oommf user's guide, version 1.0. *Interagency Report NISTIR 6376*, 10.18434/T4T88K, 1999.

[114] Lukas Exl, Dieter Suess, and Thomas Schrefl. Micromagnetism. *Handbook of Magnetism and Magnetic Materials*, pages 1–44, 2020.

[115] José Luis Costa-Krämer, José Luis Menéndez, Alfonso Cebollada, F Briones, D Garcıa, and A Hernando. Magnetization reversal asymmetry in fe/mgo (0 0 1) thin films. *Journal of magnetism and magnetic materials*, 210(1-3):341–348, 2000.

COLLEGE SCIENCES DE LA MATIERE
DOCTORAL DES MOLECULES
BRETAGNE ET MATERIAUX

Université de Rennes

Titre : Croissance et propriétés multi-échelles des jonctions tunnel magnétiques hybrides : vers le contrôle des Spinterfaces

Mot clés : Electronique moléculaire, Spintronique moléculaire, Propriétés électroniques, Transport d'électrons, Interfaces, Monocouches auto-assemblées

Résumé : Dans les jonctions tunnel magnétiques hybrides intégrant une barrière tunnel constituée d'une monocouche moléculaire auto-assemblée (SAM), le transport dépendant du spin est intimement lié aux propriétés électroniques aux interfaces ferromagnétiques (FM)/molécules de la jonction. D'un point de vue fondamental, la compréhension de ces effets dits de spinterfaces dans des systèmes modèles simples bien contrôlés est un prérequis au développement de dispositifs spintroniques moléculaires performants. Par ailleurs, d'un point de vue applicatif, la réalisation pratique de ces systèmes hybrides FM/SAMs/FM est encore un défi majeur, en raison de la difficulté intrinsèque à éviter la formation de courts-circuits dans les jonctions par diffusion de métal à travers le SAM lors du dépôt de l'électrode supérieure. Ce travail de thèse se focalise sur ces deux points. Nous avons dans un premier temps développé des jonctions tunnel magnétiques hybrides intégrant une barrière tunnel formée par un SAM d'alcanethiols greffé sous ultravide sur une électrode inférieure monocristalline de Fe(001). Nous avons mis en œuvre une méthode originale de croissance assistée par couche tampon de gaz rare condensé (BLAG) pour le dépôt d'une électrode supérieure ferromagnétique de Co sur le SAM, sans formation de courts-circuits. Les spectroscopies de photoélectrons X et UV ont été utilisées de manière intensive pour étudier chaque étape de fabrication de la jonction tunnel magnétique et en caractériser les propriétés électroniques aux interfaces. De manière complémentaire, nous avons étudié par microscopie et spectroscopie à émission d'électrons balistiques (BEEM) l'homogénéité latérale à l'échelle nanométrique du transport électronique ainsi que les alignements des niveaux d'énergie à l'interface supérieure Co/SAM. Pour un dépôt optimisé par BLAG, une interface homogène Co/SAM est obtenue sans formation de ponts métalliques à travers le SAM. Finalement, nous avons développé un jeu de masques transférables et compatibles avec le dépôt par BLAG permettant de microstructurer in situ des jonctions tunnel magnétiques modèles Co/SAM/Fe(001). Les propriétés de transport de telles jonctions de taille $5 \times 5 \mu m^2$ présentent des caractéristiques I(V) non-linéaires, signatures de l'effet tunnel électronique à travers une barrière organique exempte de courts-circuits sur une surface étendue.

Title: Growth and multi-scale properties of hybrid magnetic tunnel junctions : towards the control of Spinterfaces

Keywords: Molecular electronics, Molecular Spintronics, Electronic properties, electron transport, Interfaces, Self-assembled monolayers

Abstract: Magneto-transport properties in hybrid magnetic tunnel junctions integrating a self-assembled monolayer (SAM) as a tunnel barrier are intimately governed by the electronic properties at the ferromagnets (FM)/molecules interfaces or so-called spinterface effects. From a fundamental point of view, understanding the mechanisms of spinterface formation in simple well controlled model systems is a key prerequisite for engineering efficient molecular spintronic devices. On the other hand, practical fabrication of these FM/SAMs/FM systems is still a major challenge, due to the intrinsic difficulties to avoid the formation of electrical shorts trough the SAM tunnel barrier during top electrode deposition. The present doctoral thesis addresses these two points. We first developed model hybrid magnetic tunnel junctions integrating alkanethiol SAM tunnel barrier grafted under ultrahigh vacuum on single crystalline Fe(001) bottom electrode. We used an original buffer-layer assisted growth (BLAG) for the top Co ferromagnetic electrode deposition on the SAM without pinhole formation. X-ray and UV photoelectron spectroscopies were intensively used to investigate each step of the magnetic tunnel junction deposition and to study its interface electronic properties. Alternatively, we used ballistic electron emission microscopy (BEEM) and spectroscopy to investigate the electron transport lateral homogeneity and the energy level alignment at the Co/SAM top interface at the nanoscale. For optimal BLAG deposition, homogeneous Co/SAM interfaces are obtained without observed metal diffusion through the SAM. Finally, we developed a set of in situ transferable shadow masks compatible with BLAG deposition which were used to pattern Co/SAM/Fe(001) magnetic tunnel junctions. Transport properties of $5 \times 5\mu m^2$ tunnel junctions reveal non-linear I(V) curves, fingerprints of electron tunnelling through a pinhole-free SAM barrier over extended areas.